MULTIVARIABLE HIGH-AUTHORITY CONTROL OF PLATE-LIKE ACTIVE LIFTING SURFACES

by

Kenneth Brett Lazarus
B.S.E. Duke University (1986)
S.M. Massachusetts Institute of Technology (1989)

Submitted to the Department of Aeronautics and Astronautics
in Partial Fulfillment of the Requirements for the Degree of

Doctor of Philosophy

at the

Massachusetts Institute of Technology
June 1992

Signature of Author _____
Department of Aeronautics and Astronautics
May 15, 1992

Certified by _____
Professor Edward F. Crawley
Thesis Committee Chairman, Department of Aeronautics and Astronautics

Certified by _____
Professor Andreas von Flotow, Department of Aeronautics and Astronautics

Certified by _____
Professor John Dugundji, Department of Aeronautics and Astronautics

Certified by _____
Professor Steven R. Hall, Department of Aeronautics and Astronautics

Accepted by _____
Professor Harold Y. Wachman
Chairman, Department of Aeronautics and Astronautics

MULTIVARIABLE HIGH-AUTHORITY CONTROL OF PLATE-LIKE ACTIVE LIFTING SURFACES

by

Kenneth Brett Lazarus

Submitted to the Department of Aeronautics and Astronautics
on May 15, 1992 in Partial Fulfillment of the Requirements for
the Degree of Doctor of Philosophy

Abstract

This work investigates the use of distributed strain actuators for active aeroelastic control of plate-like flexible lifting surfaces. Simple models are used to reveal the fundamental mechanisms and parameters governing active aeroelastic control of lifting surfaces. A typical section analysis is employed to provide an understanding of the fundamental mechanisms and limitations involved in performing aeroelastic control. The effects of both articulated aerodynamic control surfaces and induced strain actuators are included in the model. The ability of these actuators to effect aeroelastic control is studied for each actuator individually as well as in various combinations. A deformable section analysis is used to determine the optimal size and placement of strain actuators incorporated into load bearing structural elements for the purpose of effecting control, and to establish guidelines for designing active lifting surfaces. Simplified models are also used to develop the scaling laws for strain actuated lifting surfaces. In addition to identifying fundamental parameters, detailed modeling techniques are developed for the dynamic aeroelastic analysis and control law design of actual plate-like lifting surfaces with integrated strain actuators. A dynamic modeling capability for active lifting surfaces is developed using the Rayleigh-Ritz assumed mode method and kernel function unsteady aerodynamics approximated by rational functions. The analytic model is utilized to design multiple-input, multiple-output controllers for active lifting surface test articles. High-authority, large-bandwidth compensators are designed using LQG optimal control theory. The control schemes are assessed analytically to determine their closed loop effectiveness and verified experimentally by bench-top disturbance rejection experiments and wind tunnel gust alleviation, command following and flutter suppression tests. In addition, a stability robustness test is developed to estimate, *a priori*, the control authority which can be applied to the test articles without destabilizing high frequency modes. The experiments demonstrate that distributed strain actuation can be effectively employed for aeroelastic control, with considerable disturbance attenuation achieved in both the quasi-steady response and over large bandwidths spanning many flexible modes. The results show the ability of strain actuators to effectively control flexible plate-like lifting surfaces.

Thesis Committee: Professor Edward F. Crawley, Chairman
Professor Andreas von Flotow
Professor John Dugundji
Professor Steven R. Hall

Acknowledgments

The author would like to express his sincere appreciation for all the guidance, support and encouragement provided by Professor Edward Crawley over the past few years. The author would also like to acknowledge the assistance of the other members of his doctoral committee. Many thanks are extended to Professor John Dugundji for his knowledge of aeroelasticity, Professor Steve Hall for his assistance with control issues and Professor Andy von Flotow for his insightful comments on a variety of subjects. In addition, I would like to thank everyone in SERC for providing the assistance, support, criticism and countless discussions needed to complete this work.

There are many others to thank besides my colleges at MIT. I would like to thank my parents and family for their support through good times and bad, and their constant encouragement to achieve. I also would like to acknowledge the support of my undergraduate advisor Professor David Loendorf who provided many opportunities and considerable motivation early in my engineering career. Finally, I would like to thank my friends for all the support, companionship and joy they have provided. To my special friends in Boston (Sarah, Jeff, Margaret, Julie, and Sean) thank you so much for everything, including my sanity. And, thanks to all the "buddies" for being better friends than anyone could ever hope to have.

This thesis is dedicated to my father and Zaddie whose love, kindness, drive and spirit have been both a guiding light and an inspirational force.

The work presented in this thesis was sponsored by the General Dynamics Corporation and the NASA Langley Research Center. Their support has been greatly appreciated.

Table of Contents

List of Figures

List of Tables

Chapter 1. Introduction

Current and future performance criteria for space vehicles, submarines and aircraft demand lightweight flexible structures such as solar arrays, antennas, mirrors, skins and lifting surfaces. Structural integrity and mission requirements of these plate-like and shell-like components of aerospace and hydrodynamic vehicles also call for low vibration and load levels, as well as precision pointing, alignment and shape control. One way of achieving these conflicting specifications of light-weight and high dynamic performance for plate- and shell-like structures is through the use of integrated strain actuators and high-authority, large-bandwidth active control systems. High-authority, large-bandwidth active control can be achieved by designing multiple-input, multiple-output (MIMO) control laws for active composite structures with distributed strain actuators. Active structures are those structures controlled by actuators which are integrated into the load bearing elements and have structural functionality [Wada, Fanson and Crawley, 1989]. Active structures with integrated strain actuators provide a natural and logical mechanism for effecting distributed multiple actuator control and for implementing modern model-based control methodologies such as the Linear Quadratic Gaussian (LQG) [Kwakernaak and Sivan, 1972], $\mathcal{H}_\infty$ [Doyle, *et. al.*, 1989] and Optimal Projection [Hyland and Bernstein, 1984] techniques.

This thesis concentrates on one particular application of actively controlled plate-like flexible structures: that of dynamic aeroelastic lifting surface control through the use of strain actuation. Active lifting surface control is desirable for enhancing aircraft performance, decreasing loads and improving ride quality. Traditionally, aeroelastic control of flexible lifting surfaces has been effected through the use of articulated aerodynamic control surfaces such as ailerons or flaperons. A great deal of research has been performed over the past few decades concerning the development and implementation of various feedback control schemes which utilize such articulated actuator systems. Researchers have examined the fundamentals of traditional aeroservoelasticity using typical section models, simplified aerodynamics and classical control methods [Horikawa and Dowell, 1979, Ohta, *et. al.*, 1989 and Heeg, 1991]. More representative models and modern

control techniques have been applied to examine problems such as flutter suppression [Newsom, 1979, Mahesh, *et. al.*, 1981, Newsom, Pototzky and Abel, 1985 and Liebst, Garrard and Adams, 1986] and gust alleviation [Karpel, 1982]. And recently, the active flexible wing (AFW) has been used to demonstrate the ability of conventional control surfaces and modern control techniques to suppress flutter while performing various maneuvers in wind tunnel experiments [Waszak and Srinathkumar, 1991, Christhilf and Adams, 1992 and Mukhopadhyay, 1992]. In addition, topics such as model order reduction [Mukhopadhyay, Newsom and Abel, 1982 and Tiffany and Karpel, 1989] multiple control surface actuation [Noll, Perry and Tiffany, 1989 and Perry, Mukhopadhyay and Hoadley, 1990] and aeroservoelastic tailoring integration [Gilbert, Schmidt and Weisshaar, 1984 and Zeiler and Weisshaar, 1988] have been studied.

In contrast to the above work which employs the usual articulated control surface actuators, this research concentrates on an alternative and fundamentally different method of dynamic aeroelastic control. The technique involves the use of induced strain actuators, which are regulated to apply equivalent forces and moments on the lifting surface, in order to deform the wing and effect dynamic aeroelastic control. Induced strain actuators, such as piezoceramics and electrostrictives, directly deform the structure through electromechanical coupling terms which appear in the actuator constitutive relations. Active lifting surfaces with distributed strain actuators have advantages over conventional articulated control surface wings which are subject to loss of effectiveness at high dynamic pressures and limited servo motor bandwidths [Lazarus, Crawley and Bohlmann, 1991]. Strain actuation is advantageous because it can directly control both the shape of and strain in the lifting surface. Thus, two mechanisms by which aeroelastic control can be effected are available. Both the control of aerodynamic forces created by altering the airfoil shape and direct control of the strain in the lifting surface may be used to improve aircraft performance. Specifically, a strain actuated active lifting surface can be used for gust and load alleviation (*i.e.*, disturbance rejection), flutter and vibration suppression (*i.e.*, plant regulation), and maneuver enhancement (*i.e.*, command following).

Active control research certainly has not been limited to the application of dynamic lifting surface control. In fact, active control has been considered for many aerospace applications, as illustrated by recent research activity. The control of truss and truss-like structures using modern methods such as LQG [Gehling, 1991], $\mathcal{H}_\infty$ [Voth and Stoughton, 1991, Fanson, *et. al.*, 1991 and Carrier *et. al.*, 1991], Fixed Architecture Optimal Projection [Peterson, 1991] and Maximum Entropy / Optimal Projection (MEOP) [Philips, Hyland and Collins, 1990] have been investigated for various spacecraft applications. The application of modern control techniques to active plate- and shell-like structures has also been examined, but not as extensively. Studies have been limited to shape control of precision reflectors [Chiarappa and Claysmith, 1981], static aeroelastic applications with simple feedback schemes [Lazarus, Crawley and Bohlmann, 1991, Weisshaar and Ehlers, 1991 and Waszak and Srinathkumar, 1991], the reduction of radiated structure-borne noise using adaptive feed-forward techniques [Zhou and Cudney, 1991 and Akishita, *et. al.*, 1991] and the control of non-active inertially actuated plates by independent modal space LQG control [Rubenstien. *et. al.*, 1991].

Current research in active controls for solving a variety of aerospace problems coupled with the potential for meeting stringent aircraft performance requirements has motivated a thorough investigation of the strain actuated active lifting surface. Consequently, this thesis investigates, develops and demonstrates the basic technology necessary for active aeroelastic control using integrated strain actuators. Assessing the use of strain actuation for dynamic aeroelastic control requires extensive application of interdisciplinary analysis methods. Thus, this work draws on research from many fields including advanced material systems, structural dynamics, aerodynamic modeling and modern control theory. Further, a combination of simple models and detailed analysis techniques, as well as open and closed loop tests are required to accurately assess the ability of active lifting surfaces to effect aeroelastic control. The elaborate analytical and experimental program followed in this study is outlined below.

The first step necessary for developing an understanding of strain actuated aeroelastic control is to examine simple models to find the

fundamental parameters and physical mechanism involved in controlling lifting surfaces with strain actuation. In Chapter 2, a typical section analysis is used to reveal the parameters fundamental to effecting aeroelastic control using either conventional articulated surfaces or strain actuators, and to find the relative merits of each method of control. In Chapter 3, a deformable section analysis is used to show the optimal relations relevant to incorporate strain actuators into load bearing structures for the purpose of effecting control, and to establish guidelines for designing active lifting surfaces. Also in this chapter, the scaling laws for strain actuated lifting surfaces are developed. The scaling laws are needed to apply the results of scale model tests to that of actual lifting surfaces and to understand the concerns which need be addressed in order to construct effective and realistic full sized active lifting surfaces.

The work in Chapters 2 and 3 reveals the viability of using strain actuation for aeroelastic control. The next step is therefore to demonstrate that an active lifting surface can actually exert aeroelastic control. Chapter 4 describes the scale model active lifting surfaces, and associated hardware, used in the bench-top and wind tunnel demonstration experiments. For the purpose of designing effective compensators, the dynamic characteristics of strain actuated composite lifting surface test articles are first modeled analytically and then verified experimentally. The dynamic, aerodynamic, and finally aeroelastic modeling is described in Chapter 5. Next, the analytic model is used to derive high-authority, large-bandwidth MIMO compensators based on a quadratic cost function and LQG optimal control theory. Compensators are also designed using frequency domain Loop Transfer Recovery (LTR) techniques. The compensator design procedure is discussed in Chapter 6. The control schemes are then assessed analytically to determine their effectiveness based on the closed loop quadratic cost index and verified experimentally by bench-top closed loop testing and wind tunnel gust alleviation, command following and flutter suppression tests.

The bench-top experiments, found in Chapter 7, served to verify portions of the analytical model, check the hardware functionality and acquire control law design experience before closed loop wind tunnel testing. The bench-top experiments also demonstrate the ability of strain actuation to

effect high-authority control over large bandwidths spanning many flexible modes. The wind tunnel experiment, described in Chapter 8, show the ability of the strain actuated lifting surfaces to achieve aeroelastic control objectives such as gust disturbance attenuation, input command following and flutter suppression. Gust alleviation is needed to eliminate unwanted vibrations which cause performance degradation, poor ride quality and dynamically amplified loads. Command following in bandwidths from quasi-steady up to and through the fundamental vibration frequency is desirable for enhancing aircraft performance specifications such as pull-up and roll rates. And, flutter suppression is important for increasing the flight envelope of high performance aircraft.

The bench-top and wind tunnel experimental results are reported in the form of closed loop state versus control cost curves in order to demonstrate the significant disturbance attenuation obtainable by applying modern control techniques to active plate-like structures. Reporting the closed loop results in this manner not only shows the performance achieved, but also displays the control authority used in relation to the maximum possible, and aids in determining the cause of performance limitations. In addition, practical tools needed for estimating, *a priori*, closed loop performance limits from open loop experiments and analytic models (*i.e.*, stability robustness) are developed and correlated with the actual limits found during closed loop testing. The results of the closed loop performance and stability robustness tests are discussed in the conclusions, as are the implications of these results and those of the typical and deformable sections for controlling actual lifting surfaces with integrated strain actuators.

Chapter 2. Typical Section Analysis

The objective of this analysis is to explore the fundamental mechanisms governing the control of dynamic aeroelastic systems, and to develop a method for consistently comparing various control schemes in order to assess the advantages and limitations of each. For this purpose a two degree-of-freedom typical section is employed. Such an analysis offers fundamental insights into the aeroelastic control problem which are often obscured by the numerical calculations required for the analysis of large order systems or the design of multivariable control laws. Included in the typical section model are forces and moments produced by both induced strain actuators and conventional articulated control surfaces. The actuator or combination of actuators selected has a direct bearing on the effectiveness of the control system. Equally important is the choice of sensors and output variables measured and fed back to the controller. In order to choose the best combination of actuators and sensors for a particular lifting surface, it is essential to understand the fundamental mechanisms involved in aeroelastic control and the advantages and inherent limitations of different controllers.

In this chapter, the governing equations for the typical section with induced strain and conventional actuators are derived. The plant dynamics are examined, as are the feedback schemes associated with the various possible state outputs (plunge and pitch) and various possible control inputs (bending due to strain actuation, torsion due to strain actuation, and the aerodynamic forces resulting from leading and trailing edge flap rotation) for several types of control laws. Control schemes are developed for single-input, single-output (SISO) and full state feedback multiple-input, multiple-output (MIMO) systems using both classical and modern state space techniques. These control laws are compared and a closed loop state versus control cost analysis is performed for various input combinations using solutions to the Linear Quadratic Regulator (LQR) problem. The analysis reveals the fundamental benefits and limitations of employing various control schemes for aeroelastic control. The results obtained can be applied to a wide variety of aeroservoelastic problems, such as flutter, vibration suppression, gust alleviation and low frequency servo shape control for maneuverability. Note that this work closely follows that of Lazarus, Crawley and Lin [1991].

2.1 Typical Section Governing Equations

For many years, low order models called typical sections have been used to explain the fundamental mechanics of aeroelasticity [Bisplinghoff, Ashley and Halfman, 1955]. These sections capture the essential physical features and have properties representative of actual lifting surfaces. The geometry of the typical section employed in this analysis is shown in Fig. 2.1. The section is given plunge $\bar{h}$ and pitch α degrees of freedom, and a leading and trailing edge flap. The structural restraints in bending and torsion appear at the elastic axis, and the disturbance to the section is a time variation in the inflow angle α_o.

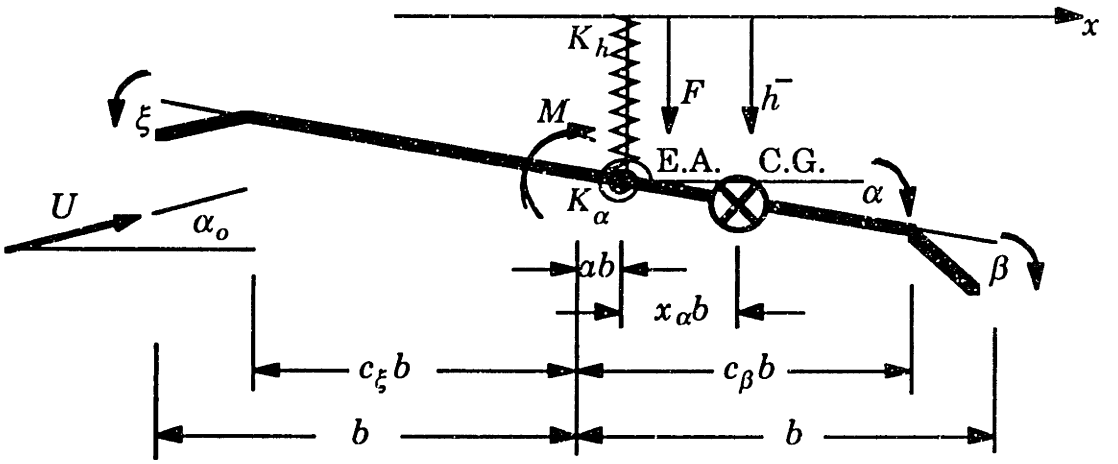

Figure 2.1. Typical section geometry with leading and trailing edge flaps. The forces and moments applied at the elastic axis due to control surface and strain actuation are indicated in the figure.

The aerodynamics are found by adapting the incompressible wing-aileron-tab lifting surface results obtained by Theodorsen and Garrick [Theodorsen and Garrick, 1942] to a leading edge flap-wing-trailing edge flap lifting surface via a coordinate transformation. Only the steady state aerodynamic terms are retained to simplify the initial examination of the problem. In practice, this would limit direct applicability of the results to low reduced frequencies. The aerodynamic forces and moments created by deflecting the leading edge ξ or trailing edge β flap are modeled as forces and moments acting at the elastic axis, so that the high frequency dynamics associated with the flaps can be neglected. The typical section also includes forces and moments acting at the elastic axis which result from commands to

the strain actuators. These are the equivalent forces and moments acting on the typical section which develop as a result of induced strain actuation. The equivalent forces and moments can be found (see Appendix 2.A) by applying Bernoulli-Euler beam and Kirchhoff plate theory as done in Crawley and de Luis [1987] or Crawley and Lazarus [1991].

Writing the equations in terms of non-dimensional mass **M**, stiffness **K**, forcing **f** and disturbance **d** matrices yields

$$\mathbf{M}\begin{Bmatrix}\bar{h}p^2\\ \alpha p^2\end{Bmatrix}+\mathbf{K}\begin{Bmatrix}\bar{h}\\ \alpha\end{Bmatrix}=\mathbf{f}\begin{Bmatrix}u_h\\ u_\alpha\\ u_\beta\\ u_\xi\end{Bmatrix}+\mathbf{d}\alpha_o(p) \qquad \text{or}$$

$$\begin{bmatrix}\frac{1}{R_\alpha^2} & \frac{x_\alpha}{R_\alpha^2}\\ \frac{x_\alpha}{R_\alpha^2} & 1\end{bmatrix}\begin{Bmatrix}\bar{h}p^2\\ \alpha p^2\end{Bmatrix}+\begin{bmatrix}\frac{\bar{\omega}_h^2}{R_\alpha^2} & \bar{q}C_{L_\alpha}\\ 0 & 1-\bar{q}C_{M_\alpha}\end{bmatrix}\begin{Bmatrix}\bar{h}\\ \alpha\end{Bmatrix}=\begin{bmatrix}1 & 0 & -\bar{q}C_{L_\beta} & -\bar{q}C_{L_\xi}\\ 0 & 1 & \bar{q}C_{M_\beta} & \bar{q}C_{M_\xi}\end{bmatrix}\begin{Bmatrix}u_h\\ u_\alpha\\ u_\beta\\ u_\xi\end{Bmatrix}+\begin{bmatrix}-\bar{q}C_{L_\alpha}\\ \bar{q}C_{M_\alpha}\end{bmatrix}\alpha_o \tag{2.1.1}$$

where

$\bar{q} = \dfrac{U_\alpha^2}{\pi\mu R_\alpha^2}$ Normalized Dynamic Pressure

$p = \dfrac{\lambda}{\omega_\alpha}$ Normalized Laplace Variable

$u_h = \dfrac{Fb}{K_\alpha}$ Normalized Strain Actuated Plunge Force

$u_\alpha = \dfrac{M}{K_\alpha}$ Normalized Strain Actuated Pitch Torque

$u_\beta = \beta$ Trailing Edge Flap Deflection

$u_\xi = \xi$ Leading Edge Flap Deflection

and the remaining non-dimensional variables are those usually employed in a typical section analysis such as lift C_L and moment C_M coefficient, frequency $\bar{\omega}_h$ and mass μ ratio, radius of gyration R_α, and static imbalance x_α [Bisplinghoff, Ashley and Halfman, 1955]. Note that the equivalent force u_h and moment u_α produced by the induced strain actuators are normalized by the section torsional stiffness K_α.

The characteristic equation for this two degree-of-freedom system is found by setting the right hand side of Eq. 2.1.1 equal to zero

$$\Delta(p)=\left[1-\frac{x_\alpha^2}{R_\alpha^2}\right]p^4+\left[\left(\bar{\omega}_h^2+1\right)-\bar{q}\left(C_{L_\alpha}x_\alpha+C_{M_\alpha}\right)\right]p^2+\left[\bar{\omega}_h^2\left(1-\bar{q}C_{M_\alpha}\right)\right] \tag{2.1.2}$$

Eq. 2.1.2 shows that the roots of the system (*i.e.*, transfer function poles) are dependent on the section geometry, structural properties, and air speed, but are independent of the actuation method. Note that there is no structural or air damping modeled in the system.

The transfer functions from the four control inputs (bending strain actuation u_h, torsion strain actuation u_α, trailing edge flap defection u_β, and leading edge flap deflection u_ξ) to the two output variables (plunge $\bar{h}$ and pitch α) are given by

$$\begin{Bmatrix}\bar{h}\\ \alpha\end{Bmatrix}=\frac{R_\alpha^2}{\Delta(p)}\begin{bmatrix}\mathrm{n}_{hh}(p) & \mathrm{n}_{h\alpha}(p) & \mathrm{n}_{h\beta}(p) & \mathrm{n}_{h\xi}(p)\\ \mathrm{n}_{\alpha h}(p) & \mathrm{n}_{\alpha\alpha}(p) & \mathrm{n}_{\alpha\beta}(p) & \mathrm{n}_{\alpha\xi}(p)\end{bmatrix}\begin{Bmatrix}u_h\\ u_\alpha\\ u_\beta\\ u_\xi\end{Bmatrix}$$

$$\mathrm{n}_{hh}(p)=p^2+1-\bar{q}C_{M_\alpha}$$

$$\mathrm{n}_{\alpha h}(p)=-\frac{x_\alpha p^2}{R_\alpha^2}$$

$$\mathrm{n}_{h\alpha}(p)=-\frac{x_\alpha p^2}{R_\alpha^2}-\bar{q}C_{L_\alpha}$$

$$\mathrm{n}_{\alpha\alpha}(p)=\frac{p^2}{R_\alpha^2}+\frac{\bar{\omega}_h^2}{R_\alpha^2}$$

$$\mathrm{n}_{h\beta}(p)=\bar{q}C_{L_\beta}\left(\bar{q}C_{M_\alpha}\left(1-\frac{C_{L_\alpha}C_{M_\beta}}{C_{M_\alpha}C_{L_\beta}}\right)-1-p^2\left(1+\frac{C_{M_\beta}x_\alpha}{C_{L_\beta}R_\alpha^2}\right)\right)$$

$$\mathrm{n}_{\alpha\beta}(p)=\frac{1}{R_\alpha^2}\bar{q}C_{M_\beta}\left(p^2\left(1+\frac{C_{L_\beta}x_\alpha}{C_{M_\beta}}\right)+\bar{\omega}_h^2\right)$$

$$\mathrm{n}_{h\xi}(p)=\bar{q}C_{L_\xi}\left(\bar{q}C_{M_\alpha}\left(1-\frac{C_{L_\alpha}C_{M_\xi}}{C_{M_\alpha}C_{L_\xi}}\right)-1-p^2\left(1+\frac{C_{M_\xi}x_\alpha}{C_{L_\xi}R_\alpha^2}\right)\right)$$

$$\mathrm{n}_{\alpha\xi}(p)=\frac{1}{R_\alpha^2}\bar{q}C_{M_\xi}\left(p^2\left(1+\frac{C_{L_\xi}x_\alpha}{C_{M_\xi}}\right)+\bar{\omega}_h^2\right) \tag{2.1.3}$$

where each element $n_{ij}(p)$ of this two by four matrix relation represents the transfer function from one of the inputs to one of the outputs. The zeros of each individual SISO transfer functions are found by setting each numerator $n_{ij}(p)$ to zero. The zero locations are dependent on the section geometry and structural properties, as were the system poles. For the case of plunge $\bar{h}$ measurement, the individual SISO transfer function zeros move rapidly with air speed. For the case of pitch α measurement, the zeros are not dependent on air speed U_α.

Alternatively, the governing equations (Eq. 2.1.1) can be written in a state space representation

$$\begin{aligned} \dot{\mathbf{x}} &= \mathbf{A}\mathbf{x} + \mathbf{B}\mathbf{u} + \mathbf{L}\alpha_o(p) \\ \mathbf{y} &= \mathbf{C}\mathbf{x} \end{aligned} \tag{2.1.4}$$

where

$$\mathbf{A} = \begin{bmatrix} \mathbf{0}_{(2x2)} & \mathbf{I}_{(2x2)} \\ -\mathbf{M}^{-1}\mathbf{K} & \mathbf{0}_{(2x2)} \end{bmatrix} \quad \mathbf{B} = \begin{bmatrix} \mathbf{0}_{(2x4)} \\ \mathbf{M}^{-1}\mathbf{f} \end{bmatrix} = \begin{bmatrix} \mathbf{b}_h & \mathbf{b}_\alpha & \mathbf{b}_\beta & \mathbf{b}_\xi \end{bmatrix}$$

$$\mathbf{L} = \begin{bmatrix} \mathbf{0}_{(2x4)} \\ \mathbf{M}^{-1}\mathbf{d} \end{bmatrix} \quad \mathbf{x} = \begin{Bmatrix} \bar{h} \\ \alpha \\ \dot{\bar{h}} \\ \dot{\alpha} \end{Bmatrix} \quad \mathbf{u} = \begin{Bmatrix} u_h \\ u_\alpha \\ u_\beta \\ u_\xi \end{Bmatrix}$$

In this form, the input/output relation from the actuators to the measurements is

$$\mathbf{y} = \mathbf{C}\Phi\mathbf{B}\mathbf{u} \quad \text{where} \quad \Phi = (p\mathbf{I} - \mathbf{A})^{-1} \tag{2.1.5}$$

Note that the characteristic equation (Eq. 2.1.2) is found by taking the determinant of Φ^{-1}, and that Eqs. 2.1.3 and 2.1.5 are identical when the output matrix **C** is chosen such that the measurements **y** are $\bar{h}$ and α.

2.2 Typical Section Properties

As seen from Eqs. 2.1.2 and 2.1.3, the location of the system poles and transfer function zeros are highly dependent on the geometrical and structural properties of the typical section. Therefore it is necessary to choose some nominal parameters in order to proceed with the analysis and control system design. The section properties chosen were those at the three quarter span of the aluminum induced strain actuated test article described in

Chapter 4. The test article had a full span aspect ratio of 3.9 and a thickness to chord ratio of 0.51 percent. The resulting typical section is altered to include ten percent leading and trailing edge flaps; and the elastic axis is moved forward of the midchord by ten percent of the chord so that flutter occurs before static divergence. The resulting typical section has a frequency ratio $\overline{\omega}_h$ of one-fifth and a mass ratio μ of twenty, not atypical of built up wings. Other relevant section properties are listed in Table 2.1.

Parameter	Symbol	Value
Section Geometry	a	–0.2
	x_α	0.2
	R_α^2	0.25
	μ	20
	$\overline{\omega}_h$	0.2
Wing Parameters	$\frac{t}{2b}$	0.51%
	$\frac{L}{b}$	3.92
Steady Aerodynamic Coefficients	C_{L_α}	2π
	C_{M_α}	1.885
	C_{L_β}	2.487
	C_{M_β}	–0.334
	C_{L_ξ}	–0.087
	C_{M_ξ}	–0.146
State Cost Matrix	N_{hh}	$(1/0.406)^2$
	$N_{\alpha\alpha}$	$(1/0.282)^2$
Control Cost Matrix	R_{hh}	$(1/0.0429)^2$
	$R_{\alpha\alpha}$	$(1/0.0215)^2$
	$R_{\beta\beta}$	$(1/0.0873)^2$
	$R_{\xi\xi}$	$(1/0.0436)^2$

Table 2.1. Nominal geometrical and material properties of the typical section

Knowledge of the system pole and zero locations is important for determining the manner in which a system can be controlled and is essential in designing SISO feedback control laws. In aeroelastic systems, all of the pole and some of the zero locations are a function of air speed U_α, which indicates that a control law appropriate at one flight condition may not necessarily be appropriate at others. In particular, the rate of zero movement and the propensity for the pole/zero pattern along the imaginary axis to change (*i.e.*, pole/zero flipping) is a particular indicator of the potential non-robustness of the closed loop control scheme [Rosenthal, 1984 and Fleming and Crawley, 1991]. It is therefore interesting to observe the relative and absolute movement of the system poles and the SISO transfer function zeros as a function of air speed. Such a plot of the purely oscillatory poles and zeros associated with plunge measurement feedback is shown in Fig. 2.2. Notice the two poles coalesce at the flutter point (U_α=1.90).

For the case of plunge $\bar{h}$ measurement, all four of the individual SISO transfer function zeros change with air speed. The SISO transfer function zeros associated with the bending strain actuator u_h are at the torsional natural frequency ω_α when the air speed is zero. These zeros decrease quadratically to zero at the divergence speed (U_α=2.88). Likewise, the zeros associated with the trailing edge flap actuator u_β decrease quadratically with air speed to zero at the reversal speed (U_α=2.40). The air speed at which the frequency component of the individual SISO transfer function zeros goes to zero is especially significant to the aeroelastic control problem, since it is at this air speed that one of the zeros becomes non-minimum phase (*i.e.*, moves into the right half of the Laplace-plane). The presence of a non-minimum phase zero indicates a fundamental limitation on the amount of control which can be applied to the system [Freudenberg and Looze, 1985]. The zeros associated with the torsion strain actuator u_α and leading edge flap actuator u_ξ also move with air speed. The zeros in both of these SISO transfer functions increase with air speed as shown in Fig. 2.2. Note that all of the zero frequencies intersect with the torsion pole frequency at the same air speed. This indicates that a pole/zero cancellation has occurred due to a loss of observability of the torsional mode. At this air speed, the aeroelastic system is such that the torsional mode can not be observed by measuring the displacement of the plunge variable $\bar{h}$.

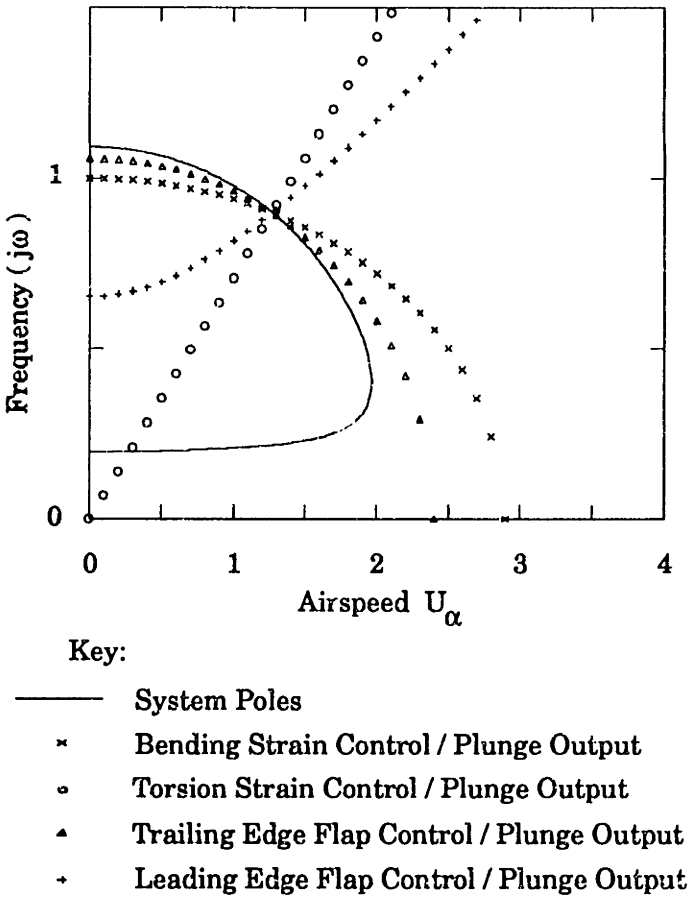

Figure 2.2. Pole and individual SISO transfer function zero frequencies versus air speed U_α. Coalescence of the system poles and the movement of the individual SISO transfer function zeros for plunge measurement output are plotted.

The individual SISO transfer function zeros associated with pitch α measurement, which are independent of the air speed, are not shown in Fig. 2.2. Examining Eq. 2.1.3, it can be seen that the two zeros associated with the bending strain actuator u_h are always at the origin, and that the two zeros associated with the torsion strain actuator u_α are always on the imaginary axis at $\bar{\omega}_h$. In both cases this places the zeros below the lower (plunge) pole of the system for all non-zero airspeeds. The zeros associated with the leading edge flap u_ξ and trailing edge flap u_β actuators depend on $\bar{\omega}_h$ and the aerodynamic influence coefficients, and may be imaginary or real. In the event they are real, once again one would be a non-minimum phase zero indicating a limitation on achievable control.

Due to the significant movement of the system poles and zeros as a function of air speed, it is necessary to choose specific dynamic pressures to analyze the system and design feedback control schemes. Two air speeds are chosen and are indicated on the pole locus plot in Fig. 2.3. The first speed is at about ten percent below the flutter velocity (U_α=1.90) and is designated as design point 1 (U_α=1.71) The second is chosen at about five percent above the flutter velocity and is designated as design point 2 (U_α=2.00). Both design points are below reversal and divergence. These speeds are chosen so that the control law designs are dominated by fundamental aeroelastic control issues, and are not complicated by factors such as aileron reversal or static instabilities.

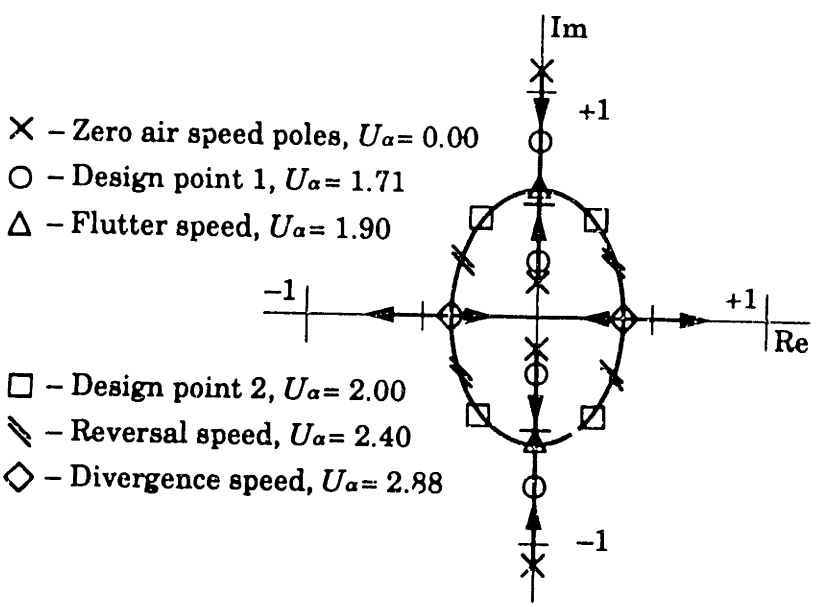

Figure 2.3. Location of the open loop poles as the non-dimensional air speed U_α increases from zero and goes through design point 1, flutter, design point 2, reversal and divergence.

2.3 Single-Input, Single-Output Control

The combination of four actuator control inputs and two measurement output variables allows for eight SISO feedback control options to be considered. The transfer functions for the eight options are defined by Eq. 2.1.3, and the location of the poles and zeros are illustrated graphically in Fig. 2.4 for the below flutter design point (U_α=1.71). At this air speed, all the poles lie on the imaginary axis indicating that each system is neutrally stable. Thus, the control objective is to add damping to the modes of the

system [Miller, Jacques and de Luis, 1990]. Note that in each system there is a zero "missing" from between the two poles (*i.e.*, between the two system poles there is no zero). This missing zero dictates that simple gain feedback, either displacement $u=-fz$ or rate $u=-pfz$, will not stabilize the system (*i.e.*, add damping) for any value (or sign) of the gain f.

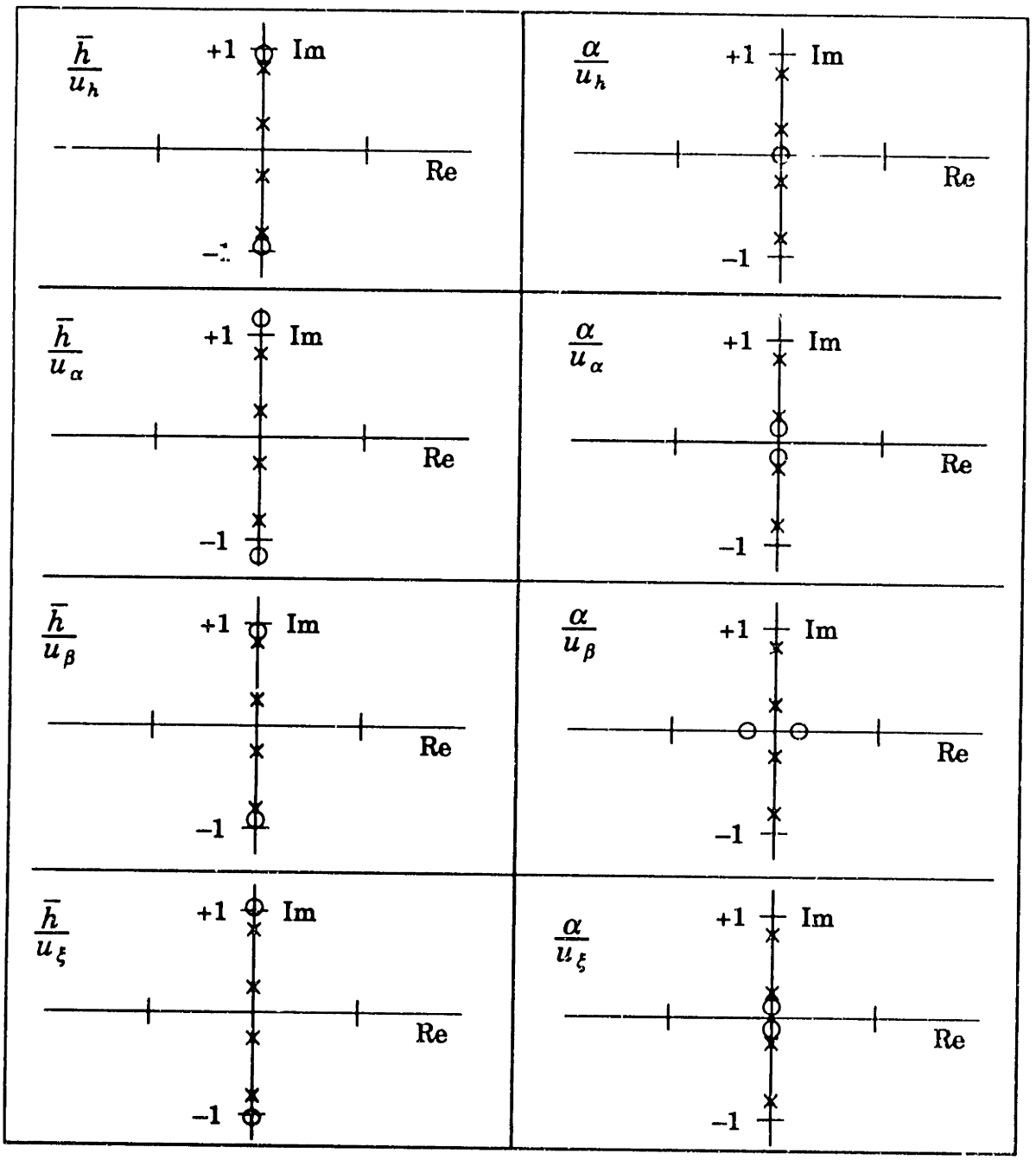

Figure 2.4. Pole and zero locations for the individual SISO input/output combinations at design point 1 (U_a=1.71).

For the cases of pitch feedback to bending strain actuation α/u_h, pitch feedback to torsion strain actuation α/u_α, and pitch feedback to leading edge flap actuation α/u_ξ the pitch mode can be stiffened (the frequency of this pole increases), but no damping is added to the closed loop system (*i.e.*, the poles do not move into the left half of the Laplace plane). In all other cases, the closed loop system is destabilized (*i.e.*, a system pole moves into the right half of the Laplace-plane) by displacement or rate feedback. Note also that the pitch measurement to the trailing edge flap actuator α/u_β transfer function, a common conventionally used SISO loop, has a non-minimum phase zero at this air speed.

Since simple feedback does not produce stable closed loop systems, other control schemes must be employed. The first option is to place a sensor at some desirable point on the section so that a stabilizing combination of the plunge and pitch output variables are fed back to the actuator. The sensor placement relation can be expressed as the vertical displacement

$$\begin{aligned} & y = \bar{h} + x_s \alpha \\ & \text{or} \quad \mathbf{c} = \begin{bmatrix} 1 & x_s & 0 & 0 \end{bmatrix} \quad \text{in state space form} \end{aligned} \tag{2.3.1}$$

If the sensor can be placed in a position x_s, which places a SISO transfer function zero between the open loop poles, the system can be stabilized using rate feedback of the output variable y. Fig. 2.5 illustrates the poles and zeros of the loop transfer function (y/u or $\mathbf{c\Phi b}$ in state space form) and the resulting SISO root locus for such a stable closed loop system. Eqs. 2.1.3 and 2.3.1 can be combined to give equations for the four SISO transfer functions between any of the four control inputs and the output measurement y. Setting the numerator of each transfer function to zero gives an expression for each SISO transfer function zero. The sensor position x_s can then be found, which yields the desired SISO transfer function zeros for each method of actuation. The sensor positions as a function of the desired zero locations for the four actuation schemes are

$$
\begin{aligned}
u_h \quad \text{Control:} \quad & x_s = \frac{R_\alpha^2}{x_\alpha}\left(1-\frac{\bar{q}C_{M_\alpha}-1}{p^2}\right) \\
u_\alpha \quad \text{Control:} \quad & x_s = \frac{x_\alpha p^2 + \bar{q}C_{L_\alpha}R_\alpha^2}{p^2+\bar{\omega}_h^2} \\
u_\beta \quad \text{Control:} \quad & x_s = \frac{p^2\left(\frac{C_{M_\beta}x_\alpha}{C_{L_\beta}R_\alpha^2}+1\right)+1-\bar{q}C_{M_\alpha}\left(1-\frac{C_{M_\beta}C_{L_\alpha}}{C_{L_\beta}C_{M_\alpha}}\right)}{\frac{1}{R_\alpha^2}\left(p^2\left(\frac{C_{M_\beta}}{C_{L_\beta}}+x_\alpha\right)+\frac{C_{M_\beta}}{C_{L_\beta}}\bar{\omega}_h^2\right)} \\
u_\xi \quad \text{Control:} \quad & x_s = \frac{p^2\left(\frac{C_{M_\xi}x_\alpha}{C_{L_\xi}R_\alpha^2}+1\right)+1-\bar{q}C_{M_\alpha}\left(1-\frac{C_{M_\xi}C_{L_\alpha}}{C_{L_\xi}C_{M_\alpha}}\right)}{\frac{1}{R_\alpha^2}\left(p^2\left(\frac{C_{M_\xi}}{C_{L_\xi}}+x_\alpha\right)+\frac{C_{M_\xi}}{C_{L_\xi}}\bar{\omega}_h^2\right)}
\end{aligned}
\tag{2.3.2}
$$

By choosing x_s such that the zero is between the poles (as in Fig. 2.5) a stable closed loop system results, in principle, for rate feedback. However, sensor placement will not work for all configurations or choices of actuators in practice. This is because the sensor location needed for stable feedback is sometimes found to be physically off of the typical section. For example, using the nominal typical section (Table 2.1) and design point 1 (below flutter) values, it is possible to find a stable sensor location for each method of actuation (although this causes a near pole-zero cancellation in the trailing edge flap actuation case y/u_β). However, all of the stabilizing sensor locations are found to be physically well off of the section at design point 2. Also, notice in Eq. 2.3.2 that if the desired zero locations are not complex conjugate pairs, the sensor position calculated will not be a real number.

The problems associated with sensor placement can be avoided by measuring both the plunge and pitch variables independently, and feeding back some linear combination of these outputs which stabilizes the system. One method of implementing such a stable control scheme is the use of full state feedback schemes such as the Linear Quadratic Regulator (LQR), which is discussed in the next section. Another SISO method of finding a stable feedback system from a single measurement to any actuator is to use a

stabilizing dynamic compensator. This can be done by classical compensation design (*e.g.*, using the methods of Bode or Nyquist) or optimal techniques (*e.g.*, solving the Linear Quadratic Gaussian problem).

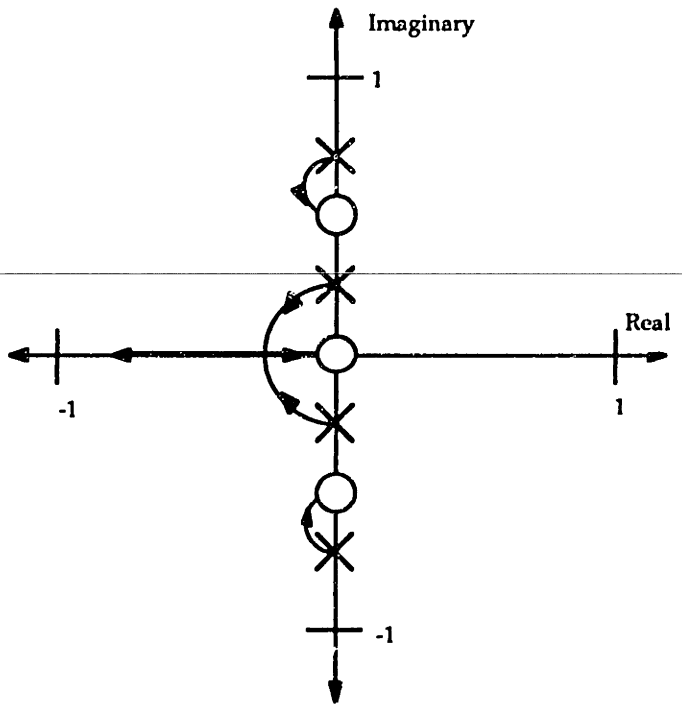

Figure 2.5. Desired loop transfer function pole and zero locations, and typical stable SISO root locus.

2.4 Full State Feedback Control

The problems associated with non-physical sensor placement solutions can be eliminated by independently measuring the state variables and feeding back combinations of them which yield stable closed loop systems. Using full state feedback is particularly advantageous because control laws may be developed which utilize various combinations of both the displacement and rate variables, and are not limited to combinations corresponding to locations physically on the airfoil.

The solution to the Linear Quadratic Regulator (LQR) problem is utilized in an attempt to provide stable well-regulated closed loop plants. Well-regulated closed loop plants have the desirable properties of relatively high damping and good disturbance rejection, which satisfies the control objective of the systems under consideration (*i.e.*, add damping). The optimal

gains **F** for full state feedback can be found by solving the LQR problem, which entails minimizing the scalar cost functional J

$$J = \int_0^\infty \left(\mathbf{x}^T\mathbf{Q}\mathbf{x} + \rho\mathbf{u}^T\mathbf{R}\mathbf{u}\right)dt$$

$$\text{where} \quad \mathbf{Q} = \mathbf{N}^T\mathbf{N} \quad \text{and} \quad \mathbf{z} = \mathbf{N}\mathbf{x} \tag{2.4.1}$$

In Eq. 2.4.1, **Q** is the penalty on the states and $\rho\mathbf{R}$ is the penalty on the control inputs which combines a scale factor ρ and an actuator weighting matrix **R**. The state cost penalty **z** is an evenly weighted combination of the plunge and pitch output variables normalized by their maximum values. The maximum values (Table 2.1) are determined from the deflection associated with a quadratic bending or linear twist distribution in a beam-like wing, and a maximum strain of one percent. Similarly, each control input is normalized by its maximum value. For the strain actuators, the maximum control input is computed using a maximum actuation strain of Λ=600$\mu\varepsilon$, which is considered a conservative value [Pan, Zhang, Bhalla and Cross, 1989]. The maximum deflection for the trailing edge flap is taken to be five degrees, and the maximum leading edge flap deflection is determined by equating its maximum hinge moment with that of the trailing edge flap, and found to be about two and a half degrees. For systems with more than one actuator input, all of the normalized control inputs are weighted evenly.

Since one goal of this investigation is to compare induced strain and conventional control surface actuation, each actuator was normalized by a reasonable estimate of the maximum control input available. The estimates are based on engineering judgment, laboratory experience and a desire to obtain a truly fair comparison of these fundamentally different actuating mechanisms. Because of the differences between the actuating mechanisms, it is interesting to compare the relative control authority of the actuators. Such a comparison can be found by examining the quasi-steady plunge and twist deformation produced by the maximum control input of each actuator. By letting the Laplace variable p equal zero and substituting the maximum control inputs into Eq. 2.1.1, the quasi-steady plunge and pitch displacements produced by each actuator input can be determined. This exercise shows that the strain and flap actuators cause roughly the same plunge displacement.

However, the strain actuators are capable of achieving twist deformations nearly seven times greater than those caused by the flap actuators. Note that this does not mean the analysis is biased toward strain actuation, since obtaining five degrees of high frequency trailing edge flap deflection would be a difficult engineering design problem. The implication is only that the strain actuators are capable of achieving higher quasi-steady twist deformations than the flaps for the configuration examined. For typical sections with other configurations, the relative quasi-steady control authority of the actuators will most likely be different.

The LQR solution yields the feedback gains $\mathbf{F}$ and the control inputs are given by $\mathbf{u}=-\mathbf{F}\mathbf{x}$. The gains represent the optimal combination of the states to be fed back to each actuator. The LQR solution was found to yield a loop transfer function, given by $\mathbf{F}\Phi\mathbf{B}$, which always had the stable alternating pole-zero pattern shown in Fig. 2.5 (although the zeros may not be on the imaginary axis). This result was found for any air speed or state control cost $\rho\mathbf{R}$, and state costs $\mathbf{N}$ which penalized some combination of the displacement states. However, the root locus drawn in the figure no longer applies for these multiple-output and perhaps multiple-input, multiple-output (MIMO) control schemes.

An interesting result is found in the case of "expensive" control, which implies a large control penalty (ρ goes to infinity) and therefore small gains. An asymptotic analysis shows that the feedback gains are given by

$$\mathbf{f} = \frac{1}{\sqrt{\rho}} \sum_i \sqrt{v_i^H \mathbf{Q} v_i} \left[\frac{\left(w_i^H \mathbf{b}\right)^H}{\left| w_i^H \mathbf{b} \right|} \right] w_i^H \qquad (2.4.2)$$

where v_i and w_i are the right and left eigenvectors of the system matrix $\mathbf{A}$, and the superscript H indicates the complex conjugate transpose.

For single control input systems, $(w_i)^H\mathbf{b}$ is a scalar so the entire quantity except for the last term w_i^H is a scalar. Therefore, the feedback gains are determined only by a weighted sum of the left eigenvectors of the open loop system. The weights are given by the contribution of the modes (observability) to the state cost chosen. In the "expensive" control case the LQR solution produces gains which are non-zero only on the rate state

variables. This result is true for any undamped single input system. The gains on the rate variables represent the optimal combination of states to use for rate feedback and thus the LQR solution is equivalent to a sophisticated rate feedback sensor placement algorithm (although the sensor does not have to be placed physically on the wing). In this low gain case the LQR solution attempts only to add damping to the system. The results show once again that damping is best added to an initially undamped structure by feeding back a stabilizing combination of the rate states. As the control becomes less expensive (ρ decreases), some displacement feedback will also be added.

Although LQR controllers can be employed to provide stable well-regulated closed loop systems, the performance of these compensators have limitations. This is especially true for the single control input case. Such restrictions become most apparent in the limiting case of "cheap" control. "Cheap" control is associated with a small control penalty and high feedback gains. As the control weight ρ goes to zero, the closed loop poles go to the stable finite MIMO zeros of the full Hamiltonian system if they exist, or otherwise to infinity along stable Butterworth patterns. The MIMO zeros of the full Hamiltonian system are found from the zeros of

$$\mathbf{H}(p) = \left[\mathbf{N}\Phi(-p)\mathbf{B}\right]^T\left[\mathbf{N}\Phi(p)\mathbf{B}\right] \tag{2.4.3}$$

These zeros are referred to as transmission zeros for square (number of measurements equals number of actuators) systems since they are the zeros of the MIMO loop transfer function $\mathbf{F}\Phi\mathbf{B}$, and "compromise" zeros for non-square systems [Emami-Naeini and Rock, 1984]. "Compromise" zeros do not appear in the MIMO loop transfer function.

For any system, the presence of "compromise" zeros implies that the closed loop poles associated with certain modes will not move along stable Butterworth patterns, causing a fundamental limit on the performance of the control system. This limitation is clearly illustrated in Figs. 2.6 and 2.7, which show the movement of the LQR closed loop pole locations of the nominal system at design point 1 (below flutter). The closed loop poles are plotted for control weights which decrease from a large value toward zero (from $\rho=10^{+4}$ to $\rho=10^{-4}$). As the control weight decreases, the control gain increases, causing the poles to move away from their open loop locations.

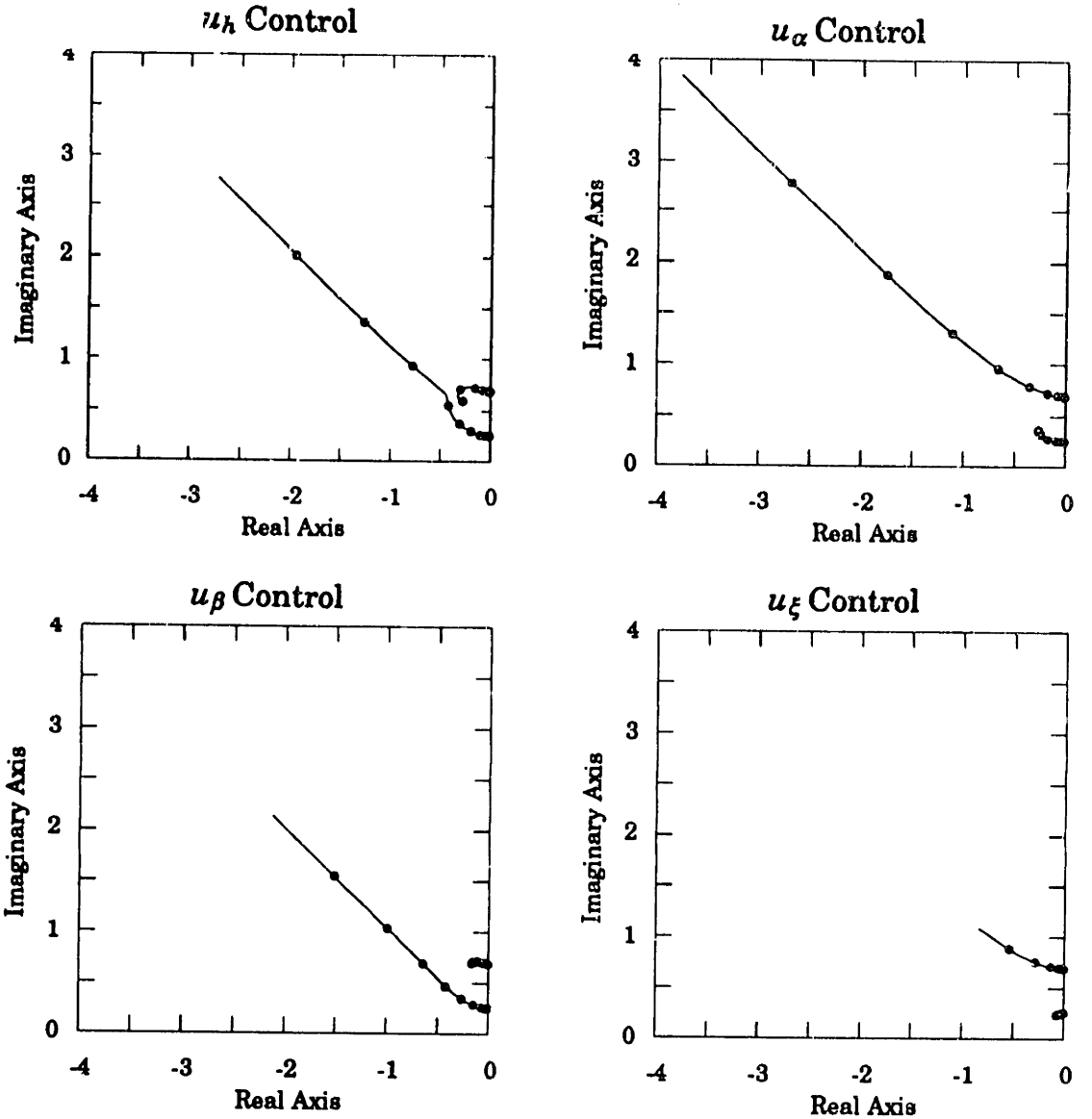

Figure 2.6. Locus of the full state feedback LQR closed loop poles as ρ goes toward zero ("cheap" control) for the four actuators acting individually. Both plunge and pitch displacements are penalized in the state cost.

The pole locations are plotted in Fig. 2.6 for the cases of the four actuators acting individually. Fig. 2.7 shows the closed loop pole locations for the cases of the actuators acting in pairs (2 inputs) and all controls acting together. When only one of the four available actuators is used, a "compromise" zero is found and only one pole is able to move along a stable Butterworth pattern. Such a zero indicates that a finite amount of state cost will persist, even when a large control effort is used. This point will be

further illustrated by the state versus control cost curves found in the following section. Notice that for the single input cases the induced strain bending u_h and trailing edge flap u_β actuators are able to move only the plunge pole along a stable Butterworth pattern. This indicates that these two actuators primarily influence the plunge mode. The induced strain torsion u_α and leading edge flap u_ξ actuators are able to move only the pitch pole along a stable Butterworth pattern, indicating that these two actuators primarily

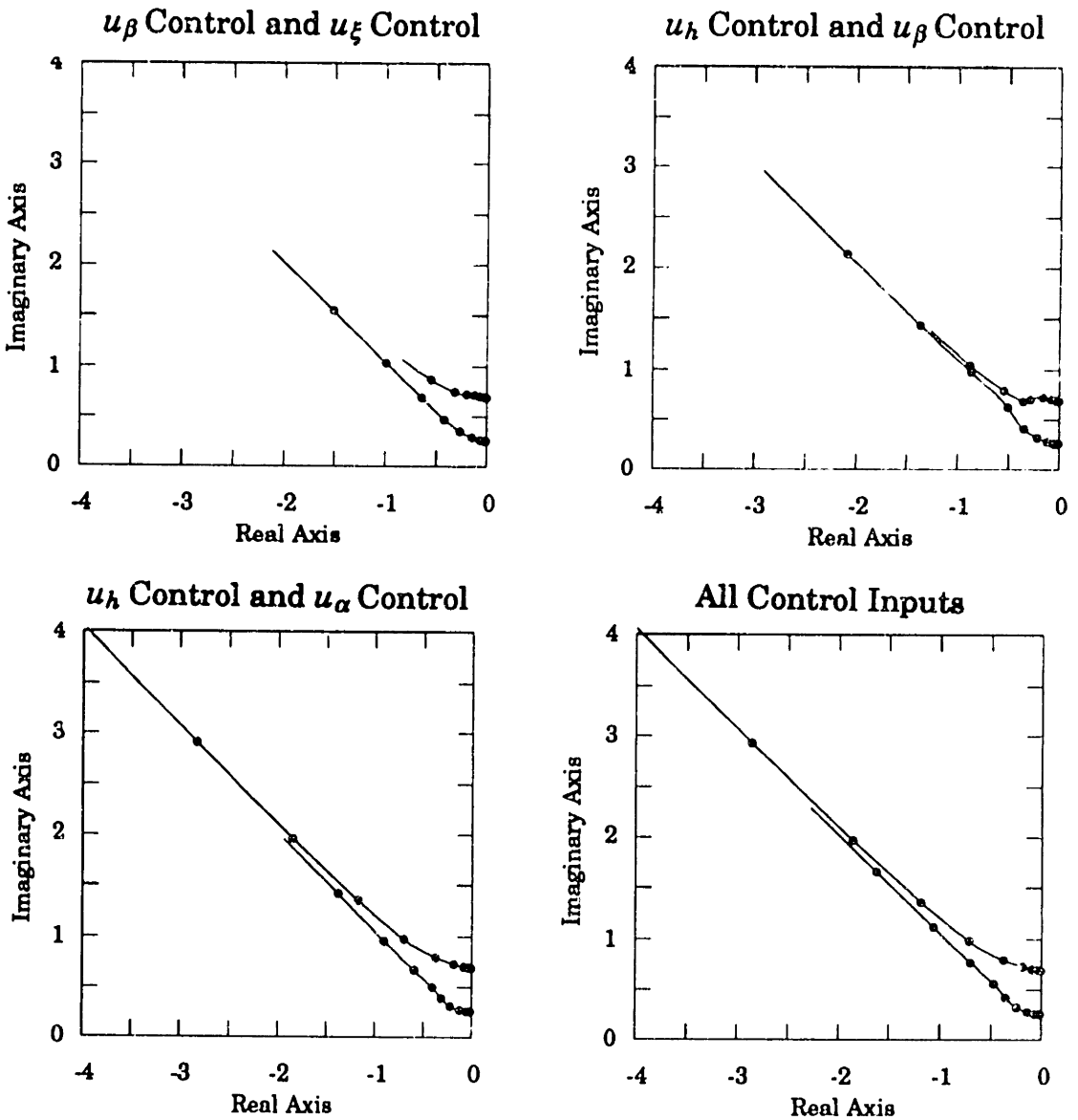

Figure 2.7. Locus of the full state feedback LQR closed loop poles as ρ goes to zero ("cheap" control) for multiple actuator input configurations. Both plunge and pitch displacement penalized in the state cost.

influence the pitch mode. Also notice that the bending actuator is more effective than the trailing edge flap actuator (*i.e.* , the poles are moved farther into the left half of the Laplace-plane), and the torsion strain actuator is significantly more effective than the leading edge flap actuator. In contrast with the single actuator case, no transmission or "compromise" zeros are found when combinations of two or more actuators are used (Fig. 2.7). In these cases, both poles move along stable Butterworth patterns, although for a fixed ρ some combinations are clearly more effective than others.

2.5 State Versus Control Cost Analysis

In order to qualitatively examine the effectiveness of the four actuators (bending strain actuation, torsion strain actuation, trailing edge flap deflection, and leading edge flap deflection) acting individually and in various combinations, several state versus control cost analyses are performed. The nominal section properties are taken to be those found in Table 2.1, and the section is analyzed at design points 1 (below flutter) and 2 (above flutter). The feedback gains are found by solving the LQR problem with a quadratic state and control cost consisting of the normalized displacement variables and control inputs, respectively. The displacement variables and control inputs are normalized by their maximum values as described above. The state cost equally penalizes the two normalized displacement states. The control inputs are also equally penalized for those designs consisting of more than one control input. In order to determine a finite cost, a broadband disturbance source is introduced in the form of a one degree broadband variation of the free stream air flow.

The results for design point 1 are shown in Figs. 2.8 and 2.9 in the form of state cost versus control cost curves. Each curve represents a different actuator configuration. In Fig. 2.8, curves are present for each actuator acting individually and all four acting together, the condition which creates the minimum state versus control cost. In Fig. 2.9, the cost associated with combinations of any two actuators acting together are plotted, as well as the curve for three actuators (bending strain, torsion strain, and trailing edge flap) and of all four actuators acting together. The curves are derived by fixing all of the parameters of the problem except the control cost weighting ρ, which is varied from $\rho=10^{+4}$ to $\rho=10^{-4}$. On these curves low control cost

values indicate "expensive" control weighting (high ρ), low gains, and therefore high state costs associated with large responses. High control cost values indicate "cheap" control weighting (low ρ), high gains, and lower state costs associated with smaller responses. The lower the state cost for any given control cost, the greater the effectiveness of the actuator or combination of actuators.

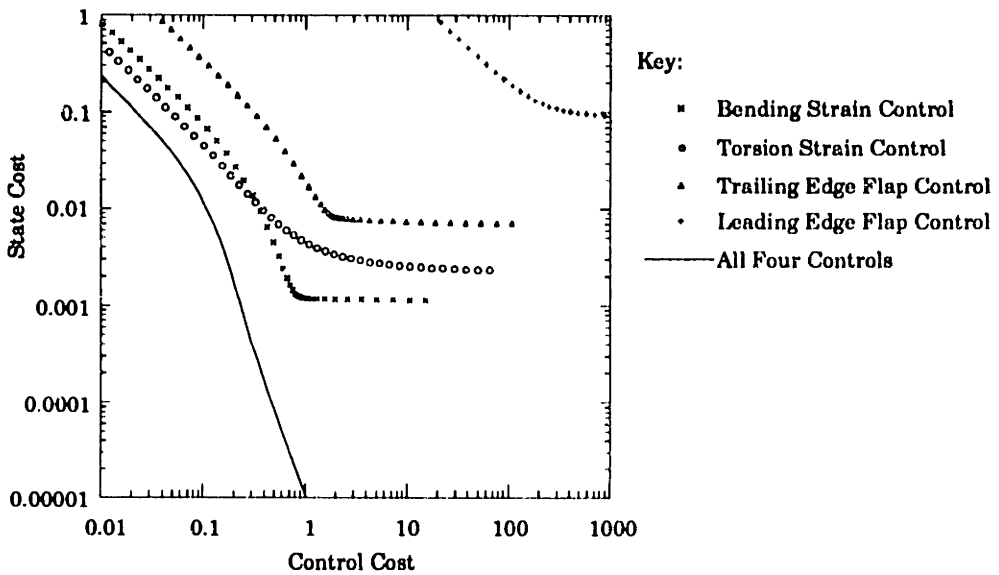

Figure 2.8. State versus control cost at design point 1 (below flutter) for systems with the four actuators acting individually and all actuators acting together. Gains were found by solving the LQR problem with both plunge and pitch displacement penalized in the state cost.

As can be seen in Fig. 2.8 for single control inputs, the torsion strain actuator u_α is most effective in the low gain "expensive" control case while bending strain actuator u_h is most effective for high gain "cheap" control. The cost curves show that the induced strain bending and torsion actuators are more effective than the conventional control surfaces throughout the entire range of control gains. It is also evident from the figure that the leading edge control surface is significantly less effective than the other actuators. Each curve associated with a single control input is observed to flatten out or asymptote to some finite state cost value. It is at this point that each actuator reaches its fundamental limit in terms of ability to exert control on the system. Note that the actuators have <u>not</u> saturated, but have imparted sufficient control to move one of the closed loop poles asymptotically near an open loop stable "compromise" zero of the Hamiltonian system, as shown in

Fig. 2.6. Since this closed loop pole will move no further despite larger control effort, the state versus control cost curve flattens. This is evidence of the fact that the presence of fewer independent actuators than important states in the system leads to "compromise" zeros, and places a fundamental limitation on the degree of control which can be exerted.

The curves associated with control schemes which utilize more than one actuator are shown in Fig. 2.9 and are, in general, much more effective than the single actuator systems. This is especially true for the "cheap" control high gain cases, where the improvement is observed to be over two orders of magnitude for some configurations. No fundamental performance limits are encountered in these multiple-input control systems for which the number of actuators (two or more) at least equals the number important states (those penalized) in the system. The state costs associated with the multiple actuator systems are shown to decrease in Fig. 2.9 as the control effort is increased throughout the entire range of control gains. As the gains increase, the system closed loop poles move outward along the stable Butterworth patterns, typified by the pairs shown in Fig. 2.7. The rate at which these poles move in the complex plane is directly related to the effectiveness of the multiple actuator system in question.

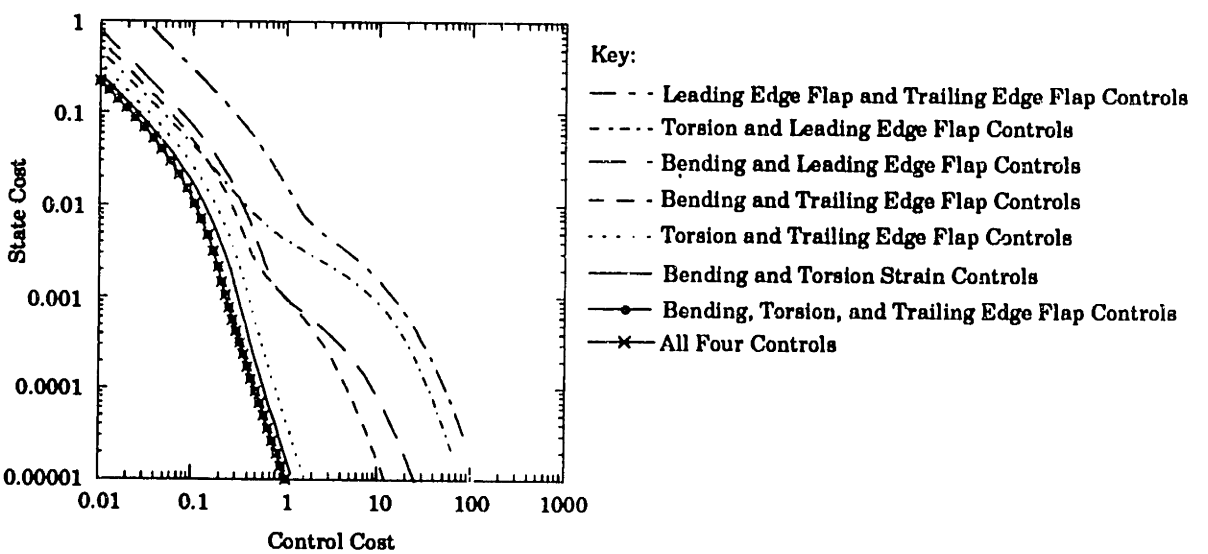

Figure 2.9. State versus control cost at design point 1 (below flutter) for systems with a variety of multiple input actuator combinations. Gains were found by solving the LQR problem with both plunge and pitch displacement penalized in the state cost.

Fig. 2.9 shows that the combination of the bending and torsion strain actuators, and the combination of the trailing edge flap and torsion strain actuators provide the best performance. These actuator combinations, bending and torsion strain or trailing edge flap and torsion strain, are found to be effective because they combine an actuator which effectively controls plunge (bending strain or trailing edge flap) with one which effectively controls torsion. In contrast, the bending strain and trailing edge flap actuator combination is much less effective since both actuators tend to control only the bending force on the wing and have little influence on the torsional moment. Fig. 2.9 also shows that the combination of "conventional" aerodynamic surfaces, leading edge flap and trailing edge flap, are the least effective actuator pair. In fact, all of the curves associated with the leading edge flap exhibit poor performance. The pairs which include the leading edge flap do not provide much more control performance than that given by the other actuators acting alone. The curves show that only after reaching the single actuator asymptote does the presence of the leading edge flap allow for more control to be effected. Finally, it is observed that the performance obtained using three actuators and all four actuators is only marginally better than that obtained using either the bending and torsion strain actuator combination or the trailing edge flap and torsion strain actuator combination. This is because there are only two states penalized and these two combinations of actuators can effectively control both states. Therefore, little additional benefit is obtained when more actuators are used than states important to the problem.

Fig. 2.10 shows similar results for individual actuators and several combinations of actuators at design point 2 (above flutter). The strain actuators once again are more effective than the conventional control surfaces. The bending and torsion strain actuators are the most effective, while the leading edge actuator provides only very small amounts of control and is not plotted in the figure. As with design point 1 (below flutter), actuator combinations are more effective than single actuator control schemes, with the combination of bending and torsion strain actuation or torsion strain and trailing edge flap actuation being most effective. Also notice the vertical low gain asymptotes in Fig. 2.10. Unlike the systems in Figs. 2.8 and 2.9 (below flutter) which have finite state cost for infinitesimal

gains, the systems of Fig. 2.10 (above flutter) are initially unstable, and the low gain asymptotes shown in the figure are associated with the minimum amount of control required to stabilize each system.

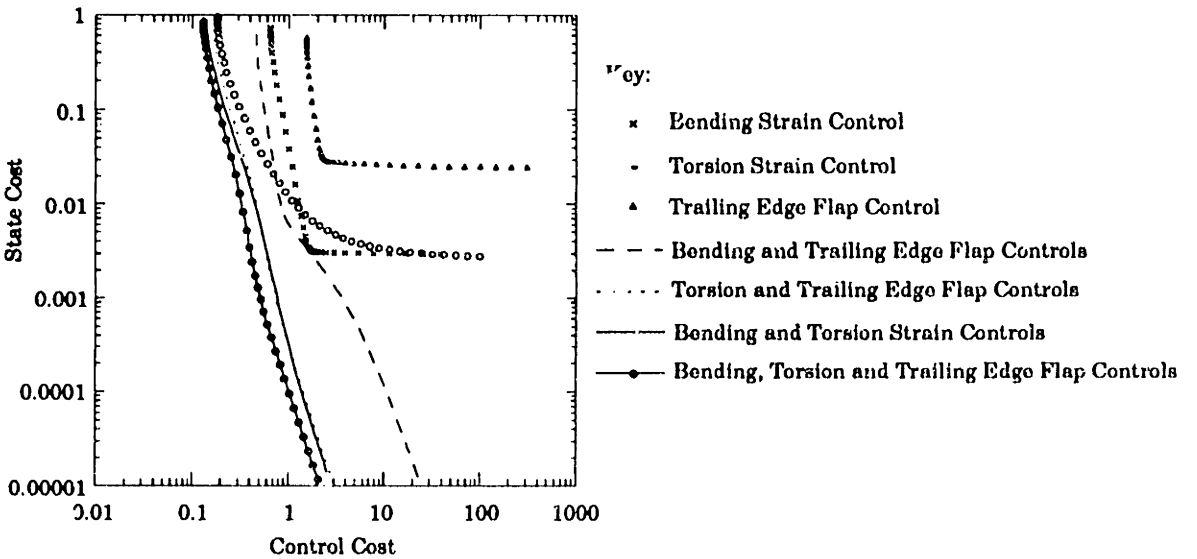

Figure 2.10. State versus control cost at design point 2 (above flutter) for systems with actuators acting individually and in multiple input combinations. Gains were found by solving the LQR problem with both plunge and pitch displacement penalized in the state cost.

2.6 Lessons Learned from the Typical Section

A typical section model which includes the applied forces and moments produced by induced strain actuation as well as conventional aerodynamic control surfaces, was developed in this chapter. The typical section was analyzed to provide the tools necessary for understanding the fundamental mechanisms and limitations involved in aeroelastic control, and for comparing alternative control methods. Classical control techniques were employed to analyze various single-input, single-output (SISO) control schemes. It was found that both the poles and zeros of the individual SISO loop transfer functions moved rapidly with air speed, and that the zeros were often in undesirable locations for effecting SISO control, including being non-minimum phase. It was also found that simple gain feedback of the displacement or rate state variables would not stabilize the systems considered, and that it was necessary to use some combination of the rate states in order to achieve a stable output feedback loop.

Stable feedback loops were found using sensor placement techniques and the solution to the Linear Quadratic Regulator (LQR) problem. For the limiting case of low gain "expensive" control, the LQR solution was found to yield a solution similar to that of sensor placement (*i.e.*, a stabilizing combination of the rate states), but was not restricted to gain ratios which corresponded to physical sensor locations. A state versus control cost analysis was performed using the solution to the Linear Quadratic Regulator problem for a variety of actuator and sensor combinations. It was found that when fewer actuators are used than important states (determined by the state cost penalty), fundamental control limitations are identified by the finite multiple-input, multiple-output (MIMO) transmission or "compromise" zeros. The closed loop poles go to these zeros, rather than along stable Butterworth patterns in the case of high gain "cheap" control, limiting the control authority which can be applied to the system. It was found that such limitations can be avoided by utilizing at least as many control actuators as important states in the system.

The state versus control cost comparisons demonstrated that strain actuation is an effective means of controlling aeroelastic systems and a viable alternative to conventional articulated control surfaces. Either bending or torsion strain actuation is as effective alone as trailing edge flap actuation, and much more effective than leading edge flap actuation. Thus, only by incorporating strain actuation can an effective second actuator be added to the system, and true high gain performance be achieved.

2.A Appendix: Equivalent Strain Actuator Forces

The equivalent strain actuator forces acting on the typical section are found by equating the deflections w of a uniform cantilever beam-like wing due to a point force and a strain actuator induced bending moment. The three-quarter span deflection due to a point force at the three-quarter span is

$$w_F = \left(\frac{9}{64}\right)\frac{L^3}{(EI)_s}F \tag{2.A.1}$$

where F is the equivalent force to be found. The three-quarter span deflection due to a strain actuator induced uniform bending moment is found by the pin force method [Crawley and de Luis, 1987] to be

$$w_M = \left(\frac{9}{32}\right)\frac{L^2}{(EI)_s}\left(\frac{1}{6+\psi}\right)E_s t_s^2 (2b)\Lambda \qquad \psi = \frac{E_s t_s}{E_a t_a} \tag{2.A.2}$$

where Λ is the free strain of the strain actuator and ψ is the relative substructure/actuator stiffness ratio. In Eqs. 2.A.1 and 2.A.2, E, I, t and b are the elastic modulus, area moment of inertia, thickness and semi-chord, respectively. The subscript 's' denotes the beam substructure and the subscript 'a' refers to the attached actuators. In both expressions, w is the deflection of the elastic axis at the three-quarter span. Equating the deflections (w_F and w_M) for the beam-like wing, and solving for the equivalent force F yields

$$F = \left(\frac{2}{L}\right)\left(\frac{1}{6+\psi}\right)E_s t_s^2 (2b)\Lambda \tag{2.A.3}$$

The torsional stiffness, by which the equivalent forces are normalized, is found from the three-quarter span rotation θ of the beam-like wing subjected to a tip torque τ

$$\theta = \left[\left(\frac{3}{4}L\right)\left(\frac{1}{GJ}\right)\right]\tau = \left[\frac{1}{K_\alpha}\right]\tau \tag{2.A.4}$$

The normalized equivalent force u_h is then found from Eqs. 2.1.1, 2.A.3 and 2.A.4 by assuming a rectangular wing cross-section and that the torsional stiffness of the strain actuator is negligible compared to that of the beam substructure

$$u_h = \frac{Fb}{K_\alpha} = \frac{9}{2}\left(\frac{1+\nu}{6+\psi}\right)\left(\frac{2b}{t_s}\right)\Lambda = 0.3656\left(\frac{2b}{t_s}\right)\Lambda \tag{2.A.5}$$

where Possion's ratio ν and the relative stiffness ratio ψ are taken as 0.3 and 10.0, respectively, in this study.

Calculating the equivalent moment u_α is not as straight forward as finding the equivalent force u_h because the problem is inherently two-dimensional. Creating an equivalent moment requires that either the strain

actuator possesses a free shear strain term (not present in piezoceramics) or the substructure exhibits bending/twist or extension/twist coupling (requiring a more complete [Crawley and Lazarus, 1991] analysis). However, an effective shear strain term can be created in a piezoceramic by properly constraining the actuator in the longitudinal and transverse directions. Imposing such constraints on a strain actuator produces an equivalent moment in the same manner (physically) as actuating an unconstrained piezoceramic bonded to a substructure with bending/twist coupling. Thus, the strain actuators are assumed to be fully constrained in the transverse direction, unconstrained in the longitudinal direction and mounted at 45 degrees, yielding an equivalent moment u_α equal to one half the equivalent force u_h based on the maximum in-plane shear strain given by Mohr's circle.

Chapter 3. Optimal Actuator Placement and Scaling Laws

The typical section analysis showed the advantages of using strain actuators and the benefits provided by multiple actuator inputs. By taking advantage of multiple-input strain actuation, true high-authority control can be effected. However, the typical section results were obtained only for specific equivalent strain actuator forces acting on the section, and no mention was made of how the size and position of the stain actuators were selected. Thus, there exist a need to develop and define the parameters important to selecting and incorporating strain actuators in active structures. The purpose of this chapter is therefore to develop models useful for determining the size and placement of strain actuators in lifting surfaces, and to develop the scaling laws needed to generalize the results obtained to representative active wings.

3.1 Optimal Strain Actuator Placement.

In the following study several assumptions are made in order to gain insight into the problem of obtaining maximum control authority from induced strain actuated structures, while minimizing the weight added. The assumptions used greatly simplify the mathematics, yielding a model that retains the fundamental physics involved in deforming a lifting surface. The analytic work provides the governing equations for strain actuated wings and design guidelines for typical active lifting surfaces. Specifically, a simplified model is used to obtain closed form solutions for optimal actuator placement and size, and optimal and suboptimal induced camber and twist, and the minimum additional weight for a given control requirement. The relations developed can be used to design actual active lifting surfaces. Although many effects which are important for detailed modelling, such as those produced by the plate boundary conditions at the root, are omitted; the objectives of this first order analysis are well served by the models developed.

Fig. 3.1 shows a cantilevered plate-like aeroelastic lifting surface, and a representative segment of the wing. The section is free to bend along the chord (induced camber actuation) as well as twist along the span (induced twist actuation) as shown in the figure. The section is assumed to have uniform geometric and material properties which are representative of the

entire lifting surface, as does a typical section. Each section is assumed to have an elastic axis which coincides geometrically with both the mid-plane and the mid-chord, and is symmetric about these planes.

The governing equations for these deformable section are found by applying Bernoulli-Euler beam or Kirchhoff plate theory, and including the effects of the strain actuation as done in Crawley and Lazarus [1991]. These relations are used to find the induced chordwise bending (camber) or spanwise twist (angle of attack) induced in the deformable section by the strain actuators. The optimal actuator placement and size relations are found by matching the structural stiffness of the wing skin and the actuator layer. The deformations induced in sections with optimally placed actuators are also found.

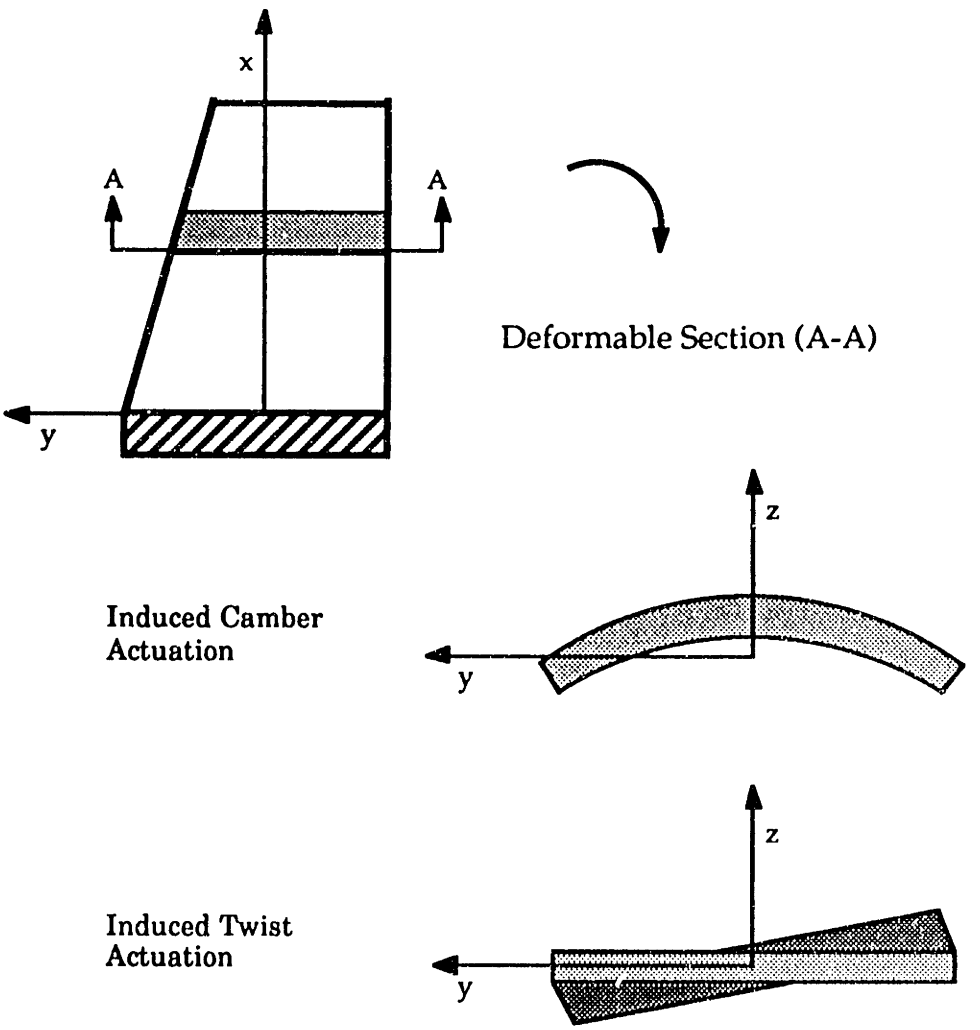

Figure 3.1. Strain actuated plate-like lifting surface, and an induced camber and induced twist actuated deformable section.

In the analysis which follows, the governing relations for both camber and twist control are developed. In addition, a procedure is outlined for the design of a nominal strain actuated airfoil, which can be used for comparison with a conventional control surface actuated wing in terms of control authority and weight penalty associated with the actuator system.

Structural Optimization For Camber Control

For the purpose of analyzing camber control the deformable section is assumed to act like a beam bending along the chord when actuated by induced strain actuator layers distributed symmetrically about the neutral axis and acting in opposition. In this configuration the chordwise bending of the section is governed by the following moment curvature relation

$$\left(\frac{EI}{L_i}\right)_y \frac{\partial^2 w}{\partial y^2} = (m_\Lambda)_y \tag{3.1.1}$$

where L_i is the length of the deformable section along the span, and m_Λ is the equivalent actuation moment per unit length developed by the induced strain actuators which causes the structure to deform. This equivalent moment is equal to the integral though the wing thickness of the product of the actuation strain Λ, Young's Modulus E, and offset from the neutral axis z

$$(m_\Lambda)_y = \int_z E\Lambda_y z\,dz \tag{3.1.2}$$

The wing stiffness and equivalent actuation moment developed are determined by the internal geometry of the lifting surface. Fig. 3.2 shows the box wing geometry analyzed in this study. The section is assumed to be made of two wing skins, a layer of distributed strain actuators, and a hollow core. The wing skins are of identical thickness. One lies above, and one lies below the neutral axis. Each skin is equidistant from the neutral axis and includes a layer of distributed induced strain actuators. The wing skin and actuator thickness (t_a plus t_s) is assumed to be much less than its distance from the neutral axis to the center of the skin (Z_{ms}) or actuator (Z_{ma}). The hollow core between the wing skins is assumed to be composed only of a perfect (and weightless) shear web.

Applying the above assumptions, the chordwise bending stiffness, or mechanical impedance, of the lifting surface is found to come from only the wing skins and the induced strain actuator layers

$$\left(\frac{EI}{b}\right)_y = 2\left[E_s t_s Z_{ms}^2 + E_a t_a Z_{ma}^2\right]$$
$$\text{for} \quad t_s, t_a << Z_{ms}, Z_{ma} \tag{3.1.3}$$

Substituting the equivalent moment (Eq. 3.1.2) and the mechanical impedance (Eq. 3.1.3) into the moment curvature relation (Eq. 3.1.1) yields an expression for the induced curvature

$$\kappa_y = \frac{E_a t_a Z_{ma} \Lambda}{E_a t_a Z_{ma}^2 + E_s t_s Z_{ms}^2} \tag{3.1.4}$$

where the induced strain actuators, located an equal distance from the neutral axis, are operated in opposition to induce curvature in the structure along the chordwise dimension. Inducing such a curvature is equivalent to changing the camber of the lifting surface. Rearranging Eq. 3.1.4, the induced camber is found to depend on the distance of the wing skin Z_{ms} and the actuator layer Z_{ma} above the neutral axis, and the wing skin and the actuator layer stiffness

$$\kappa_y = \frac{Z_{ma} \Lambda}{Z_{ma}^2 + \psi Z_{ms}^2} \qquad \psi = \frac{E_s t_s}{E_a t_a} \tag{3.1.5}$$

where ψ is the relative stiffness of the wing skin to the induced strain actuator. Upon close examination of the induced camber equation (Eq. 3.1.5), it can be seen that the amount of camber obtainable through induced strain actuation is maximized by correctly matching the bending stiffness, or mechanical impedance, of the wing skin and that of the distributed actuator layer. If the actuator layer is placed at a distance above the neutral axis that is less than that which yields maximum effectiveness, it is force limited. On the other hand, an actuator which lies a greater distance from the neutral axis than the distance which gives maximum effectiveness is stroke limited.

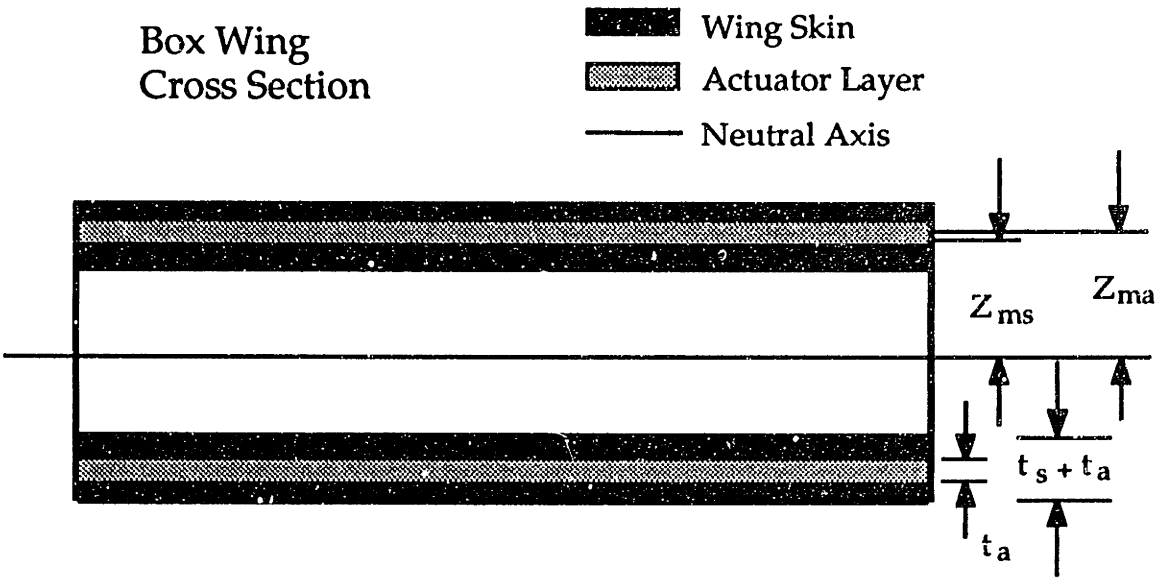

Figure 3.2. Box wing internal geometry of a lifting surface with induced strain actuators.

The optimal actuator layer height, which is found by differentiating the expression for the induced camber (Eq. 3.1.5) by the distance the actuator layer lies above the neutral axis Z_{ma}, is

$$Z_{ma} = \sqrt{\psi}\, Z_{ms} \tag{3.1.6}$$

Eq. 3.1.6 shows that the optimal position for the distributed actuator layer is only dependent on ψ, the relative stiffness of the wing skin and the actuator layer. This expression, which relates the optimal actuator layer height to the geometrical and material properties of the wing, can be used in two ways. First, the optimal actuator size can be found for a given actuator layer. In some cases the actuator placement will be fixed by other constraints, and the actuator thickness can be chosen to achieve an optimal configuration. Alternatively, it may be desirable to locate the optimal location of a given actuator. Since the actuator layer must be physically connected to the airfoil, the height of this layer above the neutral axis Z_{ma} must be roughly equal to or less than the height of the wing skin Z_{ms}. Thus for practical optimal designs to be achieved, the relative stiffness ratio ψ must be less than or equal to unity. However the relative stiffness ratio is typically greater than unity for actuators bonded to structural members such as wing skins. This

indicates that it may not be possible to achieve optimal designs, and that Z_{ma} should be made as large as physically possible by bonding the actuator layer to the interior or exterior wing skin surface, or embedding it in the skin. It also indicates that the actuator stiffness E_a should be chosen as large as possible. The high relative stiffness ratio of representative wings typically causes suboptimal actuation in a force limited mode even when Z_{ma} and E_a are large.

Sections with actuators placed according to Eq. 3.1.6 are considered optimal since it is in this configuration that the maximum camber is obtained through induced strain actuation for a given airfoil section and actuator. A non-dimensional expression for the optimal induced camber is found by substituting the optimal actuator placement expression (Eq. 3.1.6) into the camber equation (Eq. 3.1.5) and integrating over the chord

$$\left(\frac{\Delta w}{c}\right)_{\text{opt}} = \frac{1}{2}\sqrt{\frac{1}{\psi}}\left[\frac{c}{2Z_{ms}}\right]\Lambda \tag{3.1.7}$$

where $2Z_{ms}/c$ is approximately equal the the wing thickness ratio. The optimal induced camber is a function of just three non-dimensional quantities. These quantities are the inverse square root of the relative stiffness ratio ψ, the inverse of the airfoil thickness ratio, and the actuation strain Λ produced by the induced strain actuators. Eq. 3.1.7 shows that more camber is induced if the airfoil is thin, the relative stiffness ratio is kept small (Z_{ma} and E_a large), and if the actuation strain is large.

Structural Optimization for Twist Control

In addition to camber control, induced twist actuation can be used for aeroelastic control. By inducing twist curvature in the lifting surface, the local airfoil angle of attack may be regulated to effect control. A deformable section analysis can be employed, in a manner similar to the camber control case to determine the equations governing the transfer of actuation strain to twist curvature. In this analysis the deformable section is assumed to act like a plate twisting along the spanwise dimension.

The deformable plate section is assumed to bend, twist and extend along the spanwise dimension, as well as exhibit chordwise bending. The moment curvature relation for such a section is [Lazarus and Crawley, 1989]

$$\begin{bmatrix} \mathbf{A} & \mathbf{B} \\ \mathbf{B} & \mathbf{D} \end{bmatrix} \begin{Bmatrix} \varepsilon \\ \kappa \end{Bmatrix} = \begin{bmatrix} \mathbf{N}_\Lambda \\ \mathbf{M}_\Lambda \end{bmatrix}$$
$$\mathbf{N}_\Lambda = \int_z \mathbf{Q} \Lambda \, dz \qquad \mathbf{M}_\Lambda = \int_z \mathbf{Q} \Lambda \, dz \tag{3.1.8}$$

where **A**, **B**, and **D** are the plate extension, coupling and bending stiffnesses, $\mathbf{N}_\Lambda$ and $\mathbf{M}_\Lambda$ are the actuation force and moment per unit length, and **Q** is the reduced stiffness of the plate section. Note that the extension, coupling and bending stiffnesses are composed of terms from both the wing skins and actuator layers, which lie symmetrically about the neutral axis; while the actuation forces and moments depend only on the strain actuator layer properties. Eq. 3.1.8 can be simplified by neglecting the extension ε_y and bending κ_{yy} along the chordwise dimension. Further, the twisting force $(N_\Lambda)_{xy}$ and moment $(M_\Lambda)_{xy}$ created by the strain actuators can be set to zero since common induced strain actuators produce no shear strain. These assumptions allow for the twist curvature, which will be analyzed for induced twist actuation through bending/twist coupling and induced twist actuation through extension/twist coupling, to be solved for explicitly. In each case the internal geometry will be assumed to be that of the box wing (Fig. 3.2).

Twist Actuation Through Bending / Twist Coupling

When the distributed actuators are commanded to act in opposition, so that a spanwise bending moment $(M_\Lambda)_x$ is imposed on the deformable section, a twist curvature is induced through the section bending/twist coupling (D_{16}). This twist curvature can be found by setting the coupling stiffness **B** to zero and applying the aforementioned assumptions to Eq. 3.1.8

$$\kappa_{xy} = -\frac{D_{16}}{\left[D_{11}D_{66} - D_{16}^2\right]} 2(E_L)_a t_a Z_{ma} \Lambda_x \tag{3.1.9}$$

where $(E_L)_a$ is the engineering constant associated with the elastic modulus of the actuator layer in the longitudinal (spanwise) direction.

Maximum twist curvature, induced angle of attack, and the optimal actuator layer placement is found by differentiating Eq. 3.1.9 with respect to the actuator layer height and setting the result equal to zero. This yields a quadratic expression in Z_{ma}. A rough approximation for the optimal height of the actuator layer is obtained using a binomial expansion

$$Z_{ma} \cong \sqrt{\psi \frac{\left(1-\psi_D^2\right)}{1+\frac{(E_L)_s(G_{LT})_a}{(E_L)_a(G_{LT})_s}}} Z_{ms}$$

$$\text{where} \qquad \psi_D = \frac{D_{16}}{\sqrt{D_{11}D_{66}}} \tag{3.1.10}$$

In Eq. 3.1.10 E_L and G_{LT} are the engineering constants associated with the elastic and shear modulus of the wing skin and actuator layer. The relation above shows that the optimal actuator height is proportional to the distance the skin lies above the neutral axis and the square root of the relative stiffness ratio, as was found for camber control. In addition, the optimal position for twist control is dependent on the bending/twist coupling parameter ψ_D, and the engineering constants of the wing skin and actuator layer. The bending/twist coupling parameter is a non-dimensional measure of the amount of coupling inherent in the wing skin, and has a value between one and negative one [Weisshaar and Foist, 1985]. This parameter, along with the ratio of engineering constants, causes the optimal height for this case to be lower then that of the induced camber case.

A measure of the maximum lift obtained through induced twist can be found by substituting the optimal height equation (Eq. 3.1.10) into the twist curvature relation (Eq.3.1.9) and integrating over the section. This gives an expression which shows the dependence of the induced twist, from the inner to the outer spanwise edge of the section, on the geometric and material properties of the lifting surface.

$$\theta \propto \left(\frac{L_i}{c}\right) \frac{\psi_D}{\sqrt{\psi\left(1-\psi_D^2\right)}} \frac{1}{\sqrt{1+\frac{(E_L)_s(G_{LT})_a}{(E_L)_a(G_{LT})_s}}} \left(\frac{c}{2Z_{ms}}\right) \Lambda_x \tag{3.1.11}$$

where L_i is the length of the deformable section. This optimal twist expression is slightly more complicated but very similar to the optimal induced camber equation (Eq. 3.1.7). The optimal twist is dependent on the same quantities as was the optimal induced camber, such as the relative stiffness ψ, the thickness ratio, and the actuation strain Λ. However, in this case the section aspect ratio, the bending/twist coupling parameter ψ_D, and the ratio of engineering constants are also important.

Twist Actuation Through Extension / Twist Coupling

The second method of inducing twist is through extension/twist coupling and extensional actuation. In this analysis, typical plate sections with extension/twist coupling, but no extension/bending coupling, are considered. The actuators on either side of the neutral axis are commanded to act in unison, rather than in opposition, to produce extensional strains and equivalent extensional forces. Therefore spanwise twist is induced in the sections without either chordwise or spanwise bending. The twist induced from extension actuation and extension/twist coupling is governed by the following relation [Lazarus and Crawley, 1989]

$$\kappa_{xy} = -\frac{B_{16}}{\left[A_{11}D_{66} - B_{16}^2\right]}\left(N_\Lambda\right)_x \tag{3.1.12}$$

In Eq. 3.1.12, B_{16} is the extension/twist coupling of the wing skin, and $(N_\Lambda)_x$ is the equivalent extensional force per unit length developed along the spanwise dimension by the strain actuator layers.

Since twist is induced by an equivalent force (and extension/twist coupling), rather than an equivalent moment (and bending/twist coupling), the actuator layer has no optimal position above the neutral axis. Hence, the maximum twist induced in the lifting surface is independent of the actuator layer placement (as long as it is symmetric). However, there is still an impedance matching problem to consider since the actuator provides both forcing and stiffness. By differentiating the twist curvature equation (Eq. 3.1.12) by the actuator thickness t_a, the optimal actuator layer thickness is found

$$t_a = \sqrt{\frac{(E_L)_s (G_{LT})_s}{(E_L)_a (G_{LT})_a}} \frac{Z_{ms}}{Z_{ma}} t_s \tag{3.1.13}$$

Eq. 3.1.13 shows that the optimal thickness is dependent essentially on the ratio of the extensional stiffness of the wing skin and the distributed actuator layer, or mechanical impedance, as expected. The optimal induced twist curvature can be found by substituting the optimal actuator thickness expression (Eq. 3.1.13) back into the expression for induced twist through extension/twist coupling (Eq. 3.1.12). An expression for the optimal induced twist can be found by integrating over the lifting surface as done for the bending/twist coupling case.

3.2 Strain Actuator Design and Associated Weight

The deformable section analysis showed that an optimal configuration is achieved for practical configurations when the actuator layer distance from the neutral axis Z_{ma} is large. However, the greatest height which can be achieved physically is approximately the height at which the wing skin lies above the neutral axis (the difference in performance between bonding the actuators to the interior or exterior of the wing skin, or embedding the actuators in the skin is negligible since $t_a << Z_{ma}$). These performance considerations, along with other factors such as actuator type, geometric space constraints, material compatibility, damage protection and ease of manufacturing, make bonding the actuators to the interior surface of the wing skins a reasonable actuator placement choice. Such a configuration is shown in Fig. 3.3. From geometry the height of the actuator layer can be easily determined

$$Z_{ma} = Z_{ms} - \tfrac{1}{2}(t_a + t_s) \tag{3.2.1}$$

Additionally, it may be desirable to have the total (skin plus actuator layer) skin thickness of the wing with actuators equivalent to the original skin thickness t_{so}.

$$t_s + t_a = t_{so} \tag{3.2.2}$$

Thus, the actuator layer would just replace a portion of the original wing skin. This geometry was chosen in order to keep the wing stiffness with the

induced strain actuators close to the original wing stiffness, and to reduce the weight added by the actuators.

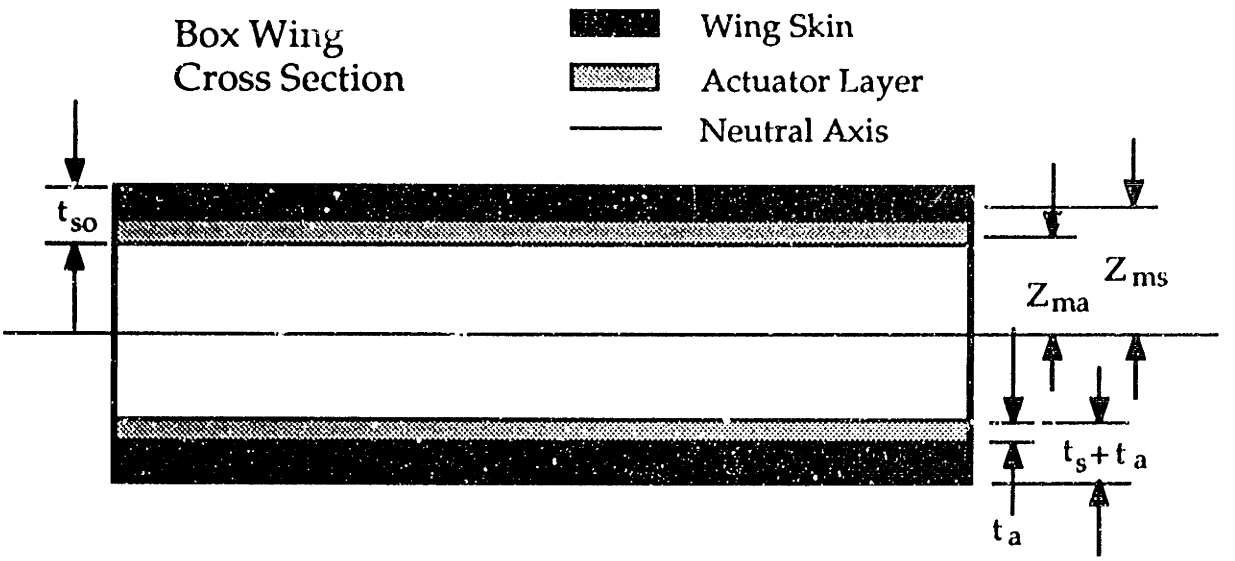

Figure 3.3. Actuator layer bonded to under surface of wing skin.

Optimal Actuator Thickness

In the configuration described, all the design variables have been fixed except the thickness of the actuator layer. Therefore, in order to achieve optimal performance, the actuator layer thickness t_a is chosen which optimizes the given actuator layer height Z_{ma}. This optimal thickness is calculated by substituting the geometric constraints (Eqs. 3.2.1 and 3.2.2) into the optimal height equations (Eqs 3.1.6 and 3.1.10) and solving for the actuator layer thickness t_a.

$$t_a \text{ (camber)} = \frac{t_{so}}{\left[\left(\frac{Z_{ma}}{Z_{ms}}\right)^2 \frac{(E_L)_a}{(E_L)_s} + 1\right]} \tag{3.2.3}$$

$$t_a \text{ (twist)} \cong \frac{t_{so}}{\left[\left(\frac{Z_{ma}}{Z_{ms}}\right)^2 \frac{(E_L)_a}{(E_L)_s}\left[\frac{1+\frac{(E_L)_s(G_{LT})_a}{(E_L)_a(G_{LT})_s}}{1-\psi_D^2}\right] + 1\right]} \tag{3.2.4}$$

Eqs. 3.2.3 and 3.2.4 show that the actuator layer thickness will always be less than the original wing skin thickness, which means that practical designs are possible using this configuration. By substituting the material and geometric properties of a typical wing, actual optimal actuator layer thicknesses can be calculated.

Actuator Layer Weight Penalty

The weight penalty associated with using induced strain actuators can be assessed in terms of percent weight added. The percent weight added is easily calculated from the original total weight and the final total weight (with the actuator layer)

$$\text{Original Total Weight} = \sum_{i=1}^{n} S_i \left(t_{so}\right)_i \rho_s \tag{3.2.5}$$

$$\text{Final Total Weight} = \sum_{i=1}^{n} S_i \left[\left(t_s\right)_i \rho_s + \left(t_a\right)_i \rho_a\right] \tag{3.2.6}$$

where all the weight has been assumed to come from either the wing skin or the actuator layer. The percent weight added is found by dividing Eq. 3.2.6 by Eq. 3.2.5 and substituting the final skin thickness relation (Eq. 3.2.6).

$$\text{Added Weight } (\%) = \sum_{i=1}^{n} \left(\frac{t_a}{t_{so}}\right)_i \left(\frac{\rho_a}{\rho_s} - 1\right) 100 \tag{3.2.7}$$

The added weight depends only on the ratio of actuator thickness to original wing skin thickness and actuator density to skin density. As the actuator thickness and density decreases, so does the added weight. And, if the density of the actuator is equal to that of the wing skin, no weight is added.

For some designs, the amount of weight added, dictated by the actuator thickness and density, for an optimal configuration is not tolerable. When the added weight is limited by design constraints, the actuator thickness must be reduced from the optimal thickness to some acceptable thickness. Such a configuration is considered suboptimal, since neither the optimal actuator height or thickness is achieved. However, a suboptimal design is not necessarily a poor design, especially if the particular configuration meets all the performance objectives.

3.3 Scaling Laws.

Sections 3.1 and 3.2 identify the parameters important for selection and placement of strain actuators in active structures. Such parameters serve as useful tools for designing controlled structures such as active lifting surfaces. In the design of model active structures, the laws governing the scaling of the important parameters also need to be determined. The scaling laws must be known in order to design models with non-dimensional properties equivalent to those of the full scale articles, so that experimental results can be applied to actual aeroelastic structures. For these reasons, the basic active lifting surface scaling laws are found in this section.

Including the effects of chordwise bending (*i.e.*, camber) is important for predicting the behavior of plate-like structures. Similarly, proper modeling of the three-dimensional unsteady aerodynamic forces associated with the deflections of lifting surfaces is essential for a full aeroelastic analysis. However for the purpose of identifying the scaling laws fundamental to strain actuated aeroelastic control, it is unnecessary to undertake such a detailed analysis. The important parameters can be identified using simple steady strip theory aerodynamics, and a beam-like structure which is free to bend and twist along the span, such that the out-of-plane displacements w are described by

$$w(x,y) = w(x) + y\theta(x) \tag{3.3.1}$$

The differential aeroelastic equations of motion are found by applying these assumptions to the strain actuated plate energy equation (5.1.1). The out-of-plane solution for periodic motion is found using a partial Ritz analysis, similar to that of Jensen and Crawley [1984], to be

$$D_{11}\frac{\partial^4 w}{\partial x^4} + 2D_{16}\frac{\partial^3 \theta}{\partial x^3} + \lambda^2 \mu w = M_\Lambda \frac{\partial^2 \Lambda}{\partial x^2} \tag{3.3.2a}$$

$$-24D_{16}\frac{\partial^3 w}{\partial x^3} + c^2 D_{11}\frac{\partial^4 \theta}{\partial x^4} - 48D_{66}\frac{\partial^2 \theta}{\partial x^2} + \lambda^2 \mu c^2 \theta = qcC_{l_a}\theta \tag{3.3.2b}$$

Non-dimensionalizing the aeroelastic equations yields

$$\overline{D}_{11}\frac{\partial^4\overline{w}}{\partial\overline{x}^4}+\left[\frac{L}{c}\right]2\overline{D}_{16}\frac{\partial^3\overline{\theta}}{\partial\overline{x}^3}+\left[\frac{\lambda_o^2\mu_o L^4}{D_o}\right]\overline{\lambda}^2\overline{\mu}\overline{w}$$
$$=\left[\frac{M_{\Lambda_o}L^2}{hD_o}\right]\overline{M}_\Lambda\frac{\partial^2\Lambda}{\partial\overline{x}^2} \tag{3.3.3a}$$

$$-\left[\frac{L}{c}\right]24\overline{D}_{16}\frac{\partial^3\overline{w}}{\partial\overline{x}^3}+\overline{D}_{11}\frac{\partial^4\overline{\theta}}{\partial\overline{x}^4}-\left[\left(\frac{L}{c}\right)^2\right]48\overline{D}_{66}\frac{\partial^2\overline{\theta}}{\partial\overline{x}^2}+\left[\frac{\lambda_o^2\mu_o L^4}{D_o}\right]\overline{\lambda}^2\overline{\mu}\overline{\theta}$$
$$=\left[\frac{q_D L^4}{cD_o}\right]\overline{q}C_{l_a}\overline{\theta} \tag{3.3.3b}$$

where the dynamic pressure, mass per unit area and vibration frequency are normalized by the divergence dynamic pressure q_D, average mass per area μ_o and fundamental natural frequency λ_o, respectively. The remaining non-dimensional quantities are defined as

$$\overline{D}_{ij}=\frac{D_{ij}}{D_o}\qquad \overline{M}_\Lambda=\frac{M_\Lambda}{M_{\Lambda_o}}\qquad \overline{q}=\frac{q}{q_D}\qquad \overline{\mu}=\frac{\mu}{\mu_o}\qquad \overline{\lambda}=\frac{\lambda}{\lambda_o}$$
$$\overline{w}=\frac{w}{h}\qquad \overline{\theta}=\frac{\partial\overline{w}}{\partial\overline{y}}=\frac{c}{h}\frac{\partial w}{\partial y}=\frac{c}{h}\theta$$
$$\overline{x}=\frac{x}{L}\qquad \overline{y}=\frac{y}{c} \tag{3.3.4}$$

where D_o is the reference bending stiffness and M_{Λ_o} is the reference strain actuated equivalent moment. Note that in contrast with usual practice, three length scales (span L, chord c and thickness h) are used in normalizing the equations so that the effects altering the lifting surface geometry can be assessed in a consistent manner. Eq. 3.3.3a shows that while aspect ratio is unimportant for the problem of simple spanwise bending, it is important for creating the twist needed for aeroelastic control through bending/twist coupling. The need to match aspect ratio is not a surprising result for the plate-like structures under examination. This result is also not constricting since aerodynamic considerations (for actual three-dimensional lifting surfaces) usually requires that aspect ratio to be matched regardless of the structural scaling. The equations also reveal another important non-dimensional geometric factor. The non-dimensional coefficient of the last term in Eq. 3.3.3a shows that the ability of strain actuators to deform a

structure depends on the slenderness ratio h/L. However the slenderness ratio is lumped with other terms so that the overall coefficient, rather than the slenderness ratio itself, is the parameter which must be matched.

The essential non-dimensional parameter governing strain actuation is found from Eq. 3.3.3a to be the actuator force stiffness ratio listed in Table 3.1. This parameter is new to the aeroelastic scaling problem and arises from the use of strain actuation. The force stiffness ratio is essentially the ratio of the equivalent moment produced by the strain actuators to the bending stiffness of the structure. Note that both structural elements and the actuators contribute to the total bending stiffness, while only the strain actuators contribute to the equivalent moment. By substituting the force stiffness ratio into Eq. 3.3.3b, alternate representations of this fundamental strain actuator aeroelastic control parameter can be identified. These parameters are also listed in Table 3.1. They include the force pressure ratio, a measure of the aerodynamic relative to the strain actuator forces, and force mass ratio, a comparison of the inertial and strain actuator forces. These non-dimensional parameters (valid for arbitrary geometries), along with those normal to aeroelasticity such as mass ratio μ and reduced frequency k, are the quantities which must be matched for scale model test results to be applied to actual lifting surfaces.

Further insight regarding the fundamental non-dimensional parameters can be found by utilizing the wing stiffness (Eq. 3.1.2) and strain actuator forcing (Eq. 3.1.3) associated with the box wing geometry displayed in Fig. 3.2 or 3.3 (assuming $h = 2Z_{ms} \cong 2Z_{ma}$). Substitution of these terms into the arbitrary geometry parameters yields the non-dimensional box wing geometry parameters listed in Table 3.1. The box wing geometry parameters emphasize the role of the slenderness ratio h/L (or thickness ratio h/c) in strain actuation. The slenderness ratio is fundamental to both simple beam bending and effecting aeroelastic control through bending/twist coupling. Notice how the thickness ratio determines the geometric susceptibility of aerodynamic forces to strain actuation as the slenderness ratio determined the effectiveness of strain actuated beam bending. These parameters also show the importance of the relative actuator to substructure stiffness ψ and density ψ_ρ ratios.

Additional Aeroelastic Scaling Law for Strain Actuated Structures	Non-dimensional Parameters for Arbitrary Geometry	Non-dimensional Parameters for Box Wing Geometry
Force Stiffness Ratio	$\frac{hD_o}{M_{\Lambda_o}L^2}$	$\frac{1}{2}(1+\psi)\left(\frac{h}{L}\right)^2$
Force Pressure Ratio	$\frac{q_D h L^2}{c M_{\Lambda_o}}$	$\frac{q_D L}{E_a t_a}\left(\frac{L}{c}\right)$
Force Mass Ratio	$\frac{\lambda_o^2 \mu_o h L^2}{M_{\Lambda_o}}$	$\frac{\lambda_o^2(1+\psi_\rho+\Delta_\rho)L^2}{E_a/\rho_a}$
Aspect Ratio	$\frac{L}{c}$	$\frac{L}{c}$
Relative Stiffness Ratio	–	$\psi = \frac{E_s t_s}{E_a t_a}$
Relative Density Ratio	–	$\psi_\rho = \frac{\rho_s t_s}{\rho_a t_a}$

Table 3.1. Additional strain actuated lifting surface scaling laws.

Note that in the equations derived, the out-of-plane displacements w are normalized by the plate thickness h in order to obtain a rational non-dimensionalization consistent with plate theory. However, other normalization schemes may be more appropriate depending on the non-dimensional quantities of interest. For example, in assessing quasi-static aeroelastic control authority, scaling the local angle of attack or twist θ is more important than scaling the out-of-plane deflections in terms of plate thickness. Therefore, the plate deflections should be normalized by the chord c rather than the thickness h. Scaling the plate twist w/c rather than deflections w/h introduces a factor of c/h, which when multiplied by the force stiffness ratio causes the box wing force stiffness ratio to scale like the slenderness ratio and aspect ratio (rather than the slenderness ratio squared). This explains why the optimal induced camber equation (3.1.7) scales like the thickness ratio (not squared) and the optimal induced twist equation (3.1.11) scales by the aspect ratio and thickness ratio, as shown in section 3.1.

In addition to geometric scaling, the box wing parameters reveal other important scaling considerations. The ratio of strain actuator force to aerodynamic stiffness (force pressure ratio) shows that greater strain actuator forces are required as the dynamic pressure increases. Larger strain actuator forces can be obtained by increasing the actuator thickness. Note that the need for increased control forces at higher dynamic pressures is a problem encountered by all actuators (including conventional articulated control surfaces) effecting aeroelastic control. The non-dimensional parameters also show that strain actuators made from the same material (defined by E_a/ρ_a) may be used for both scale models and actual lifting surfaces with box beam construction since the reduced frequency $k = \lambda b / U$ must be matched in aeroelastic testing. This can be seen more clearly by substituting the reduced frequency into the force mass ratio yielding

$$4k_o^2 \frac{U_o^2\left(1+\psi_\rho+\Delta_\rho\right)}{E_a/\rho_a}\left(\frac{L}{c}\right)^2 \qquad \text{where} \quad \Delta_\rho = \frac{\mu_o}{E_a t_a} \tag{3.3.5}$$

The reduced frequency and the aspect ratio must be matched so that the aerodynamics are scaled properly. Also the scale model velocity ratio difference should be accounted for by the added mass μ_o, as is the usual practice for sub-velocity sub-length scale model testing [Ducharme and Crawley, 1987]. Thus, the actuator properties are independent of other scale factors, and actuators used on scale model tests may be applied to full scale articles directly.

The force stiffness and force mass ratios have interesting implication for using strain actuators to control realistic aeroelastic structures, since the force created by strain actuators scales like length squared and the weight of the actuators scales like length cubed. However the amount of aeroelastic control effected is dependent on the work done on the structure by the strain actuators, which is the product of the force multiplied by the distance that the force is applied. Therefore the amount of control performed, which is a function of the energy or work imparted by the actuators, scales like length cubed and scales in exactly the same manner as the weight of the actuators. Thus, the control authority demonstrated by strain actuators on scale model lifting surfaces can be directly applied to the control of actual active wings.

Chapter 4. Test Articles

In the previous chapters simplified models showed that strain actuators could be successfully employed to effect aeroelastic control. As a result, test articles were built to experimentally demonstrate this aeroelastic control potential. This chapter describes the lifting surfaces used and the associated hardware needed for open and closed loop testing. The test articles were constructed at the Massachusetts Institute of Technology (MIT) Space Engineering Research Center (SERC) and are described in detail in Lazarus and Crawley [1989]. The test articles were designed as thin, low-aspect-ratio lifting surfaces so that both aeroelastic and transverse plate effects would be important, thereby serving as a testbed for developing and demonstrating plate-like strain actuated lifting surface aeroelastic modeling and control law design techniques.

4.1 Strain Actuated Test Article Construction

Fig. 4.1 shows a diagram of the strain actuated active lifting surface test articles. The test articles had a span x of 11.5 in (29.2 cm) and a chord y of 6.0 in (15 cm), which resulted in an equivalent full span aspect ratio of 3.83. The test articles had a thickness-to-chord ratio of 0.51 percent, and were fixed at the root by an immobile clamp for both the bench-top and wind tunnel experiments. Two model lifting surfaces were constructed, analyzed and tested. A 6061 aluminum bench-mark article was designed and tested as was a $[+30_2/0]_s$ bending/twist coupled AS4/3501-6 graphite/epoxy (G/E) plate which exhibited enhanced torsional control. The material properties of the lifting surface test articles are reported in Table 4.1. The aluminum plate thickness was 0.03125 in. (0.794 mm) and each ply of the G/E plate was 0.00528 in. (0.134 mm), resulting in a total G/E plate thickness of 0.03166 in. (0.804 mm). Due to the fiber migration associated with curing plates having a small numbers of plies, the G/E plate stiffness properties were adjusted (from the values in Table 4.1) by assuming that all graphite fibers were located in the middle 70 percent of the six ply composite plate.

The aluminum plate was later (after all other experiments were completed) modified to flutter within the wind tunnel operating range. The test article was modified by attaching a lead mass at the wing tip one semi-

chord behind the trailing edge. The mass weighed 285.5 g or 120.9 percent of the original aluminum test article weight (236.22 g) and was held in place by an 85.7 g aluminum brace, making the total modified-for-flutter aluminum test article mass equal to 157.1 percent of the nominal aluminum lifting surface. The added weight lowered the fundamental vibration frequency of the modified-for-flutter test article by 57.6 percent and lowered the flutter speed by 32.3 percent (see Chapter 5 for details).

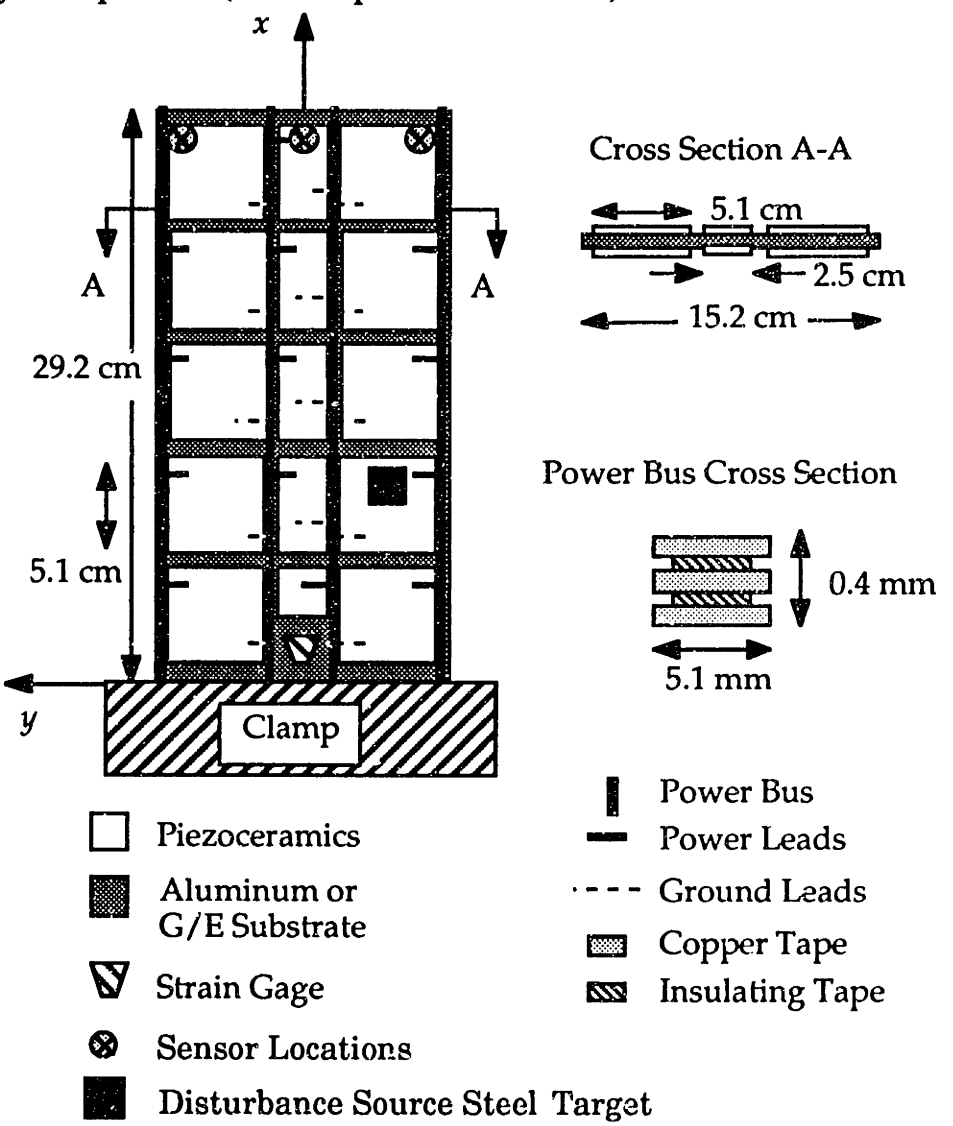

Figure 4.1. Model strain actuated active lifting surface test article.

The strain actuated lifting surfaces were designed as integrated controlled structures. The Piezoelectric Products Incorporated G-1195 piezoceramic actuators were intended to not only provide actuation, but also to make up a substantial portion of the structure itself. Each of the active

test articles had approximately 70 percent of each surface covered with the surface-bonded piezoceramic strain actuators. The 10 mil (0.254 mm) strain actuators accounted for 31.3 and 52.0 percent of the aluminum lifting surface volume and weight, and 30.1 and 62.3 percent of the graphite/epoxy lifting surface volume and weight, respectively. These piezoceramic actuators increased the spanwise bending stiffness of the aluminum and graphite epoxy plates by 201 and 437 percent, respectively, over the nominal substructure stiffness.

Voltage was provided to the actuators via four spanwise power busses. Each bus consisted of two layers of copper and three layers of insulating tape. Power bus grooves were machined in the lifting surfaces so that the upper surface of each bus was equal to that of the piezoceramic actuators. The 4 mil (0.102 mm) bus grooves ensured that each plate had a smooth surface, but decreased the bending stiffness in the grooved region by 41.2 percent for the aluminum plate, and 6.4 and 14.8 percent for the G/E plate in the spanwise and chordwise directions, respectively. The test articles were constructed so that the 30 piezoceramic wafers which were bonded to each wing were divided into twelve independent control groups for independent control of the first three modes (details of the control groups are provided in Lazarus and Crawley, 1989).

	Aluminum	G/E	Piezoceramic	Lead
E_L	70 GPa	142 GPa	60 GPa	–
E_T	70 GPa	9.81 GPa	60 GPa	–
ν_{LT}	0.3	0.418	0.3	–
G_{TL}	26.92 GPa	7.00 GPa	22.00 GPa	–
t_{ply}	0.794 mm	0.134 mm	0.254 mm	–
ρ	2700 kg/m^3	1500 kg/m^3	5400 kg/m^3	5400 kg/m^3

Table 4.1. Lifting surface test articles material and geometric properties.

The surface of each test article was covered with a thin layer of polyurethane in order to protect the wings from accidental damage and to provide a smooth aerodynamic surface for the wind tunnel tests. The total weight of the test articles, including the structure, piezoceramics, power buss,

leads and polyurethane, was measured to be 236.2 g and 196.6 g for the aluminum and G/E lifting surfaces, respectively.

4.2 Associated Hardware

In addition to the test articles, many other components were required to perform control experiments. These components, which included hardware such as sensors, a digital control processor, power amplifiers and disturbance sources, are described below. The motion of the test articles was measured by 3 non-contacting Keyence LB-70 laser displacement sensors. Each sensor had a half power (3 db gain reduction) bandwidth of 700 Hz, a range of 5.5 in (14 cm) and a resolution of 7.1×10^{-3} in (180 μm). The displacement sensors were used to measure the plate motion 0.5 in below the tip of each lifting surface in both the bench-top and wind tunnel configurations. One sensor measured the motion 0.5 in aft of the leading edge (y_1), another was used to measure the displacement at the mid-chord (y_2), and the third sensor detected the motion 0.5 in forward of the trailing edge (y_3). A. P. Circuit Corporation variable frequency filters were used to eliminate high frequency (above 1000 Hz) noise from each sensor signal. It is acknowledged that actual lifting surfaces are not able to take advantage of such displacement measurements. However, actual lifting surfaces do have ample space (not available on the small scale model lifting surfaces) for accelerometers, the output of which can be integrated to yield measurements equivalent to the displacement measurements made in this study.

All compensator designs were implemented by a Wind River Systems VX Works UNIX-compatible real time operating system running on a Heurikon HK68/V30 digital control computer. The Heurikon was linked to a Supercard array processor for increased controller speed. The control computer was capable of handling up to 16 sensor inputs (16 bit A/D's) and 8 control outputs (16 bit D/A's). Variable frequency four-pole anti-aliasing Bessel filters were utilized to eliminate unwanted alias signals.

Power was provided for the piezoceramic strain actuators by high-voltage low-impedance amplifiers constructed from Acopian 100PT3 voltage supplies and Apex PA08V operational amplifiers. Four 100 volt Acopian supplies were tied in series to provide a maximum of plus or minus 200 peek

Volts. This voltage was sufficient to supply an electric field just below the coercive field (24 Volts/mil) of the piezoceramic wafers. Twelve Apex operational amplifiers were used to provide independent amplification of each actuator group control signal.

4.3 Test Configuration and Disturbance Source

The strain actuated active lifting surfaces were tested in both bench-top and wind tunnel configurations. Most of the hardware, including the laser sensors, filters, control computer and amplifiers, was used in both sets of experiments. However, the disturbance sources used to excite the test articles in each set of experiments were not identical. Each disturbance had a different bandwidth, forcing level, and spatial distribution.

A non-contacting magnetic proximity probe was driven as an actuator to provide a disturbance source in the bench-top configuration. The magnetic field created by the proximity probe produced a disturbance force on a one inch square steel target attached to each test specimen. This disturbance force was applied at the quarter chord in order to create forces similar to those encountered during wind tunnel testing. The steel target was placed at approximately the quarter span because at this location the disturbance source was found to excite the test articles most effectively. The magnetic shaker was held at a distance of about 0.125 in. from the square target by a steel support bracket. The steel support bracket, shown in Fig 4.2, was also used to hold the laser sensors at a distance of 4.0 in. (10.2 cm) from the test articles.

The magnetic shaker created a localized force of sufficient magnitude to cause deflections of roughly 0.25 in. (6.35 mm) at the tip of the test articles. This forcing level combined with the accuracy of the laser sensors gives a rough estimate of the measurement error for the bench-top experiments. The estimated error was calculated to be 0.41 percent (see section 6.1). The magnetic probe was exited by a 500 Hz bandwidth, zero-mean, white noise signal generated by a Tektronix 2630 Fourier analyzer. The magnetic probe was able to generate forces of roughly the same magnitude over a wide range of frequencies. Thus, the forcing provided by the shaker had essentially no high frequency roll-off in the excitation bandwidth.

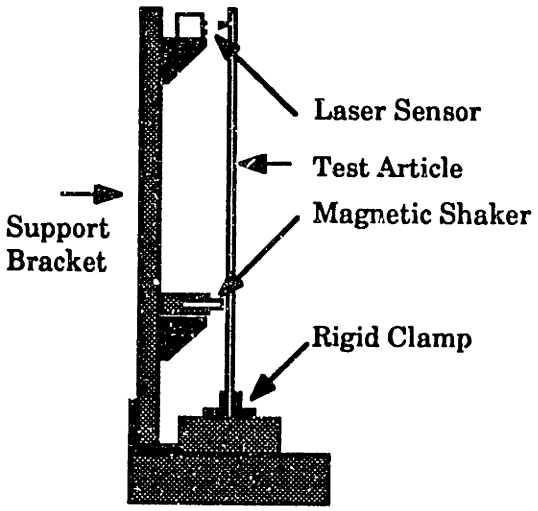

Figure 4.2. Side view of the steel support bracket used to hold the non-contacting magnetic shaker and laser proximity sensors.

The wind tunnel experiments were conducted in the MIT department of Aeronautics and Astronautics 1x1 foot laminar flow wind tunnel. A wind tunnel test section, shown in Fig. 4.3, was constructed to house the lifting surfaces, laser sensors, pitot tube and gust generator. The test section had a width of 8.0 in. (20.3 cm) and a height of 12.0 in. (30.5 cm), and the lifting surfaces were mounted vertically in the middle of the section. The flow area was reduced from the 1x1 foot tunnel section to the 8x12 in. test section using a minimum drag shape to ensure smooth flow. In this configuration, the laser sensors were located 4.0 in. (10.2 cm) from the test articles (as was the case for the bench-top experiments). This 4.0 in. stand-off distance gave a usable measurement range of plus or minus 1.5 in (3.81 cm) from the laser sensors which had a maximum range of 5.5 in. (14.0 cm). The lifting surfaces were mounted at a zero root angle of attack using a rigid cantilever support similar to that of the bench-top experiments. Any gaps between the cantilevered root of the test articles and the test section floor were closed with cellophane tape to ensure smooth air flow. Note that the bending/twist coupled G/E lifting surface was tested in a washin (bending causes an increased angle of attack) configuration.

The disturbance for the wind tunnel experiments was supplied by a gust generator, designed and constructed to provide about a 1 degree broad band angle of attack variation in the free stream flow. The gust generator,

depicted in Fig 4.3, was constructed of three gust vanes made from 0.0625 in. thick aluminum and a 0.75 in. aluminum push rod. The gust vanes, which had a chord of 4.0 in. and a span of 11.5 in., were placed in the wind tunnel test section 6.0 in. ahead (measure from the mid-chord of the lifting surfaces to the mid-chord of the gust vanes) of the lifting surfaces. The gust vanes were separated by 1.0 in. (perpendicular to the flow), with the middle vane aligned with the test articles. The 0.75 in. push rod, which was connected to the quarter chord of the vanes at the tip by 0.25 in. diameter aluminum rods, was driven by an Indiana General 48 V 3320D-79B D.C. motor. The D.C. motor produced a rotational speed roughly proportional to the input voltage. The position of the motor shaft Θ_m was measured using a voltage source and a variable resistance 120KΩ ten turn trim pot connected to the motor shaft.

A feedback control circuit was designed using classical techniques so that the gust generator frequency response was similar to that of a typical gust spectrum. The closed loop response of the gust generator, measured from voltage in V_{in} to motor shaft angle Θ_m, had a gain of ten from zero to 40 Hz and then rolled-off due to a double real pole. Note that because the open loop transfer function from V_{in} to Θ_m had a free integrator, this transfer function had a closed loop steady state error of zero. The gust generator was driven with a zero mean white noise signal generated by the Fourier analyzer. This input produced a gust amplitude of approximately one degree in the bandwidth of zero to 40 Hz. The excitation caused by the gust generator at the gust alleviation test velocity of 60 mph was found to be roughly three times that of the bench-top disturbance source or 0.75 in. (1.91 cm). Thus, the lifting surface response to the gust generator disturbance yielded a laser sensor measurement error of about 0.14 percent.

In addition to driving the bench-top magnetic shaker and the wind tunnel gust generator, the Fourier analyzer was also used to process the disturbance, sensor and control signals. The output of the Fourier analyzer was used to produce disturbance and control transfer functions and calculate the RMS response.

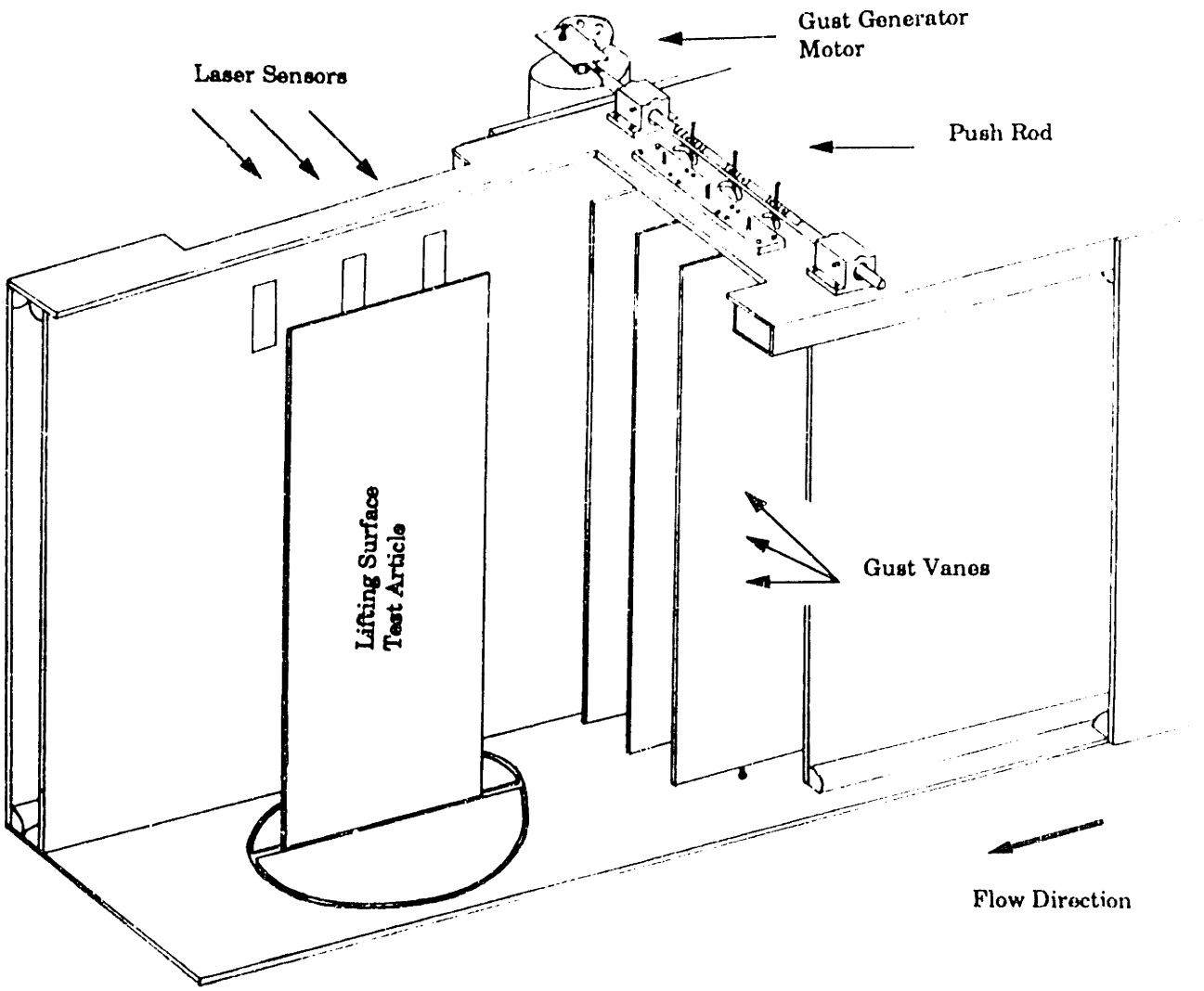

Figure 4.3. Wind tunnel test section with active lifting surface vertically mounted one semi-chord behind the gust generator vanes. The wall-mounted laser displacement sensors are also shown in the figure.

Chapter 5. Analytical Model

Building an aeroelastic model of sufficient accuracy for designing closed loop controllers requires considerable knowledge of structural dynamics, aerodynamics and linear system analysis. Fig. 5.1 shows the pieces of analysis needed and the logical flow of modeling tasks which lead to a high fidelity aeroelastic model. Each analysis piece contributes states, representing the dynamics of the physical phenomenon modeled, to the full order model in a form compatible with linear time-invariant system analysis. The full system includes models of the plant dynamics (structural dynamics and unsteady aerodynamics), actuator and sensor dynamics, disturbance source dynamics and any dynamics associated with electronic equipment such as amplifiers and filters. This chapter details the models used to describe the dynamics of the lifting surfaces, the assembly of the individual models into a coupled state space system, and the reduction of the model to a size useful for designing effective control laws.

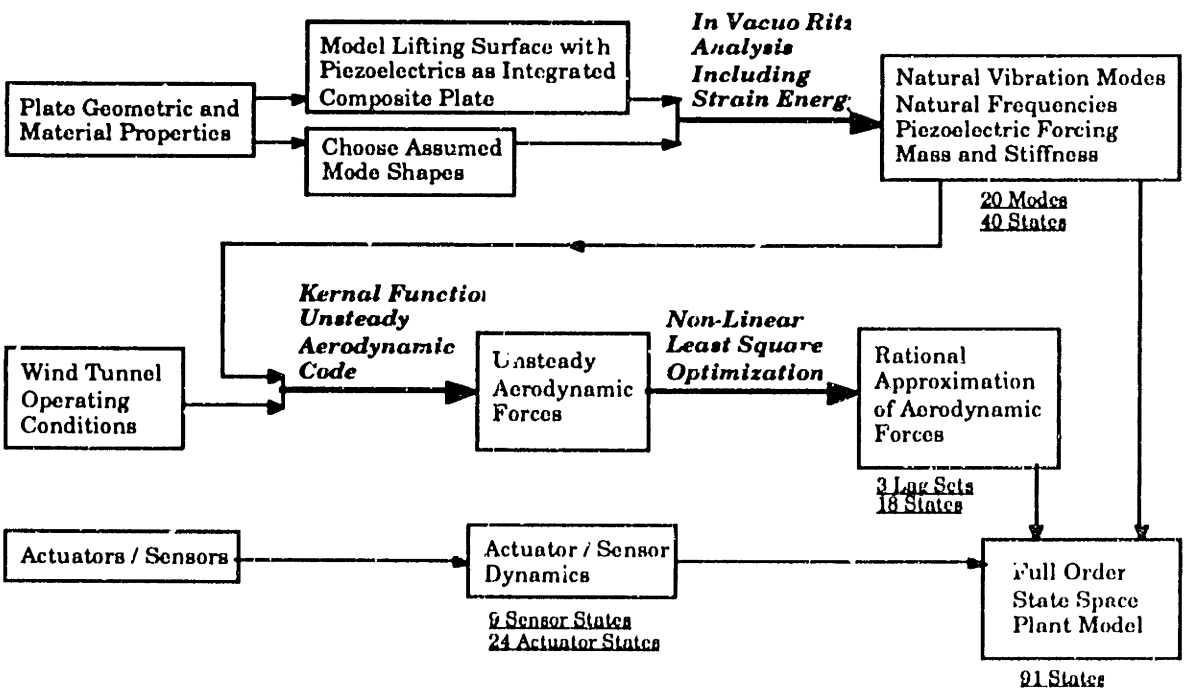

Figure 5.1. Aeroelastic modeling flow chart. Figure shows structural, aerodynamic and other component analytical models, and how the various pieces fit together to produce a full aeroelastic model.

5.1 Lifting Surface Structural Model

A detailed structural model is essential for implementing high-authority, large-bandwidth control systems. Accurate knowledge of the system poles and zeros is required in order to develop effective control schemes. To achieve such a high fidelity model, the active test articles with surface mounted strain actuators are modeled as integrated components of a composite structure. By modeling the substructure, piezoceramic actuators and epoxy layers as plies of a laminated plate, the appropriate strain energy relations can be derived using the usual Kirchoff plate assumptions [Lazarus and Crawley, 1989, Lee and Moon, 1989 and Wang and Rogers, 1991].

$$U = \frac{1}{2}\int_{A}\int \{\varepsilon^{o T} \quad \kappa^{T}\}\begin{bmatrix} \mathbf{A} & \mathbf{B} \\ \mathbf{B} & \mathbf{D} \end{bmatrix}\begin{Bmatrix} \varepsilon^{o} \\ \kappa \end{Bmatrix} d\,(A) - \int_{A}\int [\mathbf{N}_{A}\ \mathbf{M}_{A}]\begin{Bmatrix} \varepsilon^{o} \\ \kappa \end{Bmatrix} d\,(A) \tag{5.1.1}$$

Rayleigh-Ritz Assumed Mode Model

The Rayleigh-Ritz assumed mode method [Meirovitch, 1967] is used to formulate the lifting surface equations of motion from the strain energy relations. Ritz models have been shown to be superior at predicting the natural frequencies of plate-like structures to FEM models for a particular model order [Meirovitch and Kwak, 1990]. Also, it has been observed, through structural modeling experience, that Ritz models are better suited for correctly identifying system transmission zeros and individual actuator/sensor transfer function zeros. Although the Ritz method is a powerful analytical technique, obtaining accurate results requires that a well chosen set of assumed modes are used. The assumed modes are selected based on the structural configuration, the natural vibration modes of similar but less complex plate structures, experimentally observed modes shapes, and engineering judgment.

Twenty assumed shape functions are utilized in the Rayleigh-Ritz structural analysis of the strain actuated lifting surfaces. The spanwise x and chordwise y displacements of the assumed modes are listed in Table 5.1. The twenty modes include five spanwise beam bending (B), four spanwise torsion (T), two chordwise bending (C) and four extensional (E), as well as two "static" and three "segmented" modes. The spanwise bending modes, which

have an assumed constant chordwise distribution, are found from the exact solution of a cantilever-free beam [Blevins, 1984]. The spanwise torsional modes are calculated by performing a Torsion Partial Ritz analysis (assumed linear chordwise distribution), in order to include root warping stiffness effects [Crawley and Dugundji, 1980]. The chordwise bending modes are the exact solution of a free-free beam, where the spanwise deflection distribution is found from a dynamic Camber Partial Ritz analysis (assumed quadratic minus a constant distribution).

Mode	Mode Shape ψ_i	Spanwise x Distribution	Chordwise y Distribution
1-5	Bending (B)	Exact Cantilever Beam	Constant
6-9	Torsion (T)	Torsion Partial Ritz (Homogeneous Solution)	Linear
10-11	Chordwise (C)	Camber Partial Ritz (Homogeneous Solution)	Exact Free-Free Beam
12	Static x	Quadratic	Constant
13	Static y	Camber Partial Ritz (Particular Solution)	Quadratic minus constant
14-15	Segmented x	Curvature in non-piezoceramic areas only	Constant
16	Segmented y	Camber Partial Ritz (Particular Solution)	Curvature in non-piezoceramic areas only
17-18	Spanwise (E)	Sin(x), Linear	Constant
19-20	Chordwise (E)	Constant	Cos(y), Linear

Table 5.1. Assumed mode shapes included in the 20 mode Ritz analysis.

In addition to the usual dynamic mode shapes, modes are assumed which are not associated with the solution of any eigenvalue problem. A quadratic spanwise "static" and a quadratic chordwise "static" assumed mode are included to model the strain energy associated with a constant distributed bending moment. Also, two "segmented" spanwise modes and one "segmented" chordwise mode are assumed in order to correctly model the strain energy stored in the aluminum or G/E test article substructure at the relatively soft locations in the gaps between the piezoceramics. "Segmented" assumed modes have non-zero curvature in areas which do not contain piezoceramics and zero curvature in areas which do. One spanwise "segmented" mode had non-zero curvature in all the spanwise gaps and the other "segmented" mode had non-zero curvature only in the gap nearest the

root. The spanwise x distributions of the chordwise "static" and "segmented" modes are calculated from a static Chamber Partial Ritz analysis (assumed quadratic chordwise distribution) similar to that used to calculated the spanwise distribution of the torsional and dynamic chordwise bending modes. Inclusion of the "static" and "segmented" modes, as well as performing the Partial Ritz analysis, is essential for correctly predicting the system poles, transmission zeros and steady state transfer function magnitudes. Finally, two spanwise and two chordwise in-plane modes are also included to introduce the added flexibility of allowing for extensional actuation. Note that the assumed mode shapes which are dependent on the plate structural stiffness (modes 6-9, 13, and 16) are calculated using uniform averaged properties. The stiffness properties are averaged by weighting the stiffness of each section of the plate (substructure with piezoceramics, nominal substructure and substructure with power bus grooves) by the area of the section relative to the total plate area. Further Ritz analysis details, including full mathematical mode shape descriptions and a discussion of the Partial Ritz analyses, can be found in Appendix 5.A.

The Rayleigh-Ritz analysis method combines the plate strain energy relations and the assumed modes to calculate the plate equations of motion. To facilitate these calculations, the strain actuated lifting surface is divided into 91 sections which include grooved and non-grooved substructure, piezoceramic wafer, and additional mass (epoxy and power bus component) sections. The assumed mode shapes are integrated over each of the 91 segments, using isometric elements and a 32 point Gaussian integration procedure. This analysis yields the modal mass $\mathbf{m}$, stiffness $\mathbf{k}$, piezoelectric $\mathbf{f}_A$ and disturbance $\mathbf{f}_d$ forcing matrices

$$\mathbf{m}\ddot{\mathbf{q}} + \mathbf{k}\mathbf{q} = \mathbf{f}_A(t) + \mathbf{f}_d(t) + \mathbf{f}_A(t)$$

$$\text{where} \begin{bmatrix} \mathbf{u} \\ \mathbf{v} \\ \mathbf{w} \end{bmatrix} = \psi\mathbf{q}$$

$$\text{and } \psi = \begin{bmatrix} 0 & \cdots & 0 & \psi_{17} & \psi_{18} & 0 & 0 \\ 0 & \cdots & 0 & 0 & 0 & \psi_{19} & \psi_{20} \\ \psi_1 & \cdots & \psi_{16} & 0 & 0 & 0 & 0 \end{bmatrix} \qquad (5.1.2)$$

where **u**, **v** and **w** are the in-plane longitudinal and transverse and out-of-plane displacements, respectively. The generalized displacements **q**, in Eq. 5.1.2, are related to the in- and out-of- plane displacement through the assumed mode shapes ψ_i, which are functions of both the spanwise x and chordwise y coordinates. Note that the aerodynamic forcing matrix $\mathbf{f}_A(t)$, which is found using unsteady kernel function aerodynamics and a rational approximation, is discussed in section 5.2.

Verification of Structural Model

The experimentally measured bench-top and analytically predicted pole frequencies of the test articles are listed in Table 5.2. The Ritz predictions were within 5 and 9 percent of the experimentally measured values in the desired control bandwidth (about 200 Hz) for the aluminum and G/E plates, respectively. The aluminum test article Ritz predictions had a mean percent error of 2.6 with a variance in the percent error of 6.2, and the G/E test article predictions had a mean error of 4.9 with a variance of 13.8 in the control bandwidth. Note that the analysis method had the greatest difficulty in predicting the aluminum test article chordwise bending natural frequency (1C), due to sensitivity of this plate to the change in stiffness caused by the power bus grooves.

		Aluminum Plate			G/E Plate		
Mode	Shape	Exp. (Hz)	Ritz (Hz)	Error	Exp. (Hz)	Ritz (Hz)	Error
1	1B	7.44	7.79	+4.7%	6.88	7.44	+8.1%
2	1T	36.6	36.0	-1.4%	35.3	35.3	+0.0%
3	2B	49.5	50.4	+1.8%	47.8	49.0	+2.5%
4	2T	117	122	+3.9%	114	124	+8.8%
5	3B/1C	143	149	+4.0%	138	145	+5.1%
6	1C/3B	204	185	-9.3%	166	161	-3.0%
7	3T	223	235	+5.4%	215	242	+12.4%
8	4B	283	298	+5.3%	282	306	+8.4%
9	4T	370	390	+5.4%	353	405	+14.6%
10	5B	–	498	–	–	–	–

Table 5.2. Experimentally measured and analytically predicted test article natural vibration frequencies and dominant mode shapes.

In addition to the relatively small error in the predicted and measured natural frequencies, the Ritz analysis was also able to accurately compute the modal residues such that the static response was correctly predicted and the input/output transfer functions omitted no zeros and correctly ordered the poles and zeros. For example, the predicted frequency of the first two zeros of the disturbance to the leading edge sensor (y_1/**d**) transfer function shown in Chapter 7 (Fig. 7.1) were predicted within 7 and 5 percent of the bench-top experimental values, respectively. This accuracy was found to be typical of the results obtained (compare the open loop analytical and experimental singular value plots in section 5.5 and the disturbance to sensor transfer functions in Figs. 7.1, 7.2, 8.1 and 8.2) and sufficient for designing high-authority control laws.

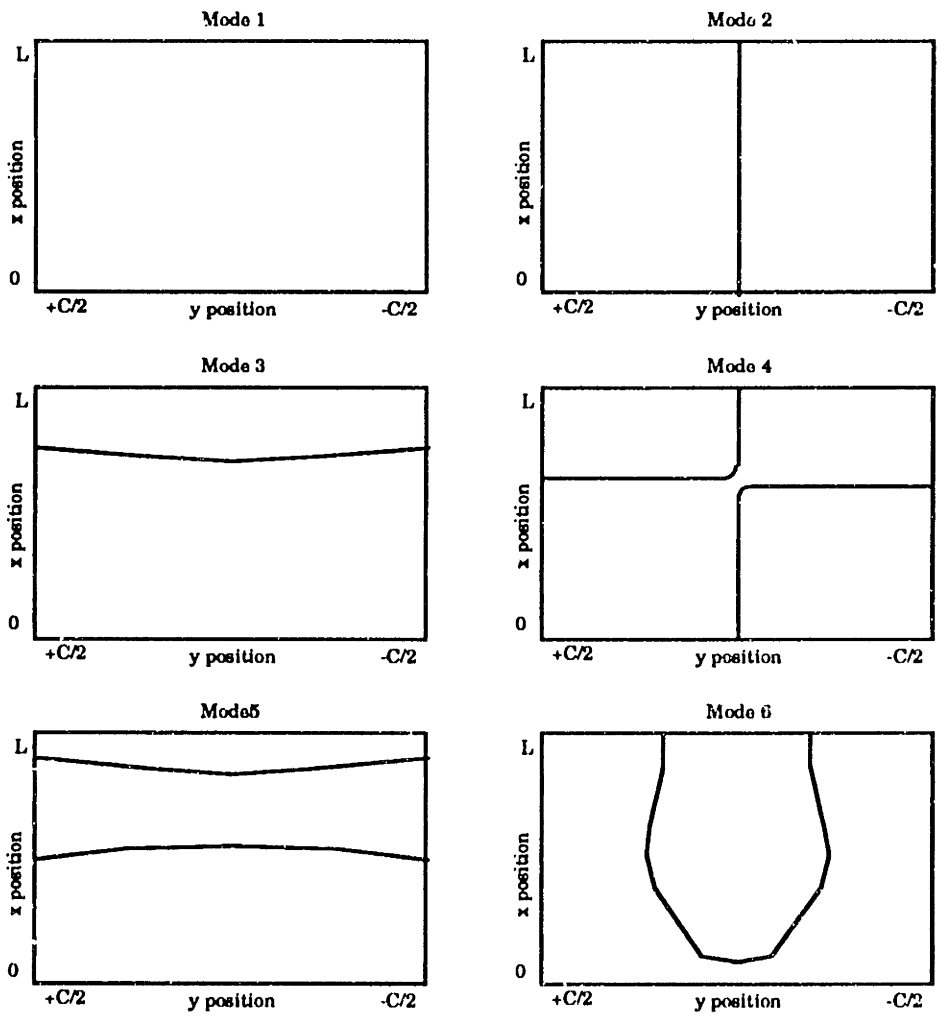

Figure 5.2. Nodal contour plots of the first six aluminum plate vibration modes on the bench-top. Aspect ratio not to scale.

In general, the Ritz model predicted the poles of the lifting surface with the aluminum substructure with greater accuracy than the G/E substructure because of difficulties in obtaining accurate estimates of the stiffness properties of thin laminated G/E structures. The anisotropic stiffness properties of the G/E substructure caused both the natural vibration mode shapes and dominant mode order to differ from that of the aluminum plate. This can clearly be seen in the nodal contour plots show in Figs. 5.2 and 5.3 for the aluminum and G/E lifting surfaces. The analytically generated plots show how stiffness cross coupling in the G/E plate causes the node lines of the torsionally dominated modes to be skewed from those of the aluminum plate. Also notice that the order of the third bending (3B) and first chordwise (1C) (*i.e.*, 5th and 6th) modes are transposed for the two plates.

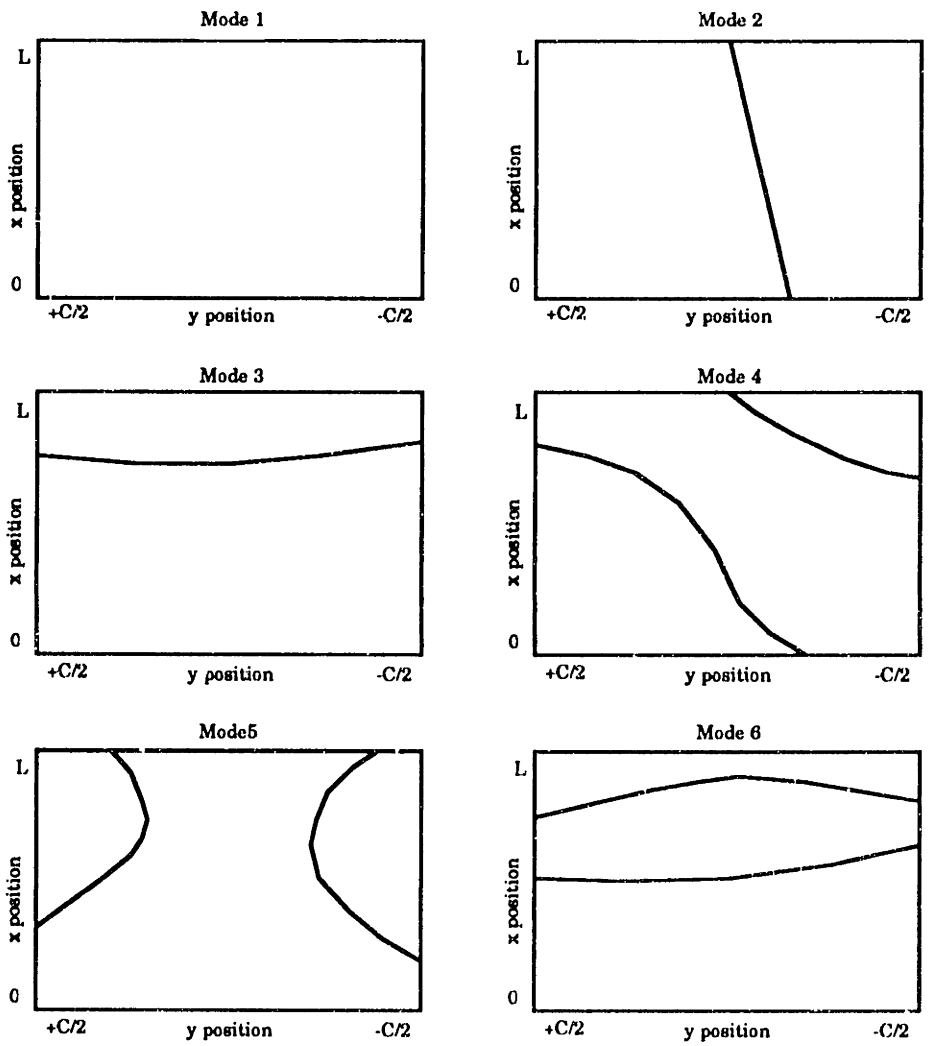

Figure 5.3. Nodal contour plots of the first six G/E plate vibration modes on the bench-top. Aspect ratio not to scale

The effect of different stiffness properties on the mode shapes is further illustrated by the three dimensional mode shape plots shown in Fig. 5.4. In this figure, the fifth natural mode is plotted for the aluminum and G/E plate. Observe that the aluminum plate mode is dominated by spanwise bending while the largest component of the G/E mode is chordwise bending. In addition, the "segmented" nature of the G/E plate mode shows the importance of including such an assumed mode in the analysis. Additional three-dimensional mode shape plots can be found in Appendix 5.B.

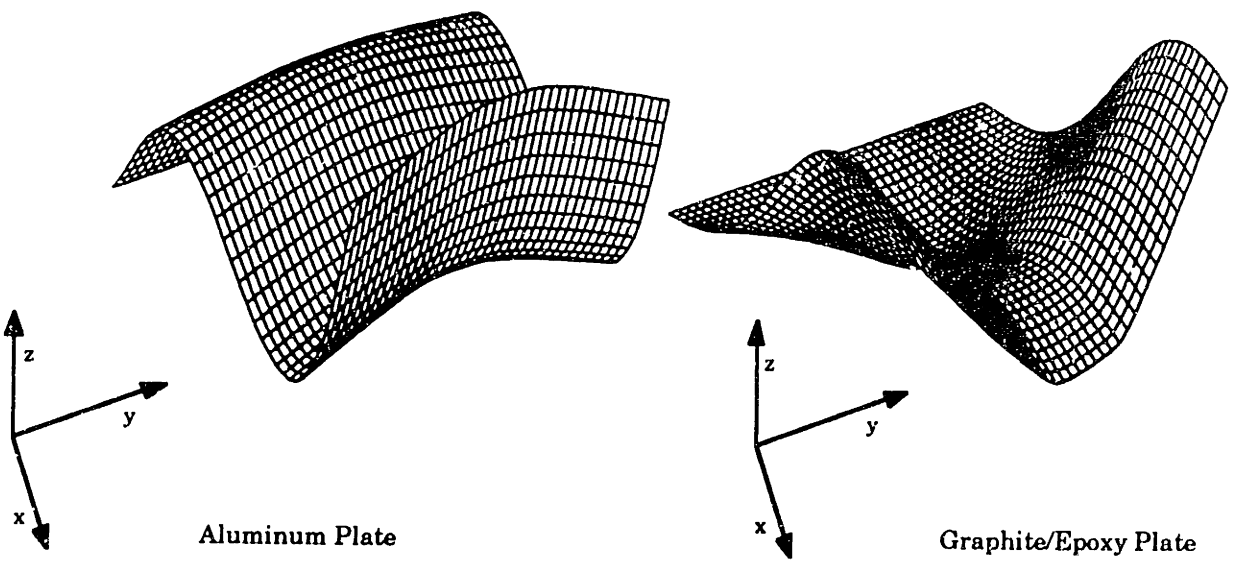

Figure 5.4. Three dimensional plot of the fifth natural vibration mode shape for the aluminum and the graphite/epoxy plates.

The model was further refined by updating the damping ratio ζ_r (estimated based on the half-power bandwidth technique) and natural frequencies ω_r using experimental frequency response data. Incorporation of the experimental data into the analytic model was facilitated by mapping ($\mathbf{q} = \Phi\eta$) the system of Eq. 5.1.2 to modal coordinates using the mass normalized eigenvectors Φ of the Ritz model

$$\mathbf{M}\ddot{\eta} + \mathbf{D}\dot{\eta} + \mathbf{K}\eta = \mathbf{F}_A(t) + \mathbf{F}_d(t) + \mathbf{F}_A(t)$$

$$\text{where} \quad \begin{bmatrix} \mathbf{u} \\ \mathbf{v} \\ \mathbf{w} \end{bmatrix} = \psi\Phi\eta \qquad (5.1.3)$$

$$\mathbf{M} = \Phi^T \mathbf{m} \Phi = \begin{bmatrix} \ddots & & \\ & m_r & \\ & & \ddots \end{bmatrix} = \mathbf{I} \qquad \mathbf{K} = \Phi^T \mathbf{k} \Phi = \begin{bmatrix} \ddots & & \\ & \omega_r^2 & \\ & & \ddots \end{bmatrix}$$

and

$$\mathbf{D} \equiv \begin{bmatrix} \ddots & & \\ & 2\zeta_r \omega_r & \\ & & \ddots \end{bmatrix} \qquad \mathbf{F} = \Phi^T \mathbf{f}$$

The structural system can also be expressed in the Laplace domain as

$$\left[\mathbf{M}s^2 + \mathbf{D}s + \mathbf{K}\right]\eta(s) = \mathbf{F}_A(s) + \mathbf{F}_d(s) + \mathbf{F}_A(s) \tag{5.1.4}$$

Including the experimentally determined damping estimates in the model proved extremely important for compensator design since this quantity directly affects the dynamic amplification of each mode, and therefore the plant/compensator loop gain and degree of notching required by the compensator in the roll-off region. In contrast, it was found that controllers designed from models with the experimentally updated stiffness matrices (adjusted using the measured frequencies) achieved no better performance than those designed from the analytically predicted Ritz stiffness.

5.2 Lifting Surface Aerodynamic Model.

Calculating the unsteady forces acting on a lifting surface in a form compatible with modern linear time-invariant dynamic analysis and control law development routines requires a two step process. First, the unsteady aerodynamic forces $\mathbf{F}_A(k,M)$ due to wing motion and gust flow variation are found from three dimensional compressible linear theory using either a doublet lattice [Albano and Rodden, 1969] or kernel function [Watkins, Woolston and Cunningham, 1959] method. The unsteady forces, which are complex functions of reduced frequency $k = wb/U_\infty$ and Mach number $M = U_\infty/a_o$, are evaluated at several distinct reduced frequencies for each flight condition (air speed and altitude). Second, the complex unsteady forcing matrices are fit with a rational function approximation in the (reduced) frequency domain. Such a fit normally includes mass-, damping- and stiffness-like terms plus lag and gust forcing matrices. A variety of techniques have been developed to obtain accurate fits including linear and non-linear least squares [Tiffany and Adams, 1988; and Eversman and

Tewari, 1991] and minimum state [Karpel and Hoadley, 1991] methods. Because the unsteady forces are functions of reduced frequency and Mach number, a rational approximation must be found, in general, for each flight condition. However, for low Mach number fixed altitude wind tunnel tests, the unsteady aerodynamics can be accurately described as a function of only reduced frequency $\mathbf{F}_A(k)$.

Unsteady Aerodynamic Forces

The aerodynamic forces $\mathbf{F}_A,(k)$, which are comprised of forces generated by the lifting surface motion itself $\mathbf{F}_{A\eta}(k)$ and unsteadiness in the flow $\mathbf{F}_{Ag}(k)$, are included in the modal equations of motion (Eq. 5.1.4) by pre multiplying the aerodynamic forces by the transpose of the mass normalized *in-vacuo* eigenvector matrix Φ.

$$\Phi^T\mathbf{F}_A(k)=\Phi^T\mathbf{F}_{A\eta}(k)+\Phi^T\mathbf{F}_{Ag}(k)=q\mathbf{Q}_\eta(k)\eta+q\mathbf{Q}_g(k)g \tag{5.2.1}$$

The elements of the generalized aerodynamic force matrix $\mathbf{Q}_\eta(k)$ are calculated by integrating over the lifting surface the product of the i^{th} deflection shape times the pressure distribution Cp due to the downwash δ associated with the j^{th} deflection shape.

$$\mathbf{Q}_{\eta_{ij}}(k)=\iint_{\text{wing}} h_i(x,y)\Delta Cp_{\delta_j}(x,y)dxdy \tag{5.2.2}$$

Likewise, the generalized gust force vector $\mathbf{Q}_g(k)$ is found by integrating over the lifting surface the product of the i^{th} deflection shape times the pressure distribution Cp due to the downwash δ_g associated with a sinusoidal gust

$$\mathbf{Q}_{g_i}(k)=\iint_{\text{wing}} h_i(x,y)\Delta Cp_{\delta_g}(x,y)dxdy \tag{5.2.3}$$

The gust profile is assumed to have the form

$$\frac{u_g}{u_{FS}}\left[\cos\left(\frac{x\omega}{u_\infty}\right)-i\sin\left(\frac{x\omega}{u_\infty}\right)\right] \tag{5.2.4}$$

where the gust velocity u_g is normalized by the free stream velocity $u_{FS} = u_g+u_\infty$ so that the leading constant is the gust velocity ratio.

Since modal forces are desired, the deflection shapes used are the natural mode shapes of the *in-vacuo* system **h**, which are found by multiplying the transpose of the mass normalized *in-vacuo* eigenvector matrix Φ by the matrix of assumed mode shapes ψ.

$$\mathbf{h}(x,y) = \Phi^T \left[\psi(x_1,y_1) \quad \psi(x_2,y_2) \quad \cdots \right] \tag{5.2.5}$$

The natural mode shape matrix **h** has dimensions of elastic modes by physical stations on the lifting surface at which the deflections are measured. Evaluating the aerodynamic forces directly in modal coordinates has advantages over evaluating the forces in assumed mode generalized coordinates and then transforming to modal space. First, fewer natural modes are needed because only the aerodynamics associated with the important natural vibration shapes need be known, rather than the aerodynamics associated with all the assumed modes which combine to form the natural modes. Second, it is less difficult to fit the aerodynamics with a rational approximation near the reduced frequency of a natural mode, rather than fit the aerodynamics in the reduced frequency regions associated with the assumed modes combining to form a natural mode. Further, the in-air aeroelastic frequencies are usually in the vicinity of the *in-vacuo* elastic frequencies, but are not necessarily near any frequencies of the assumed modes which contribute to a particular natural frequency. Thus, the aerodynamic forces are found using the natural *in-vacuo* elastic mode shapes, and are only calculated for the subset of natural modes which contribute significantly to the aerodynamics (*i. e.*, result in significant forces).

In this study, the modal aerodynamic $\mathbf{Q}_\eta(k)$ and gust force $\mathbf{Q}_g(k)$ matrices are calculated using the kernel function unsteady aerodynamics code UNSAER [Cunningham, 1971]. The out-of-plane deflections of the natural elastic modes are evaluated at seven chordwise and fourteen spanwise physical locations on the lifting surface. These deflections are input to UNSAER along with the lifting surface geometry and the reduced frequencies at which the aerodynamic forces are to be calculated. The unsteady kernel function code calculates the modal deflections and corresponding slopes over the entire lifting surface using the supplied deflections and internal interpolation functions. The downwash and pressure

is evaluated at five chordwise and six spanwise control stations with the aid of spanwise and chordwise assumed loading distributions. The loading distributions are chosen (from a variety of user controlled options) to be elliptic along the span and the distribution associated with the two-dimensional symmetric thin airfoil problem along the chord [Kuethe and Chow, 1976]. Interpolation functions are once again used to calculate the pressure distribution over the lifting surface. The product of the pressure distribution and modal deflection is then integrated over the wing to yield the generalized modal forces. Note that the generalized aerodynamic force matrix $\mathbf{Q}_\eta(k)$ is square and has dimensions of fitted natural modes, while the gust force matrix $\mathbf{Q}_g(k)$ has dimensions of fitted natural modes by gust disturbance modes.

Aerodynamic forces were calculated for the first six natural elastic mode shapes and the gust profile of Eq. 5.2.4. Only the first six natural modes were used in determining the aerodynamic forces for the active lifting surface test articles because it was found that the deflections associated with higher modes did not generate any significant aerodynamic forces. The modal aerodynamic forces were evaluated for all airspeeds at which experiments were performed and at 10 reduced frequencies (k = 0.01, 0.05, 0.1, 0.5, 1.0, 2.0, 3.0, 4.0, 5.0 and 6.0). In all cases the density was assumed to be the standard sea level flight value of 1.225 kg/m^3. The modal forces were calculated at several values of reduced frequency k near zero so that the rational approximation (described below) of the unsteady aerodynamic forces asymptotically approached the steady state solution as the reduced frequency decreased to zero. The remaining values were chosen to be evenly distributed over the wide range of reduced frequencies associated with the first six vibration modes in the wind tunnel (up to 100 mph) operating range.

Rational Approximation

The unsteady kernel function code provides the complex modal aerodynamic forces acting on the lifting surface as a function of reduced frequency. These forces can be combined with the *in-vacuo* modal mass, damping and stiffness matrices in order to calculate the system stability, natural frequencies and dynamic response. However, with the aerodynamic forces left as complex functions of reduced frequency, the dynamics of the

system can only be determined using either the physical interpretation lacking *V-g* [Bisplinghoff, Ashley and Halfman, 1957] or the time consuming iterative *p-k* [Hassig, 1971] method. Further, modern control law synthesis techniques cannot be utilized with the complex aerodynamic forcing matrices known only at discrete reduced frequency. Therefore, it is essential that the unsteady aerodynamic forces, which are transcendental functions in the Laplace domain, are fit with rational approximations so that efficient linear time-invariant system algorithms (*i.e.*, Matlab and MatrixX) may be utilized.

The unsteady forces are approximated with continuous functions by equating the complex forcing matrices with partial fraction frequency domain expansions, which are quadratic in reduced frequency k and have n_l lag terms

$$\begin{aligned}\mathbf{F}_A(k) &= q\left[\mathbf{Q}_\eta(k)\right]\eta + q\left[\mathbf{Q}_g(k)\right]g \\ &= q\left[(\mathbf{A}_0)_\eta + (\mathbf{A}_1)_\eta k + (\mathbf{A}_2)_\eta k^2 + \sum_{l=1}^{n_l}(\mathbf{A}_{2+l})_\eta \frac{k}{k+R_l}\right]\eta \\ &+ q\left[(\mathbf{A}_0)_g + (\mathbf{A}_1)_g k + (\mathbf{A}_2)_g k^2 + \sum_{l=1}^{n_l}(\mathbf{A}_{2+l})_g \frac{k}{k+R_l}\right]g \end{aligned} \quad (5.2.6)$$

The coefficient matrices $\mathbf{A}_0$, $\mathbf{A}_1$, $\mathbf{A}_2$ and $\mathbf{A}_{2+l}$ are solved for using a non-linear least squares technique, where the problem becomes non-linear when the lag poles R_l are free parameters. Note that each coefficient matrix has dimensions of the matrix to which it was fit (*i.e.*, the dimensions of $(\mathbf{A}_i)_\eta$ = equals that of $\mathbf{Q}_\eta$ and the dimensions of $(\mathbf{A}_i)_g$ = equals that of $\mathbf{Q}_g$).

In this study, the non-linear least squares routine SPLFIT [Tiffany and Adams, 1988] was utilized to generate the rational approximation matrix coefficients and lag poles. The first coefficient matrix $\mathbf{A}_0$ was fixed such that the approximation matched the steady state solution exactly for k equal to zero. The remaining coefficient matrices were solved for by SPLFIT. It was found that the accuracy of the approximation improved as the number of lag terms n_l increased from zero. The accuracy of the fit, measured by the least squares error between the rational approximation and the aerodynamic forces calculated at discrete reduced frequencies, improved with the addition of a first, second and third lag term, but no measurable improvement was found with the addition of a fourth term. Thus, three lag terms were used in fitting

the lifting surface test article unsteady aerodynamics. The value of each lag pole was determined by an optimization procedure within SPLFIT which minimized the total error over all elements of the matrix coefficients.

Verification of Unsteady Aerodynamics

The unsteady aerodynamics calculated by UNSAER were verified by comparing the aerodynamic forces generated using two-dimensional plunge and pitch modes with the results obtained by Theodorsen [1935]. The effects of aspect ratio and Mach number were also verified by comparison with a finite span correction and a Prandtl-Glauert transformation, respectively. All comparisons made were found to be favorable. However, the real check on the accuracy of the unsteady aerodynamic forces will be made by examining the theoretical and experimental loop transfer functions (section 5.5), and ultimately by performing closed loop aeroelastic control experiments (Chapters 7 and 8). On the other hand, the ability of the rational function fit to approximate the unsteady aerodynamics can be verified immediately. Figs. 5.5 and 5.6 show the generalized (modal) aerodynamic forces and their corresponding rational function approximations for the G/E lifting surface at 60 mph. Plots are displayed of the first (1^{st} bending) and second (1^{st} torsion) modal forces generated by deflecting the lifting surface in the first six modes. Both the real and imaginary parts of the generalized forces and rational function approximations are plotted versus reduced frequency. The accurate approximations of the generalized forces plotted were found to be typical of those obtained for the other G/E lifting surface modes as well as the modes of the other test articles.

Figs. 5.5 and 5.6 show that the largest generalized forces acting on the first and second modes, respectively, resulted from the motion of these low frequency modes themselves. However, some of the forces produced by the higher frequency modes were also found to be quite large and contribute significantly to the aeroelastic behavior of the lifting surfaces. The figures also show that the magnitude (and often the sign) of the generalized forces change considerably with frequency. Despite this large variation in forces the rational approximations fit the tabular data remarkably well. The total least squares error over all generalized forces was calculated to be 0.015 and 0.005 for the aluminum and G/E lifting surfaces at 60 mph and 0.038 for the

modified-for-flutter lifting surface at 90 mph, respectively. Finally, note that all of the rational approximations asymptote to the steady lift solution (k=0), and that all of the steady generalized forces have imaginary parts equal to zero.

With the aerodynamic forces computed and approximated by rational functions, the next step required to describe the (reduced) frequency dependent unsteady aerodynamic forces in a form compatible with linear time-invariant system analysis methods is to express the approximate forcing functions (Eq. 5.2.6) in terms of the Laplace variable s. The transformation to the Laplace domain is accomplished by letting $s = iw$ ($k = wb/U$).

$$\begin{aligned}\mathbf{F}_A(s) &= q\left[\mathbf{Q}_\eta(s)\right]\eta + q\left[\mathbf{Q}_g(s)\right]g \\ &= q\left[\left(\overline{\mathbf{A}}_0\right)_\eta + \left(\overline{\mathbf{A}}_1\right)_\eta s + \left(\overline{\mathbf{A}}_2\right)_\eta s^2 + \sum_{l=1}^{n_l}\left(\overline{\mathbf{A}}_{2+l}\right)_\eta \frac{s}{s+\overline{R}_l}\right]\eta \\ &+ q\left[\left(\overline{\mathbf{A}}_0\right)_g + \left(\overline{\mathbf{A}}_1\right)_g s + \left(\overline{\mathbf{A}}_2\right)_g s^2 + \sum_{l=1}^{n_l}\left(\overline{\mathbf{A}}_{2+l}\right)_g \frac{s}{s+\overline{R}_l}\right]g\end{aligned}$$

where

$$\begin{aligned}\overline{\mathbf{A}}_0 &= \mathbf{A}_0 & \overline{\mathbf{A}}_2 &= \mathbf{A}_2\left(\frac{b}{U_\infty}\right)^2 \\ \overline{\mathbf{A}}_1 &= \mathbf{A}_1\frac{b}{U_\infty} & \overline{\mathbf{A}}_{2+l} &= \mathbf{A}_{2+l} \\ \overline{R}_l &= R_l\frac{U_\infty}{b}\end{aligned} \qquad (5.2.7)$$

This Laplace domain transformation is technically valid only for simple harmonic motion (assumed for calculating the aerodynamic forces). However, the concept of analytic continuation is commonly used to justify extending rational functions into the entire Laplace domain in order to describe growing and decaying motion [Tiffany and Adams, 1988]. Unfortunately, what is really being done is best described as approximate analytic continuation since the function being continued in the Laplace domain is itself a continuous approximation of discrete values. Despite such drawbacks, the method described above has been found to model the unsteady aerodynamic forces acting on lightly damped lifting surfaces quite well. This is because the poles of these structures are generally near the imaginary axis, and for problems

such as gust alleviation and flutter suppression the dominant response is that of simple harmonic vibratory motion and the poles which are most significant are generally near the imaginary axis.

Of course the real motivation behind using the method described above is to manipulate the unsteady aerodynamic forces into a form which can be easily incorporated into a state space model of the aeroelastic system. Note that the Laplace domain rational function approximation of the unsteady aerodynamic forces described by Eq. 5.2.7 is in precisely the desired form. Substitution of these Laplace domain aerodynamic forces into the 2nd order modal equations of motion (Eq. 5.1.4) yields

$$\left[\overline{\mathbf{M}}s^2+\overline{\mathbf{D}}s+\overline{\mathbf{K}}\right]\eta = q\left[\sum_{l=1}^{n_l}\left(\overline{\mathbf{A}}_{l+2}\right)_\eta \frac{s}{s+\overline{R}_l}\eta+\sum_{l=1}^{n_l}\left(\overline{\mathbf{A}}_{l+2}\right)_g \frac{s}{s+\overline{R}_l}g\right]$$
$$+q\left[\left(\overline{\mathbf{A}}_2\right)_g s^2+\left(\overline{\mathbf{A}}_1\right)_g s+\left(\overline{\mathbf{A}}_0\right)_g\right]g+\mathbf{F}_A+\mathbf{F}_d$$

where
$$\overline{\mathbf{M}} = \mathbf{M}-q\left(\overline{\mathbf{A}}_2\right)_\eta$$
$$\overline{\mathbf{D}} = \mathbf{D}-q\left(\overline{\mathbf{A}}_1\right)_\eta$$
$$\overline{\mathbf{K}} = \mathbf{K}-q\left(\overline{\mathbf{A}}_0\right)_\eta \qquad (5.2.8)$$

The final step in obtaining a state space description is to describe the aerodynamic lag terms as augmented states. Following Tiffany and Adams [1988] the aerodynamic states are defined to combine both elastic and gust modes, thereby minimizing the number of states added

$$\mathbf{X}_{a_l} = -\overline{R}_l\mathbf{I}\mathbf{X}_{a_l}+\left(\overline{\mathbf{A}}_{l+2}\right)_\eta s\eta+\left(\overline{\mathbf{A}}_{l+2}\right)_g sg \qquad (5.2.9)$$

Eq. 5.2.9 shows that for each lag term l, one state is augmented to the system for each mode fitted with aerodynamics. Thus the total number of augmented aerodynamic states is equal to the number of lags times the number of fitted modes.

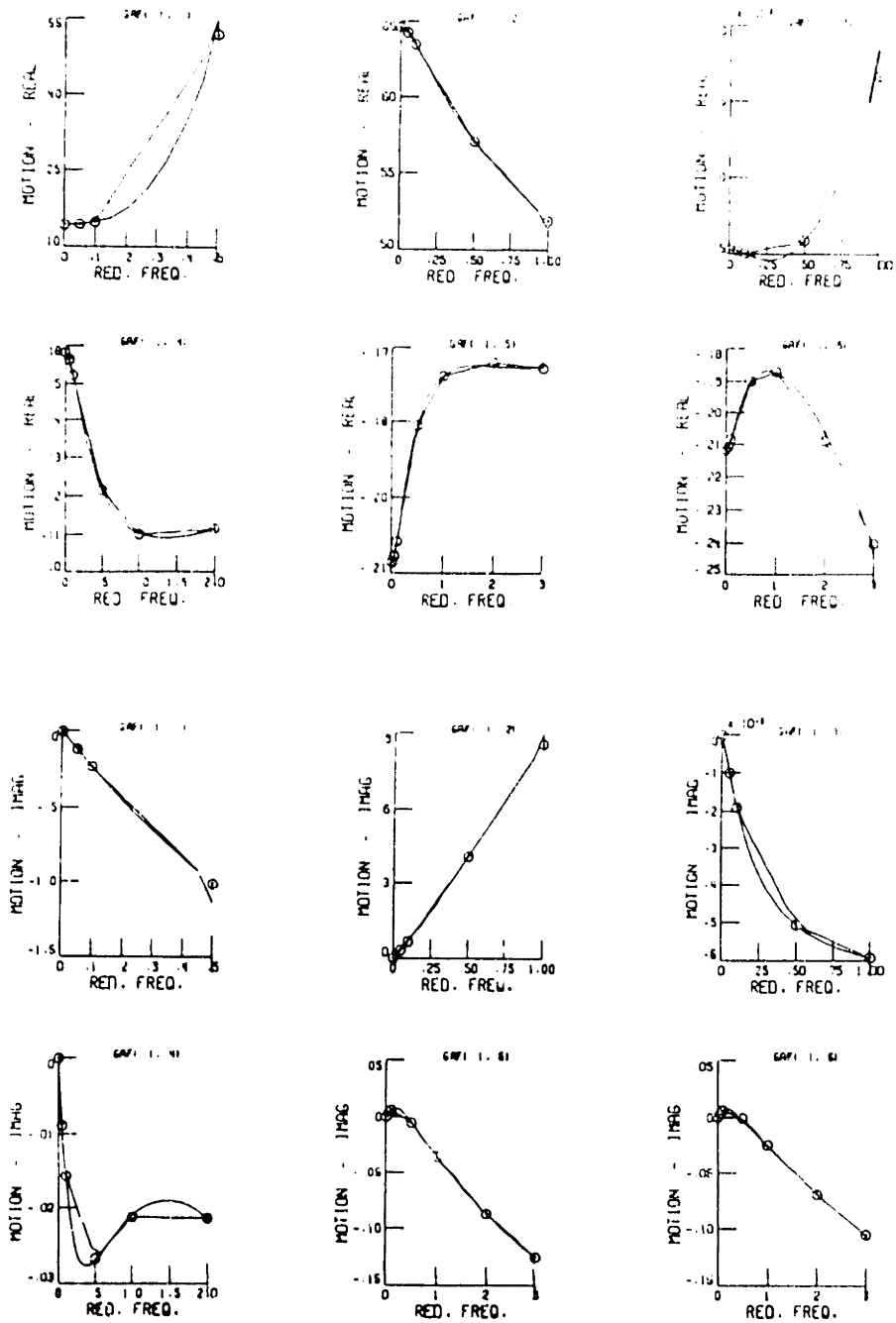

Figure 5.5. Generalized aerodynamic forces (GAFs) and rational function approximations acting on the first mode of the G/E lifting surface at 60 mph. The real and imaginary parts of the aerodynamic forces are plotted versus reduced frequency. Tabular GAFs are indicated by the symbol 'o'.

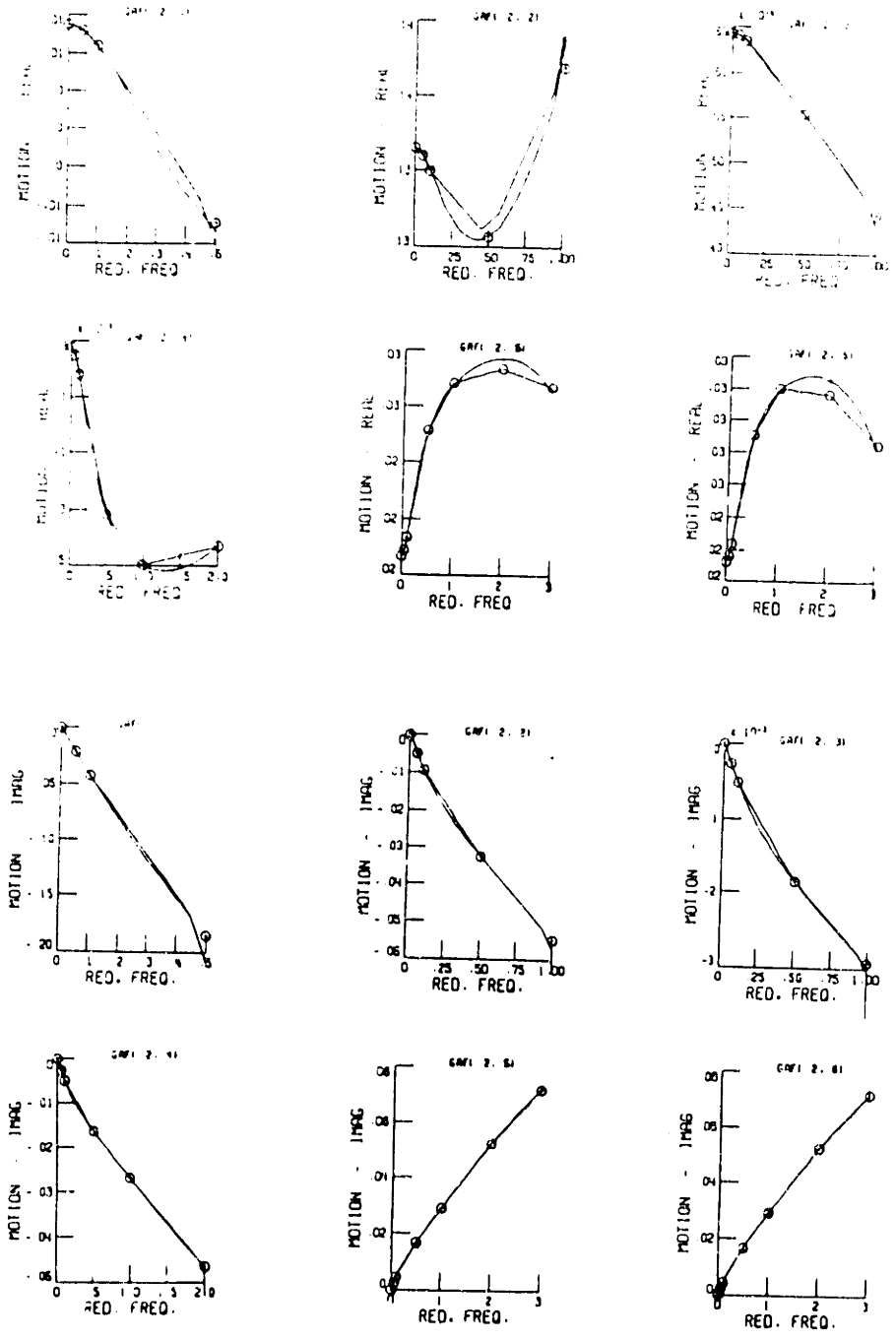

Figure 5.6. Generalized aerodynamic forces (GAFs) and rational function approximations acting on the second mode of the G/E lifting surface at 60 mph. The real and imaginary parts of the aerodynamic forces are plotted versus reduced frequency. Tabular GAFs are indicated by the symbol 'o'.

5.3 Combined Lifting Surface Aeroelastic Model

The aeroelastic behavior of the lifting surface test articles is analyzed by combining the structural and aerodynamic models in a state space representation. A state space representation of the structural and aeroelastic system is obtained by combining Eqs. 5.2.8 and 5.2.9

$$s\mathbf{X} = \mathbf{A}_p\mathbf{X} + \mathbf{B}_p\mathbf{u} + \mathbf{L}_p\mathbf{d} \qquad \mathbf{y} = \mathbf{C}_p\mathbf{X}$$

with $\mathbf{X} = [\eta \quad s\eta \quad \mathbf{X}_a]^T$ and

$$\mathbf{A}_p = \begin{bmatrix} \mathbf{0} & \mathbf{I} & \mathbf{0} & \cdots & \mathbf{0} \\ -\overline{\mathbf{M}}^{-1}\overline{\mathbf{K}} & -\overline{\mathbf{M}}^{-1}\overline{\mathbf{D}} & q\overline{\mathbf{M}}^{-1}[\mathbf{I} & \cdots & \mathbf{I}] \\ \mathbf{0} & \left(\overline{\mathbf{A}}_3\right)_\eta & -\mathbf{I}\overline{R}_1 & \cdots & \mathbf{0} \\ \vdots & \vdots & \vdots & \ddots & \vdots \\ \mathbf{0} & \left(\overline{\mathbf{A}}_{2+l}\right)_\eta & \mathbf{0} & \cdots & -\mathbf{I}\overline{R}_{n_l} \end{bmatrix} \qquad \mathbf{B}_p\mathbf{u} = \begin{bmatrix} \mathbf{0} \\ \overline{\mathbf{M}}^{-1}\mathbf{F}_\Lambda \\ \mathbf{0} \\ \vdots \\ \mathbf{0} \end{bmatrix}$$

$$\mathbf{L}_p\mathbf{d} = \begin{bmatrix} \mathbf{0} \\ \overline{\mathbf{M}}^{-1}\mathbf{F}_d \\ \mathbf{0} \\ \vdots \\ \mathbf{0} \end{bmatrix} + \begin{bmatrix} \mathbf{0} & \mathbf{I} & \mathbf{0} \\ q\overline{\mathbf{M}}^{-1}\left(\overline{\mathbf{A}}_0\right)_g & q\overline{\mathbf{M}}^{-1}\left(\overline{\mathbf{A}}_1\right)_g & q\overline{\mathbf{M}}^{-1}\left(\overline{\mathbf{A}}_2\right)_g \\ \mathbf{0} & \left(\overline{\mathbf{A}}_3\right)_g & \mathbf{0} \\ \vdots & \vdots & \vdots \\ \mathbf{0} & \left(\overline{\mathbf{A}}_{2+l}\right)_g & \mathbf{0} \end{bmatrix} \begin{bmatrix} g \\ sg \\ s^2g \end{bmatrix}$$

$$\mathbf{C}_p = \begin{bmatrix} \psi\left(x_{\text{tip}}, y_{\text{LE}}\right)\Phi & \mathbf{0} & \mathbf{0} \\ \psi\left(x_{\text{tip}}, y_{\text{MC}}\right)\Phi & \mathbf{0} & \mathbf{0} \\ \psi\left(x_{\text{tip}}, y_{\text{TE}}\right)\Phi & \mathbf{0} & \mathbf{0} \end{bmatrix} \tag{5.3.1}$$

This state space aeroelastic system includes both structural η and aerodynamic $\mathbf{X}_a$ modes. The aerodynamic matrices combine with the structural matrices in the form of apparent mass, aerodynamic damping, aerodynamic stiffness and aerodynami lag state terms. Only the aerodynamic states, which model the time delays between the wing motion and the aerodynamic forces created by the motion, increase the number of states needed to describe the system. However, the dynamic response is influenced by all of the aerodynamic terms, and instabilities are caused by both the non-symmetric nature of the aerodynamic mass, damping and stiffness terms as well as the lag states. Note that the gust displacement,

velocity and acceleration terms are dependent on the gust generation device and input spectrum, and are determined by the dynamics of the gust generation disturbance source (see section 4.3). Also note that the system described in Eq. 5.3.1 reduces to the dynamic behavior of the test articles in the bench-top configuration when q equals zero and $\mathbf{F}_d$ equals some finite value. Finally, observe that the outputs of the aeroelastic system (measured by the laser sensors) are described by the output matrix $\mathbf{C}_p$, which is comprised of the *in-vacuo* eigenvalues Φ and the out-of-plane assumed mode tip displacements at the leading edge LE, mid-chord MC and trailing edge TE.

Verification of Lifting Surface Aeroelastic Model

Tabular unsteady aerodynamic data was generated and fits were calculated (similar to those in Figs. 5.5 and 5.6) for the nominal aluminum and G/E lifting surface test articles at 60 mph, and for the modified-for-flutter aluminum test article at 90 mph. The unsteady aerodynamic forces were found at these air speeds for the purpose of obtaining the most accurate aerodynamic model at the air speeds at which the active lifting surfaces were tested (the gust alleviation and command following experiments were conducted at 60 mph and the flutter experiments at 90 mph). However, because of the low Mach numbers involved, it can be assumed that the aerodynamic forcing functions are valid over the entire compressible range.

Eq. 5.3.1 is used to calculate the coupled aeroelastic vibration frequencies of the lifting surface test articles. In calculating the lifting surface natural frequencies, structural modes with experimentally updated frequencies (as described in section 5.1) are utilized. The structural modes are updated with frequencies recorded during previous wind tunnel experiments with the air speed set to zero. Note that these frequencies differ slightly from those measured in the bench-top experiments and current wind tunnel configuration. The small discrepancies are most likely due to differences in the mounting hardware, which provide the cantilever support for the lifting surfaces, and constraints on the volume of air resting in the wind tunnel test section.

The analytically predicted and experimentally measured natural frequencies of the lifting surfaces in the wind tunnel test configuration are

reported in Tables 5.3, 5.4 and 5.5 for the aluminum, G/E and modified-for-flutter aluminum test articles, respectively. Theoretical predictions are listed for frequency and damping at 0, 20, 40, 60, 80 and 100 mph. The experimental frequencies were measured in the wind tunnel at speeds of 0, 20, 40 and 60 mph for the aluminum and G/E wings, while frequencies where measured every 10 mph up to the flutter point for the modified-for-flutter aluminum test article. The tables show good agreement between the predicted and measured frequencies. The aluminum lifting surface had an average error of -2.10 percent with a variance of 9.62 in the first two modes over air speeds ranging from 0 to 60 mph. Similarly the G/E lifting surface had an average error of +2.05 percent with a variance of 18.5 in the first two modes. The result for the modified-for-flutter wing did not correlate as well, having an average error of +0.24 percent with a variance of 51.8 in the first two modes for 0 to 80 mph. The large variance was attributed to difficulties in modeling the structural dynamics of the brace used to support the huge mass added to make the wing flutter within the wind tunnel operating range. Fortunately, the model was found to have sufficient accuracy for predicting the flutter speed and designing controllers for flutter suppression.

Tables 5.3, 5.4 and 5.5 also show that large amounts of damping were introduced into the low frequency modes by the aerodynamics at speeds above 40 mph. At the gust alleviation test velocity of 60 mph the damping in the first mode increased by more than an order of magnitude, and the damping in the second, third and fourth modes approximately doubled. Note that at moderate air speeds (40 to 80 mph), the aerodynamic damping of the lower modes is considerably larger for the G/E relative to the aluminum lifting surface. This increased damping is due to the washin configuration of the G/E plate and is typical of such aeroelastically tailored designs. The aerodynamic damping has tremendous implications for controlling aeroelastic systems since it is easier to achieve significant vibration reduction in structures having lightly damped low frequency and heavily damped high frequency modes. Thus, designing controllers for gust alleviation (lightly damped low frequency and heavily damped high frequency modes) was found to be a much more difficult control problem than designing controllers for bench-top disturbance rejection (all modes lightly damped) for the test articles considered in this study. Finally, the data suggests that the

unsteadiness in the aerodynamics was a significant factor. The reduced frequencies ranged from 0.03 to 0.9 for the gust alleviation and command following experiments, and the reduced flutter frequency was approximately 0.03.

Mode 1

MPH	Theory (Hz)	Red. Freq. k	% Damping	Exp. (Hz)	% Error
0	7.20		1.5	7.50	-4.0
20	7.16	0.171	4.5	7.50	-4.5
40	7.16	0.086	8.1	7.40	-3.2
60	7.10	0.057	14.2	6.75	5.2
80	6.98	0.042	21.4		
100	6.75	0.032	32.7		

Mode 2

MPH	Theory (Hz)	Red. Freq. k	% Damping	Exp. (Hz)	% Error
0	35.5		1.5	36.0	-1.4
20	35.1	0.840	2.0	36.0	-2.5
40	34.4	0.412	2.6	35.7	-3.6
60	33.2	0.265	3.2	34.1	-2.7
80	31.3	0.187	3.8		
100	28.6	0.137	4.2		

Mode 3

MPH	Theory (Hz)	Red. Freq. k	% Damping	Exp. (Hz)	% Error
0	49.5		1.5	49.5	0.0
20	49.0	1.173	1.8	50.7	-3.4
40	49.0	0.587	2.2	50.4	-2.8
60	49.1	0.392	2.6	49.6	-1.0
80	49.2	0.294	3.0		
100	49.3	0.236	3.4		

Mode 4

MPH	Theory (Hz)	Red. Freq. k	% Damping	Exp. (Hz)	% Error
0	116.		1.5	115.	0.9
20	115.	2.753	1.7		
40	115.	1.376	1.8		
60	115.	0.918	2.0		
80	115.	0.688	2.1		
100	114.	0.546	2.3		

Table 5.3. Analytically predicted and wind tunnel measured natural frequencies for the aluminum lifting surface.

Mode 1

MPH	Theory (Hz)	Red. Freq. k	% Damping	Exp. (Hz)	% Error
0	6.88		1.5	6.88	0.0
20	6.84	0.164	7.6	6.56	4.3
40	6.67	0.080	16.6	6.25	6.7
60	6.25	0.050	29.1	5.70	9.6
80	5.33	0.032	53.2		
100	2.01	0.010	230.0		

Mode 2

MPH	Theory (Hz)	Red. Freq. k	% Damping	Exp. (Hz)	% Error
0	34.2		1.5	34.5	-0.9
20	33.8	0.809	2.2	33.9	-0.3
40	32.9	0.394	3.0	33.2	-0.9
60	31.3	0.250	4.0	32.0	-2.2
80	28.7	0.172	4.7		
100	25.0	0.120	3.7		

Mode 3

MPH	Theory (Hz)	Red. Freq. k	% Damping	Exp. (Hz)	% Error
0	47.8		1.5	48.0	-0.4
20	47.2	1.130	1.9	46.6	1.3
40	47.1	0.564	2.2	46.6	1.1
60	47.1	0.376	2.6	47.5	-0.8
80	47.1	0.282	2.9		
100	47.1	0.226	3.3		

Mode 4

MPH	Theory (Hz)	Red. Freq. k	% Damping	Exp. (Hz)	% Error
0	110.		1.5	111.	-0.9
20	109.	2.609	1.7	111.	-1.8
40	109.	1.305	1.9	110.	-0.9
60	109.	0.870	2.2	110.	-0.9
80	108.	0.646	2.4		
100	108.	0.517	2.6		

Table 5.4. Analytically predicted and wind tunnel measured natural frequencies for the G/E lifting surface.

Mode 1

MPH	Theory (Hz)	Red. Freq. k	% Damping	Exp. (Hz)	% Error
0	3.04		1.5	2.80	8.6
20	3.07	0.073	2.4	2.88	6.6
40	3.19	0.038	3.3	2.95	8.1
60	3.45	0.028	4.2	3.25	6.2
80	4.22	0.025	6.3	4.37	-3.4
90	5.52	0.029	30.1		
100	4.63	0.022	69.5		

Mode 2

MPH	Theory (Hz)	Red. Freq. k	% Damping	Exp. (Hz)	% Error
0	12.3		1.5	13.3	-7.5
20	12.0	0.287	2.2	13.3	-9.8
40	11.4	0.136	3.2	12.4	-8.1
60	10.3	0.082	4.6	10.5	-1.9
80	8.03	0.048	6.6	7.75	3.6
90	5.68	0.030	-13.4		
100	5.19	0.025	-42.8		

Mode 3

MPH	Theory (Hz)	Red. Freq. k	% Damping	Exp. (Hz)	% Error
0	33.6		1.5	28.4	18.3
20	33.4	0.800	1.6		
40	33.2	0.397	1.7		
60	32.7	0.261	1.9		
80	32.0	0.192	2.1		
90	31.5	0.168	2.1		
100	31.0	0.148	2.2		

Mode 4

MPH	Theory (Hz)	Red. Freq. k	% Damping	Exp. (Hz)	% Error
0	45.3		1.5	43.	5.3
20	44.9	1.075	1.8		
40	44.9	0.537	2.0		
60	44.9	0.358	2.1		
80	45.0	0.269	2.2		
90	45.1	0.240	2.2		
100	45.2	0.216	2.3		

Table 5.5. Analytically predicted and wind tunnel measured natural frequencies for the modified-for-flutter aluminum lifting surface.

The behavior of the lifting surfaces can be examined further by plotting the movement of the system poles with air speed. Such aerodynamic root loci are shown in Figs. 5.7, 5.8 and 5.9 for the aluminum, G/E and modified-for-flutter aluminum test articles, respectively. The poles are plotted for air speeds from 0 to 100 mph at increments of 5 mph. For each wing, the poles move farther into the left half-plane as the air speed initially increases from zero. The movement of the poles into the left half-plane, which indicates an increase in damping, continues at low air speeds. Then at some intermediate air speed the poles associated with the first torsion mode reverse direction and move rapidly toward the imaginary axis. This reversal of direction, which indicates that the system is approaching an instability, occurs at about 90, 80 and 70 mph for the aluminum, G/E and modified-for-flutter aluminum lifting surfaces, respectively. The poles associated with the first bending mode of the aluminum and G/E wings decrease toward the real axis indicating either a pure torsion flutter or bending divergence instability will occur, while the bending poles increase towards the torsion poles for the modified-for-flutter wing resulting in a coalescence flutter instability. Note that the poles on the real axis are aerodynamic lag poles, since the bending poles do not reach the real axis for air speeds within the wind tunnel limit.

Fig. 5.7 shows that the aluminum lifting surface is far from any instabilities at the gust alleviation and command following test velocity of 60 mph. In fact, the poles of the aluminum lifting surface are predicted to be stable well above the operating range of the wind tunnel (100 mph), with flutter at 130 mph and divergence at 165 mph. The poles of the G/E lifting surface are also stable over the entire wind tunnel range, as indicated in Fig. 5.8. Flutter and divergence are predicted to occur at the lower air speeds of 110 and 115 mph, respectively. In contrast, the modified-for-flutter lifting surface, shown in Fig. 5.9, is predicted to flutter below the tunnel limit at 87.6 mph. The flutter speed for this wing was experimentally measured at 88 mph. The flutter mode was predicted and observed to be due to a coalescence of the first bending and first torsion modes. The classical coalescence nature of this instability is clearly illustrated in Fig. 5.10, which plots the natural frequencies of the first two modes versus air speed for the modified-for-flutter aluminum lifting surface. The bending pole increases and the torsion pole decreases with air speed until coalescence flutter occurs.

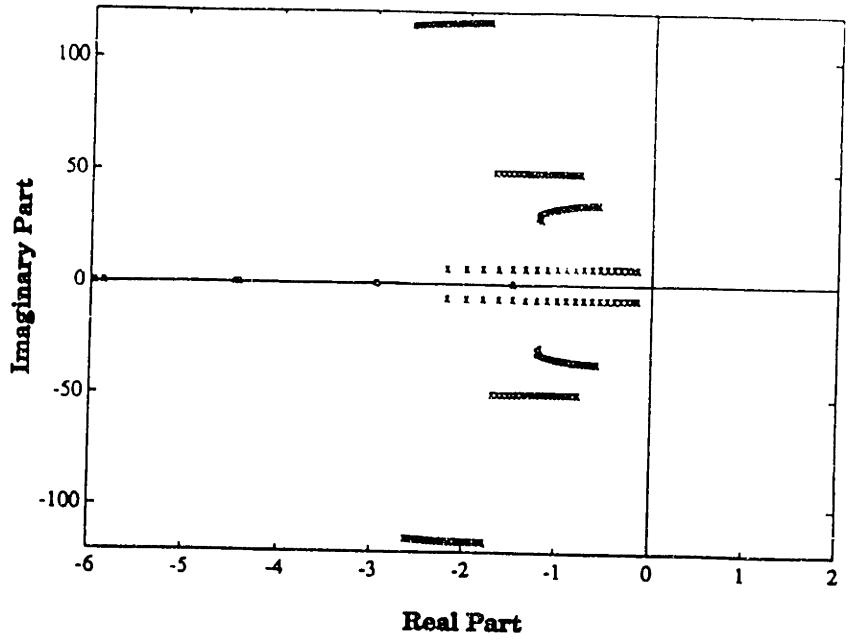

Figure 5.7. Poles of the aluminum lifting surface for air speeds increasing from zero to the wind tunnel limit of 100 mph. All poles are on the left hand side of the imaginary axis, indicating the system is stable.

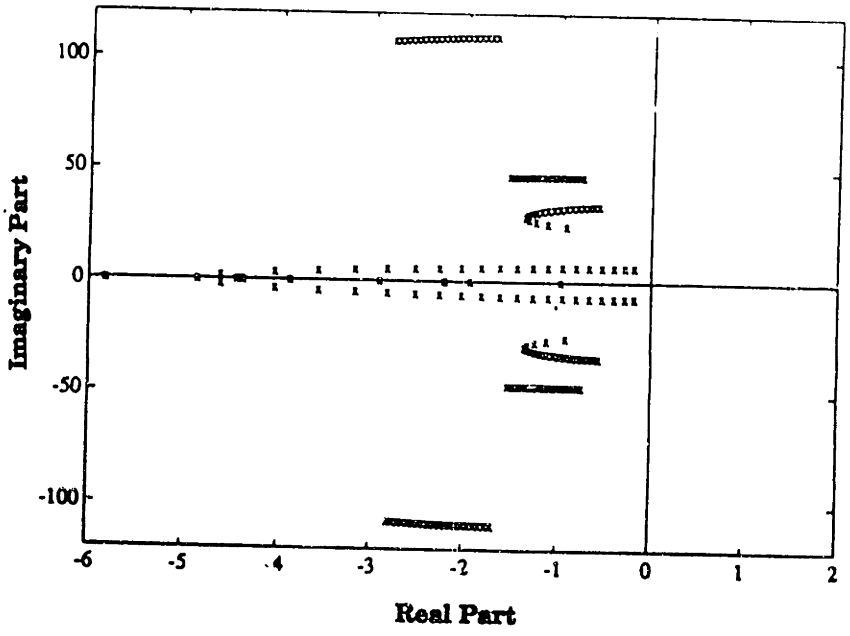

Figure 5.8. Poles of the G/E lifting surface for air speeds increasing from zero to the wind tunnel limit of 100 mph. All poles are on the left hand side of the imaginary axis, indicating the system is stable.

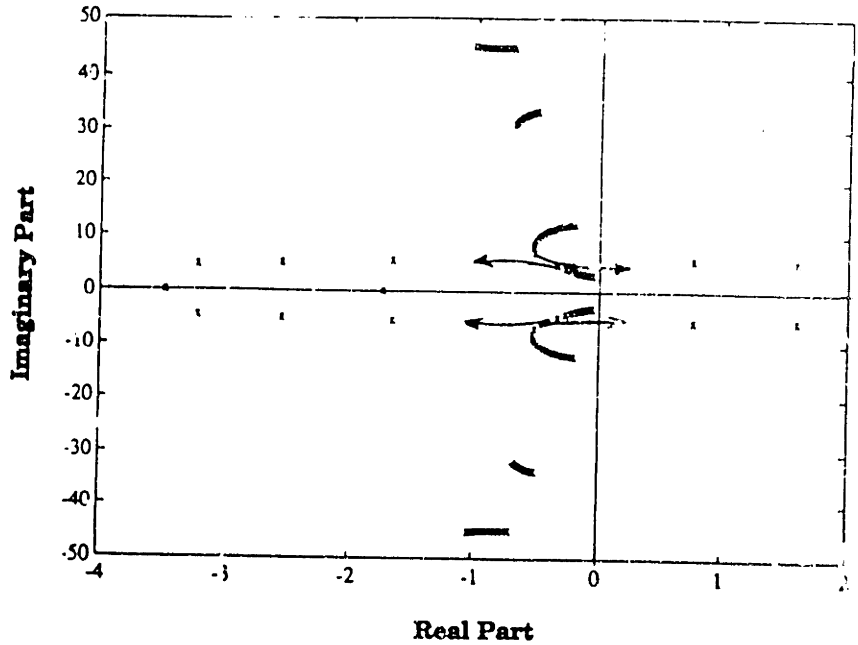

Figure 5.9. Poles of the modified-for-flutter aluminum lifting surface for air speeds increasing from zero to the wind tunnel limit of 100 mph. Above the flutter speed (88 mph) a pair of poles have moved to the right hand side of the imaginary axis, making the system unstable.

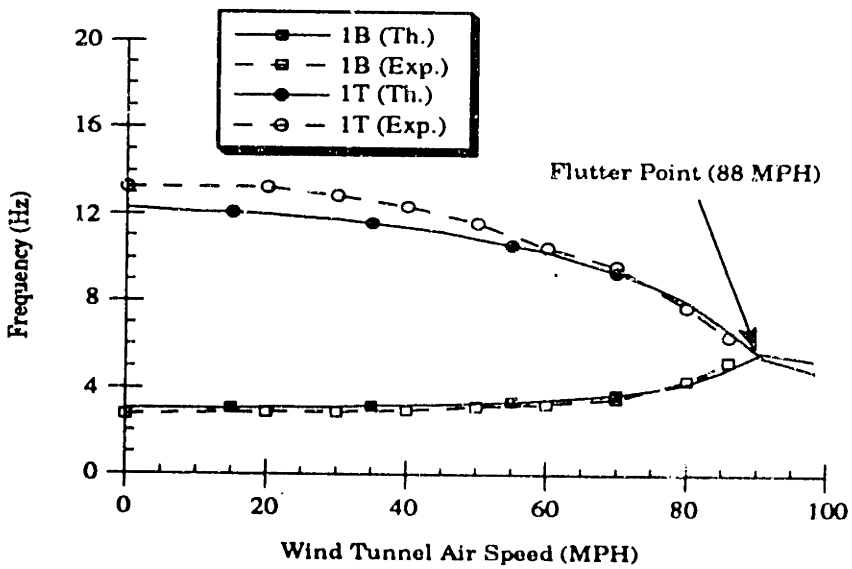

Figure 5.10. Natural frequency of the modified-for-flutter aluminum lifting surface bending and torsion modes for air speeds increasing from zero to the wind tunnel limit of 100 mph. At the flutter speed (88 mph) the poles have coalesced causing an instability.

5.4 Full Order Analytic Model

The plant model of any controlled system must be augmented to include the dynamics of sensors, actuators and any other electronic components in the feedback path such as anti-aliasing filters and amplifiers. A block diagram of the system components to be modeled is shown in Fig. 5.11. Incorporating all the system components is easily facilitated by transforming the structural system into state space form ($\mathbf{A}_p$, $\mathbf{B}_p$, $\mathbf{C}_p$ and $\mathbf{L}_p$ of Eq. 5.3.1). The state space model is then combined with the appropriate dynamics associated with the other components in the system.

The full bench-top system created had 73 states, while 93 states were needed to describe the test articles in the wind tunnel. Forty of the states were associated with the twenty structural modes, and 18 states were used to model the unsteady aerodynamic lags. The remaining states resulted from the dynamics of three optical sensors (modeled with 1 pole at 700 Hz), twelve piezoceramic actuator arrays (no dynamics) and power amplifiers (no dynamics) and anti-aliasing filters (modeled with 2 poles at 1000 Hz for each of the 3 sensor outputs and 2 poles at 2500 Hz for each of the 12 control inputs). The disturbance source model added no additional dynamics to the system for the bench-top test, however two additional states were included in the wind tunnel model to account for the roll-off of the gust spectrum produced by the gust generator. This large order system *evaluation* model was used to calculate the open and closed loop disturbance transfer functions and to evaluate the stability and performance of the control laws designed. The dynamics of this large order open loop system can be described in either a state space

$$\dot{\mathbf{x}} = \mathbf{A}\mathbf{x} + \mathbf{B}\mathbf{u} + \mathbf{L}\mathbf{d} \qquad \mathbf{y} = \mathbf{C}\mathbf{x} \tag{5.3.1}$$

or transfer function representation

$$\begin{aligned} \mathbf{y} &= \mathbf{G}_c(s)\mathbf{u} \qquad & \mathbf{G}_c &= \mathbf{C}(s\mathbf{I} - \mathbf{A})^{-1}\mathbf{B} \\ \mathbf{y} &= \mathbf{G}_d(s)\mathbf{d} \qquad & \mathbf{G}_d &= \mathbf{C}(s\mathbf{I} - \mathbf{A})^{-1}\mathbf{L} \end{aligned} \tag{5.3.2}$$

where $\mathbf{G}_c(s)$ contains the control and $\mathbf{G}_d(s)$ holds the disturbance transfer functions.

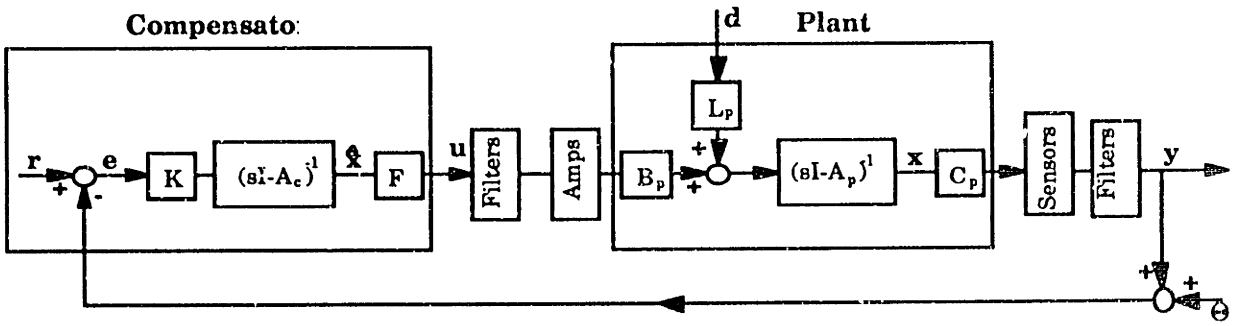

Figure 5.11. Block diagram of the experimental system including the lifting surface (A_p, B_p, C_p, and L_p), compensator (A_c,K, and F), disturbance (d) and measurement noise (Θ).

5.5 Model Order Reduction

Since the use of large order evaluation models for developing model based control laws usually leads to similarly large order compensators, which are difficult to implement at high rates in real time and unnecessary for obtaining effective controllers, the 73 or 93 state evaluation model was reduced to a lower order *design* model. The reduction was based on the Hankel singular values of the system. The Hankel singular values were found by first obtaining a minimal realization and then balancing the system using the algorithm of B. C. Moore [1981] in Pro-Matlab. The states associated with the Hankel singular values greater than 0.1% of the maximum Hankel singular value were retained in the model. The steady state components of the discarded states were also retained in the model.

This procedure reduced the 73 state bench-top evaluation model to a 22 state design model for the aluminum and G/E test articles and reduced the 93 state wind tunnel evaluation model to 32, 34, and 38 states for the aluminum, G/E and modified-for-flutter aluminum wind tunnel evaluation models, respectively. It was found that the disturbance to sensor output (**y/d**) and control input to sensor output (**y/u**) transfer functions of the design models were nearly identical to those of the associated evaluation models in the evaluation bandwidth (500 Hz on the bench and 200 Hz in the wind tunnel). Further, it was found that increasing the order of the design model had no effect on the transfer functions, the controllers designed or their performance.

The accuracy of the analytical model and the fact that model fidelity is not affected by the model reduction procedure can be shown by plotting the singular values of the control transfer function matrix $\mathbf{G}_c(s)$. Figs. 5.12 and 5.13 display the analytically predicted and experimentally measured transfer function matrix maximum singular values for the aluminum and G/E test articles on the bench-top, respectively. The figures show excellent agreement between the predicted and measured frequencies and magnitudes. Also note that large responses are found at high as well as low frequencies.

Similarly, Figs. 5.14 and 5.15 display the analytically predicted and experimentally measured transfer function matrix maximum singular values for the aluminum and G/E test articles in the wind tunnel at 60 mph, respectively. As before the theory and experiment are in good agreement, but it appears that the torsion modes were excited more than anticipated in the wind tunnel. Also, turbulence in the free stream flow raised the noise floor considerably. The wind tunnel singular value plots show the significant amount of aerodynamic damping introduced in the first bending and torsion modes, relative the damping found on the bench-top. However, it can be seen that the higher frequency modes remain lightly damped in the wind tunnel. Thus, the wind tunnel transfer function magnitudes do not roll off as quickly as the bench-top magnitudes. Note that the laser sensor output filters included an additional times ten gain for the bench-top experiments. The additional output gain increased the analog to digital conversion accuracy of the relatively smaller bench-top sensor signals.

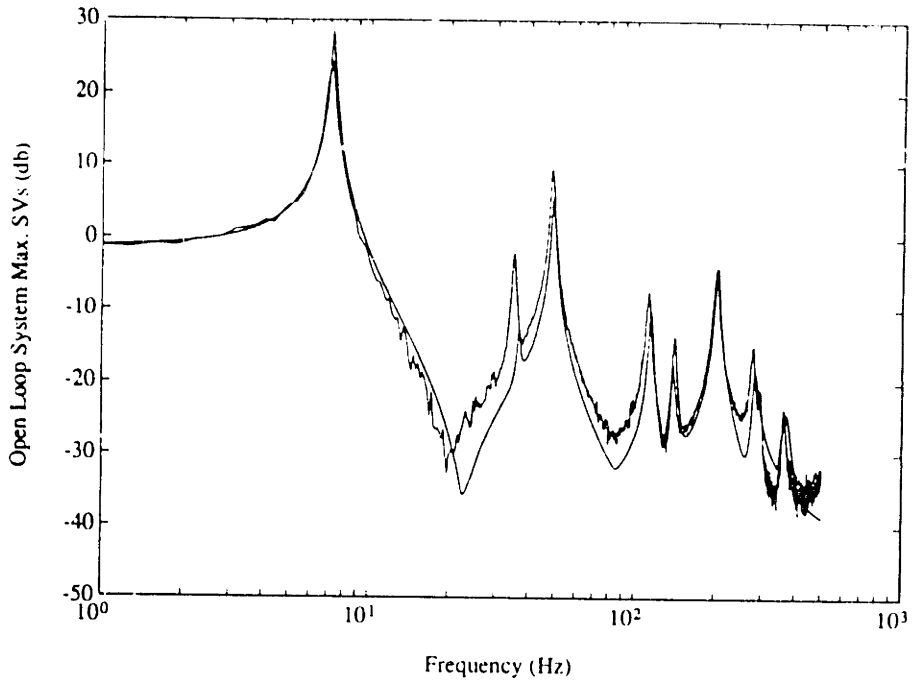

Figure 5.12. Maximum singular values of the control transfer function matrix $G_c(s)$ for the aluminum test article on the bench-top. Analytical and experimental singular values are plotted.

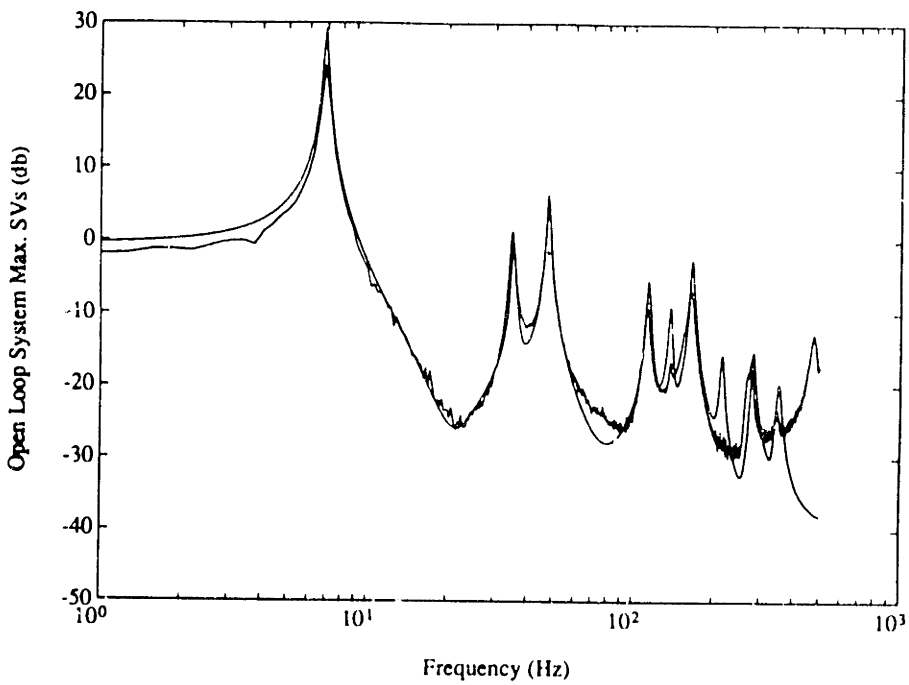

Figure 5.13. Maximum singular values of the control transfer function matrix $G_c(s)$ for the G/E test article on the bench-top. Analytical and experimental singular values are plotted.

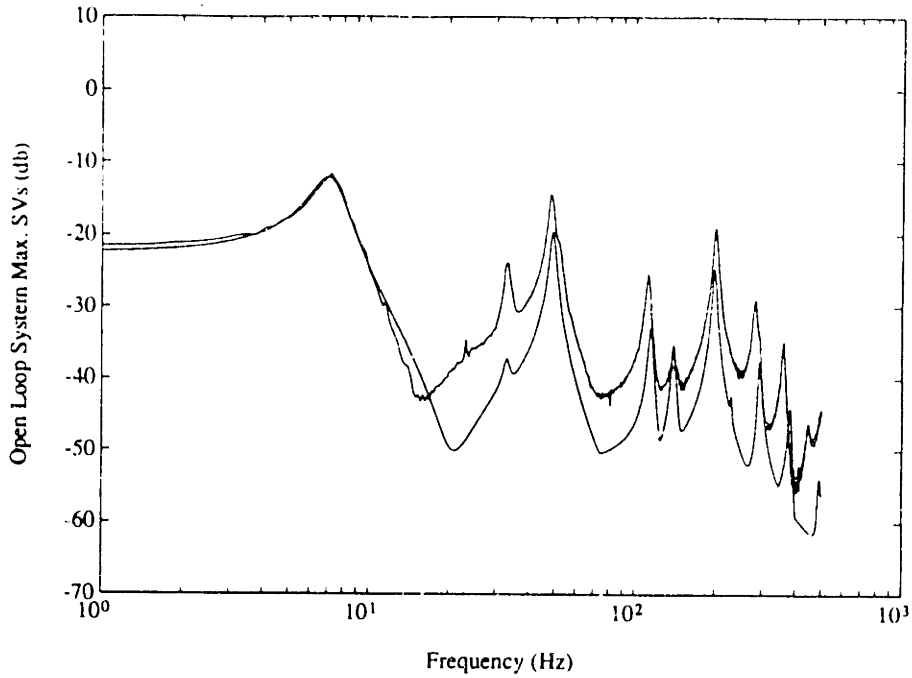

Figure 5.14. Maximum singular values of the control transfer function matrix $G_c(s)$ for the aluminum lifting surface in the wind tunnel at 60 mph. Analytical and experimental singular values are plotted.

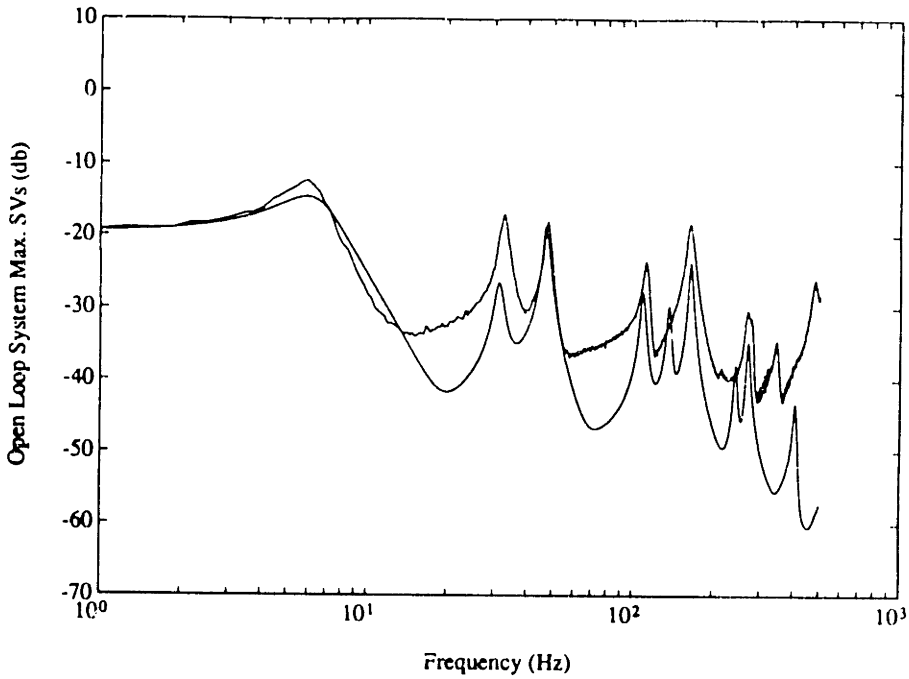

Figure 5.15. Maximum singular values of the control transfer function matrix $G_c(s)$ for the G/E lifting surface in the wind tunnel at 60 mph. Analytical and experimental singular values are plotted.

5.A Appendix: Assumed Mode Mathematical Description.

All of the assumed modes ψ_i used in the Ritz analysis to model the plate-like test articles were composed of both spanwise ψ_{x_i} and chordwise ψ_{y_i} non-dimensional functions. The dynamic spanwise beam bending modes (1-5) assumed were those of the exact solution to the cantilever beam bending problem along the span with a constant chordwise distribution

$$\psi_{x_i}(\bar{x}) = \left[\cosh(\beta_i \bar{x}) - \cos(\beta_i \bar{x})\right] - \sigma_i\left[\sinh(\beta_i \bar{x}) - \sin(\beta_i \bar{x})\right]$$
$$\psi_{y_i}(\bar{y}) = \text{constant}$$
$$\text{where} \quad \bar{x} = x/L \quad \text{and} \quad \bar{y} = y/c \tag{5.A.1}$$

The constants σ_i and B_i in Eq. 5.A.1 are listed in Table 5.6 and were taken from Blevens [1984].

Assumed Mode	σ_i	β_i
1	0.734096	1.875104
2	1.018467	4.694091
3	0.999224	7.854757
4	1.000034	10.99554
5	0.999998	14.13717

Table 5.6. Coefficients of the spanwise beam bending assumed modes for the aluminum and G/E plates.

The spanwise torsional assumed modes (6-9) were found from a Torsion Partial Ritz analysis (similar to the analysis of section 3.3) for an isotropic plate with an assumed linear twist distribution

$$\bar{w}(\bar{x}, \bar{y}) = \theta(\bar{x})\bar{y} \tag{5.A.2}$$

The Torsion Partial Ritz analysis used the variational statement of stationary energy, assumed periodic motion and the assumed displacement distribution of Eq. 5.A.2 to derive the equation governing spanwise twist for a cantilever plate

$$\frac{\partial^4 \theta}{\partial \bar{x}^4} - \left[48 \frac{D_{66}}{D_{11}}\left(\frac{L}{c}\right)^2\right]\frac{\partial^2 \theta}{\partial \bar{x}^2} + \left[\frac{\lambda^2 \mu L^4}{D_{11}}\right]\theta = 0 \tag{5.A.3}$$

Note that in addition to the usual torsional stiffness and rotary inertia terms, Eq. 5.A.3 includes the effects of root warping. The homcgeneous solution and assumed shape of the torsion modes is given by

$$\psi_{x_i}(\bar{x}) = T_{i1}\cos(g_i\bar{x}) + T_{i2}\sin(g_i\bar{x}) + T_{i3}\cosh(f_i\bar{x}) + T_{i4}\sinh(f_i\bar{x})$$
$$\psi_{y_i}(\bar{y}) = \bar{y} \qquad (5.A.4)$$

where the torsional constants g_i, f_i and T_{ij} were found by applying the appropriate boundary conditions and solving the resulting transcendental equation [Crawley and Dugundji, 1980]. The constants are listed in Table 5.7 for the aluminum (AL) and graphite epoxy (G/E) test articles.

Mode	g_i	f_i	T_{i1}	T_{i2}	T_{i3}	T_{i4}
AL 6	1.777237	8.054099	-0.220694	1.000000	0.220694	-0.220694
AL 7	5.051262	9.339443	-0.540795	1.000000	0.540795	-0.540853
AL 8	8.121630	11.29915	-0.718797	1.000000	0.718797	-0.718782
AL 9	11.18019	13.66406	-0.818217	1.000000	0.818217	-0.818219
G/E 6	1.780696	7.915441	-0.225003	1.000000	0.225003	-0.224965
G/E 7	5.050597	9.219103	-0.547773	1.000000	0.547773	-0.547840
G/E 8	8.117240	11.19700	-0.724964	1.000000	0.724964	-0.724948
G/E 9	11.17561	13.57857	-0.823031	1.000000	0.823031	-0.823033

Table 5.7. Coefficients of the spanwise twist distribution of the torsional assumed modes for the aluminum and G/E plates.

The dynamic chordwise bending modes (10, 11) were assumed to have the chordwise distribution of a free-free, free-free beam

$$\psi_{y_i}(\bar{y}) = \left[\cosh(\beta_{ci}\bar{y}) + \cos(\beta_{ci}\bar{y})\right] - \sigma_{ci}\left[\sinh(\beta_{ci}\bar{y}) + \sin(\beta_{ci}\bar{y})\right] \qquad (5.A.5)$$

where the constants σ_{ci} and B_{ci} are listed in Table 5.8.

Assumed Mode	σ_{ci}	β_{ci}
10	0.982502	4.730041
11	1.000777	7.853205

Table 5.8. Coefficients of the chordwise distribution of the dynamic chordwise bending assumed modes for the aluminum and graphite epoxy plates.

The spanwise deflection distributions for these modes were calculated from a Camber Partial Ritz analysis. The Camber Partial Ritz analysis was similar to that used for obtaining the torsion mode shapes, however a spanwise camber distribution was assumed for the Camber Partial Ritz

$$\bar{w}(\bar{x},\bar{y}) = \kappa(\bar{x})\left[4\bar{y}^2 - \frac{1}{3}\right] \tag{5.A.6}$$

By substituting this camber distribution into the variational statement of stationary energy and once again assuming periodic motion, the equation governing the spanwise camber distribution was found

$$\frac{\partial^4 \kappa}{\partial \bar{x}^4} - \left[240\frac{D_{66}}{D_{11}}\left(\frac{L}{c}\right)^2\right]\frac{\partial^2 \kappa}{\partial \bar{x}^2} + \left[720\frac{D_{22}}{D_{11}}\left(\frac{L}{c}\right)^4 - \frac{\lambda^2 \mu L^4}{D_{11}}\right]\kappa = 0 \tag{5.A.7}$$

As before, the solution to this differential equation was found by applying the appropriate boundary conditions and solving the resulting transcendental equation. The homogeneous solutions for these dynamic camber modes (10, 11) of the test articles were found to be

$$\psi_{x_i}(\bar{x}) = C_{i1}\cos(g_i\bar{x}) + C_{i2}\sin(g_i\bar{x}) + C_{i3}\cosh(f_i\bar{x}) + C_{i4}\sinh(f_i\bar{x}) \tag{5.A.8}$$

For the static (13) and segmented (19) camber modes, a particular solution (resulting from a constant strain actuator applied moment) of Eq. 5.A.7 was used to find the assumed spanwise camber distributions. These assumed shape functions were found to be

$$\psi_{x_i}(\bar{x}) = C_{i1}\cos(g_i\bar{x}) + C_{i2}\sin(g_i\bar{x}) + C_{i3}\cosh(f_i\bar{x}) + C_{i4}\sinh(f_i\bar{x}) + C_{i5} \tag{5.A.9}$$

The constants and coefficients of Eqs. 5.A.8 and 5.A.9 used in the Ritz analysis are listed in Table 5.9.

Mode	g_i	f_i	C_{i1}	C_{i2}	C_{i3}	C_{i4}	C_{i5}
AL 10, 11	1.66399	17.6442	1.00000	-10.6036	-1.00000	1.00000	–
G/E 10, 11	1.67572	10.3106	0.99996	-6.15292	-0.99996	1.00000	–
AL	-2.43329	-7.73280	0.25000	-0.79436	0.25000	0.24997	-0.50000
13, 16	+7.73270j	+2.43329j	+0.79434j	+0.24997j	-0.79434j	-0.79436j	+0.00000j
G/E	-1.22570	-7.29742	0.36011	-2.14362	0.36011	0.36005	-0.72022
13, 16	+7.29742j	+1.22570j	+2.14365j	+0.36005j	-2.14365j	-2.14365j	+0.0000j

Table 5.9. Coefficients of the spanwise camber distribution of the dynamic, static and segmented chordwise bending assumed modes for the aluminum and G/E plates.

5.B Appendix: Three-dimensional *in-vacuo* mode shapes.

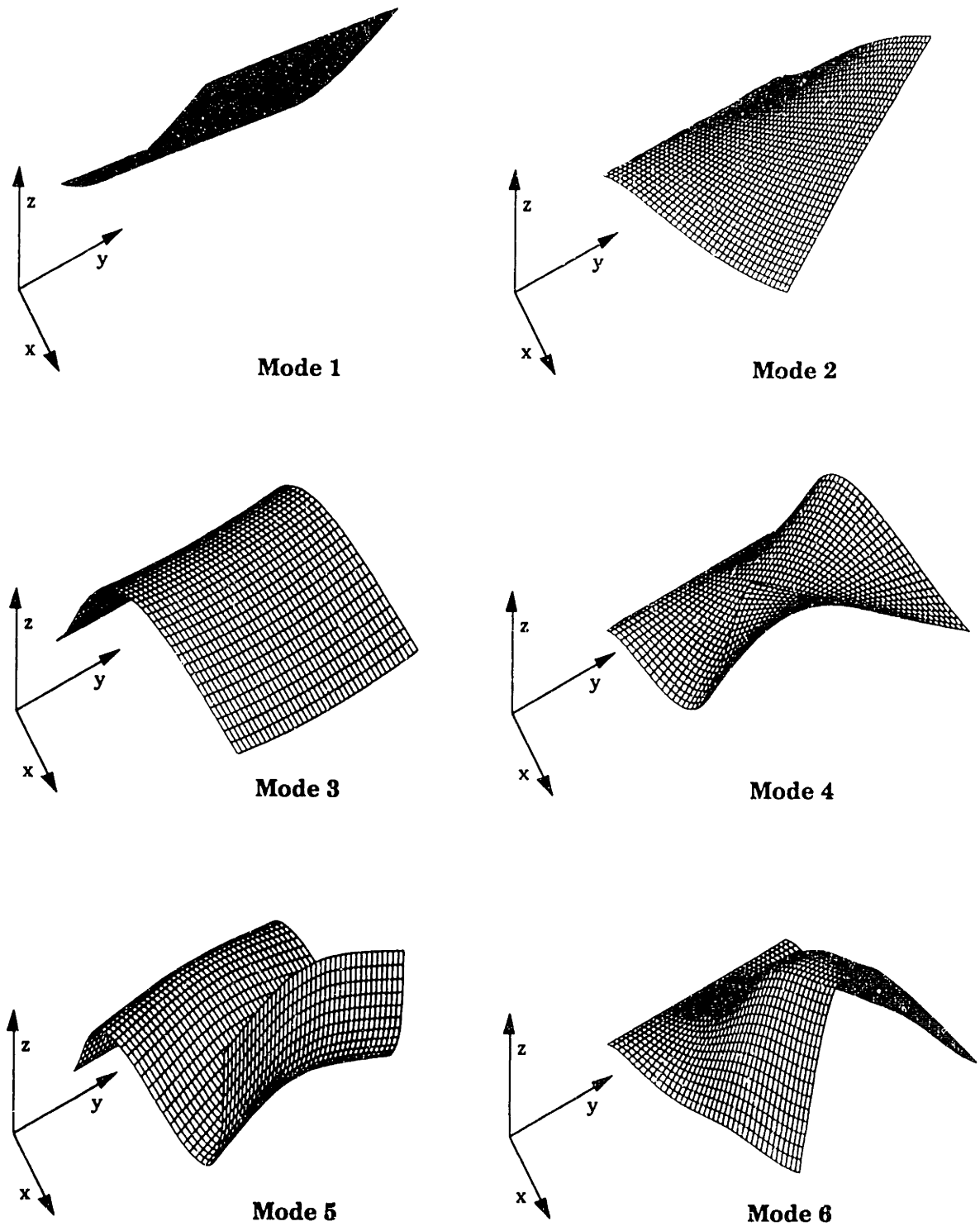

Figure 5.16. Three dimensional plots of the first six natural vibration mode shapes of the aluminum test article.

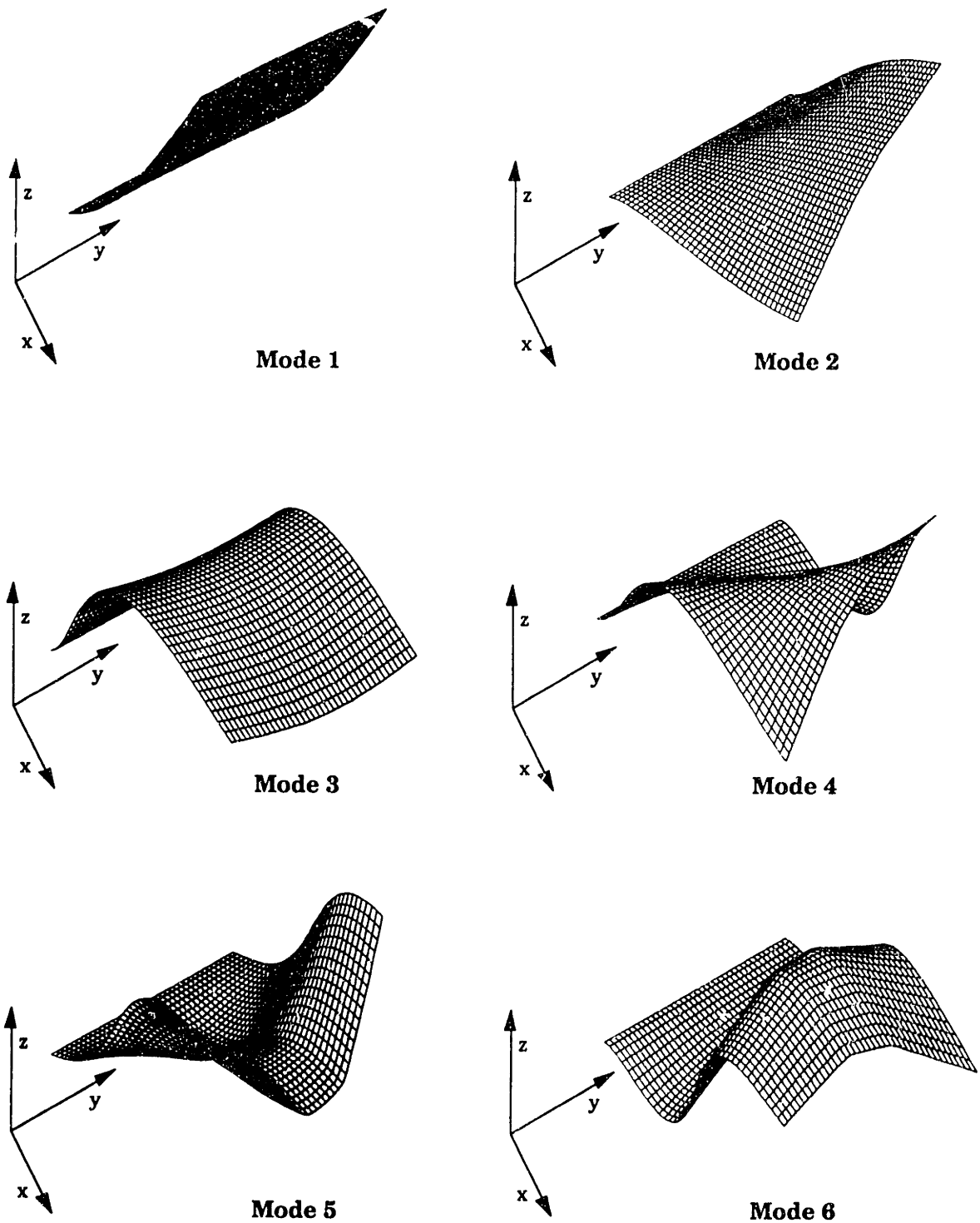

Figure 5.17. Three dimensional plots of the first six natural vibration mode shapes of the graphite/epoxy test article.

Chapter 6. Control Law Synthesis

The first step necessary in designing control laws for the active lifting surfaces is to define the performance objectives and metrics for the controlled systems. The dynamic aeroelastic control performance objectives of greatest interest include flutter suppression, vibration suppression and gust alleviation. In terms of control system design, these issues translate into those of stability, plant regulation and disturbance rejection, respectively. Since a well-regulated plant automatically carries the properties of guaranteed stability and good disturbance rejection, the control law design problem reduces to that of plant regulation. Thus, the compensator design goal for the bench-top disturbance rejection, wind tunnel gust alleviation and wind tunnel flutter experiments is to turn the system into one which is well-regulated, and similar compensator design techniques may be used in each case. On the other hand, well-regulated plants are not necessarily good for command following, and command following compensators must be designed using procedures which differ considerably from those used for plant regulation.

Performance metrics for the bench-top disturbance rejection, and wind tunnel gust alleviation and flutter suppression control objectives can be defined by quadratic cost functions which measure the output **y** RMS response. The outputs **y** are the response of the lifting surfaces as measured by the laser displacement sensors. Defining the performance index as a cost function enables the cost used in the LQG design synthesis procedure to be both selected in a logical manner and a meaningful measure of controller performance (in fact the cost is exactly the performance metric). The specifics of the design procedure used in the linear quadratic regulator (LQR) and Kalman filter portions of the model based LQG compensator synthesis are described below for the bench-top and wind tunnel tests. The bench-top disturbance rejection and wind tunnel gust alleviation designs make use of essentially the same cost minimization procedure. The wind tunnel flutter suppression controllers are also designed by cost minimization, but the plants being controlled in this case are unstable. In contrast, command following performance is specified in the frequency domain. Thus, command following controllers are designed to meet frequency domain specifications using the

LQG-LTR method, which manipulates the LQG cost into a form that can be used to impose frequency domain constraints.

Initially, control laws were evaluated with the piezoceramic actuators grouped in various combinations. It was found that the best actuator control authority was achieved by dividing the piezoceramic wafers into three actuator groups. This actuator grouping was most effective because of the trade-off between the number of control outputs and the speed at which these outputs could be generated by the digital control computer. The three groups were formed by first pairing each of the piezoceramics on opposite sides of the neutral axis, thus creating individual bending actuator pairs. One actuator group was then formed from the five actuator pairs nearest the leading edge of the lifting surface (u_1). The second group was comprised of the five actuator pairs centered at the mid-chord (u_2). The third group was made up of the five actuator pairs near the trailing edge (u_3). This arrangement was then used in all subsequent control designs. All three of the laser displacement sensors were utilized in all the experiments performed, so that each multivariable system to be controlled had 3 inputs and 3 outputs.

6.1 LQG Cost Minimization Compensator Design

The state cost was chosen as the sum of the output $\mathbf{y}$ RMS response squared for the bench-top disturbance rejection, wind tunnel gust alleviation and wind tunnel flutter suppression experiments. Similarly, the control cost was chosen to be the sum of the control $\mathbf{u}$ RMS response squared. The total cost J was therefore

$$\begin{aligned} J &= \int_0^\infty \left[\bar{\mathbf{y}}^T\bar{\mathbf{y}} + \rho\bar{\mathbf{u}}^T\bar{\mathbf{u}}\right]dt \\ &= \int_0^\infty \left[\mathbf{x}^T\mathbf{Q}\mathbf{x} + \rho\mathbf{u}^T\mathbf{R}\mathbf{u}\right]dt \\ \mathbf{Q} &= \left[\mathbf{C}/\mathbf{y}_{max}\right]^T\left[\mathbf{C}/\mathbf{y}_{max}\right] \\ \mathbf{R} &= \mathbf{I}/\mathbf{u}_{max}^2 \end{aligned} \qquad (6.1.1)$$

where ρ is the relative state to control weighting design parameter. The scaled outputs $\bar{\mathbf{y}}$ and inputs $\bar{\mathbf{u}}$ were calculated by normalizing the physical outputs and inputs by their maximum values. The maximum outputs $\mathbf{y}_{max}$ were estimated based on the maximum expected sensor outputs caused by the disturbance sources. The largest two sigma (the signal is below this value

95 percent of the time) tip displacements measured by the laser sensors were found to be about 0.25 in. (0.635 cm) on the bench-top, caused by the magnetic shaker, and 0.75 in. (1.905 cm) in the wind tunnel, exited by the gust generator. Since the laser sensor voltage displacement constant was 0.1 V/mm, these displacements corresponded to laser sensor two sigma output voltages $\mathbf{y}_{max}$ of 0.635 V and 1.905 V for the bench-top and wind tunnel gust alleviation experiments, respectively. Note that this normalization is similar to that developed by Bryson and Ho [1969]. However in the procedure described above, the outputs are normalized by the maximum expected open loop values, rather than the desired closed loop values, to account for the different disturbance sources (bench-top shaker versus wind tunnel gust generator) in a consistent manner.

During the wind tunnel flutter experiments, the gust vanes had to be removed because of instabilities found in the individual vanes at speeds lower than the modified-for-flutter aluminum plate flutter speed. Therefore, the disturbance was provided only by the turbulence in the free stream flow. The turbulence excited the modified-for-flutter test article and was found to caused a two sigma laser sensor outputs of about 1.0 V at 80 mph. The measured maximum output was used to estimate an equivalent sinusoidal gust amplitude capable of producing the same sensor outputs. This value was found to be 0.02 degrees, and the sensor outputs measured at 80 mph were used to normalize the flutter suppression test (90 mph) sensor outputs.

The maximum control inputs $\mathbf{u}_{max}$ were taken to be those which could be generated by the control computer (±10 V), since the amplifier gains (fixed at 20 to generate a maximum of ±200 V) were already included in the system model. This normalization procedure increased the mathematical robustness of the control design calculations and facilitated inputs which were measurable (±10 Volts) and outputs which were commandable (±10 V) by the digital control computer. With the maximum values fixed, the control weight ρ was the only remaining free parameter in the LQR design process.

The Kalman filter half of the problem was set up by defining disturbance and sensor noise covariance matrices based on laboratory measurements of the disturbance source intensities and the accuracy of the laser displacement sensors. Such measurements are useful starting points

for determining the intensities of the disturbance and measurement noise covariance matrices. However, in reality the intensities of these stochastic processes, which do not actually have zero means or white frequency distributions, are not known. Thus, these intensity matrices are actually used as design tools in a manner similar to the control weighting ρ. In this study, the disturbance intensity was normalized by its maximum value and fixed at unity since the disturbance signal used in the experiments was always the maximum value.

The measurement noise was computed based on the laser sensor accuracy (180 μm) and the two sigma sensor output $\mathbf{y}_{max}$ values. The normalized measurement noise was calculated from the following formula which correctly accounts for the digitization error of the sensors [Rabiner and Schafer, 1978]

$$\text{Noise}\% = \frac{1}{\sqrt{3}} \frac{180 \times 10^{-6}}{\mathbf{y}_{max}} (100) \tag{6.1.2}$$

This normalized value was found to be 1.64 percent for the bench-top experiments. For the wind tunnel gust alleviation experiments the measurement noise was found to be 0.56 percent, three times lower than on the bench-top because of the larger disturbance source intensity produced by the gust generator. The measurement noise was estimated to be the larger value of 1.00 percent for flutter tests, since the gust generator could not be used and the only disturbance source was the free stream turbulence. From these values of measurement noise, the covariance matrices needed for the LQG design procedure could be generated. However, in order to provide stability robustness to un-modeled and mis-modeled plant dynamics, the intensity of the measurement noise was assumed to be roughly double the value calculated using Eq. 6.1.2. Further, the measurement noise was assumed to vary from this nominal value. Thus, the measurement noise was actually used as a free parameter in the Kalman filter design.

Standard routines in the Matlab Robust-Control Toolbox (Mathworks, Inc., 1988) are used to solve for the filter gain $\mathbf{K}$, compensator dynamics $\mathbf{A}_c$ and output gain $\mathbf{F}$ which make up the LQG compensator. In state space form the compensator can be written in terms of the error $\mathbf{e}$ and control signal $\mathbf{u}$

$$\dot{\hat{\mathbf{x}}} = \mathbf{A}_c\hat{\mathbf{x}} + \mathbf{K}\mathbf{e} \qquad \mathbf{u} = \mathbf{F}\hat{\mathbf{x}} \tag{6.1.3}$$

where the error signal **e** is equal to the command $\mathbf{r}_c$ minus the sum of the output **y** and the measurement noise Θ. The model based compensator dynamics are described by

$$\mathbf{A}_c = \mathbf{A} - \mathbf{B}\mathbf{F} - \mathbf{K}\mathbf{C} + \mathbf{K}\mathbf{D}\mathbf{F} \tag{6.1.4}$$

where the feed through term **D** results from the model order reduction procedure described in section 5.5.

6.2 LQG-LTR Frequency Domain Compensator Design

Desired command following performance is usually specified in the frequency domain by the sensitivity (disturbance to error signal) transfer functions or singular values. Typically the transfer functions or singular values are required to be below some value (determined by the largest acceptable error) over a particular bandwidth (set by the speed of response needed). One way such frequency domain specifications may be imposed within the LQG compensator design framework is by the loop transfer recovery (LTR) method [Stein and Athens, 1987]. The LQG-LTR method manipulates the matrices defining the LQG cost functions so that a limited number of frequency domain specifications may be imposed.

The LTR method was used to design compensators for the wind tunnel command following experiments. In theory, the LTR procedure consists of three basic steps: Augment integrators to the plant, design the Kalman filter loop, and increase the control gain (decrease the control weight) until the filter loop is recovered. However, some modifications to this procedure were needed to actually use LTR for active lifting surface command following. First, it was necessary to move the added integrator poles away from the origin to prevent quasi-steady actuator saturation. Thus, the integrators became low frequency quasi-integrator poles which set the low frequency command following limit. Second, the upper frequency limit, or command following bandwidth, was determined by the ability to "recover the loop" rather than the design of the Kalman filter loop. Loop recovery is difficult at best and impossible for plants with non-minimum phase zeros because plant inversion is required (the plant dynamics are canceled by the compensator

dynamics). This makes high frequency command following extremely difficult, since achieving good command following requires recovery (and therefore an extremely accurate model) at least a decade above the command following bandwidth. The "dubious" aspects of plant inversion and other problems associated with LTR are discussed by Stein and Doyle [1991].

Two sets of compensators were designed for the active lifting surface command following tests. A set of low frequency compensators were designed for quasi-steady and very low frequency command following with a quasi-integrator low frequency pole set to 1.0 Hz. And, a set of high frequency compensators were designed for mid-range frequency command following with a quasi-integrator pole at 5.0 Hz. In each set, the Kalman filter loop was designed to match all singular values over the command following bandwidth, which extended from the quasi-integrator poles to the designed cross-over frequency. The filter loop was designed to be equal to $\mu \mathbf{I}/s$ in order to obtain large low frequency gain (for performance) and small high frequency gain (for stability robustness). The sensor noise, equal to $1/\mu$, was used to set the cross-over frequency for each compensator design.

6.3 Controller Order Reduction

To facilitate implementation on the real time control computer, model based compensators found from the design models (22, 32 and 34 states) were reduced to 14 states using the ordered Hankel singular value procedure described previously. As an alternate design procedure, reduced 14 state compensators were computed directly from the design model using a fixed architecture optimal projection gradient search technique [Mercedal, 1991]. Optimal projection designs differ from the two step (design and reduce) process in that the compensators are designed to a specific model order with the knowledge of the model order incorporated in the design equations. The optimal projection compensators were compared to the reduced order LQG compensators in the aluminum test article bench-top experiments so that the effect of ad-hoc compensator reduction could be assessed.

Finally, the reduced order continuous time compensators were transformed to the discrete time domain via a Tustin transform. The sampling rate was chosen to be 2000 Hz, which provided adequate frequency

resolution in the desired control bandwidth (about 200 Hz). This rate was found to be the practical limit of the control computer used to implement these three-input, three-output, fourteen state digital compensators. The actual delay of the digital control computer was measured at roughly one sample period, two times the delay normally associated with a zero order hold [Franklin and Powell, 1980].

The equations describing the reduced order LQG or optimally projected compensators can be expressed in state space

$$\dot{\hat{\mathbf{x}}} = \mathbf{A}_{cc}\hat{\mathbf{x}} + \mathbf{K}_c\mathbf{e} \qquad \mathbf{u} = \mathbf{F}_c\hat{\mathbf{x}} + \mathbf{D}_c\mathbf{e} \tag{6.3.1}$$

or transfer function form

$$\mathbf{u} = \mathbf{K}(s)\mathbf{e} \qquad \mathbf{K}(s) = \mathbf{F}_c(s\mathbf{I} - \mathbf{A}_{cc})^{-1}\mathbf{K}_c + \mathbf{D}_c \tag{6.3.2}$$

where $\mathbf{A}_{cc}$ contains the reduced order compensator dynamics and $\mathbf{D}_c$ is a compensator feed through term which results from the reduction process. Note that the additional subscript "c" differentiates the reduced order compensators (Eqs. 6.3.1 and 6.3.2) from the original designs (Eqs. 6.1.3 and 6.1.4).

In the design of dynamic compensators, the loop transfer function $\mathbf{T}(s)$ plays an important role. This transfer function shows the relative control authority being exerted and the potential for driving the system unstable, which depends on the magnitude relative to unity for MIMO systems and the gain margin for SISO systems. The loop transfer function, measured from the compensator error inputs to the plant sensor outputs, is found from the compensator (Eq. 6.3.2) and plant control (Eq. 5.3.2) transfer functions

$$\mathbf{y} = \mathbf{T}(s)\mathbf{e} \qquad \text{where } \mathbf{T}(s) = \mathbf{G}_c(s)\mathbf{K}(s) \tag{6.3.3}$$

The compensator and resulting loop transfer functions are detailed below for the various bench-top and wind tunnel tests performed.

6.4 Compensator Design Details

For the bench-top disturbance, wind tunnel gust alleviation and wind tunnel flutter suppression tests, control laws were designed to minimize the cost made up of the sensor outputs and control inputs as described above.

The state cost evenly weighted each sensor output, while the control cost weighted the control inputs by the total piezoceramic actuator area of each control group. Compensators were designed from the design models for relative state to control cost weights ρ ranging from 10^{+4} to 10^{-4}. Compensators were designed for control weighting increments of 10, so that a series of 9 controllers were designed for each assumed sensor noise value. The command following controllers, which were designed using the LTR method, were computed for relative control weights of 1.0 to 10^{-8} in the hopes of achieving true filter loop recovery. These compensators were also designed for control weighting increments of 10 to obtain a series of 9 controllers.

Bench-Top Disturbance Rejection Compensator Details

Compensators were designed from the 22 state design models for the aluminum and G/E bench-top test articles using sensor noise estimates of 1, 3 and 6 percent. Figs. 6.1 and 6.2 display the compensator $\mathbf{K}(s)$ and the loop $\mathbf{T}(s)$ transfer function singular values of the G/E bench-top test article compensators designed with a sensor noise estimate of 3 percent. Fig. 6.1 plots the singular values of a low gain ($\rho = 1.0$) compensator design and Fig. 6.2 displays the singular values of a high gain ($\rho = 10^{-2}$) design. A significant increase in gain is observed between the two designs. Note that in each design the compensator gain begins rolling-off at about 120 Hz (the actual control bandwidth), and notching is observed in the roll-off region. Moreover, observe the increased notching of the high gain compensator.

Wind Tunnel Gust Alleviation Compensator Details

The wind tunnel gust alleviation compensators were designed from the 32 and 34 state design models using sensor noise estimates of 0.5, 1.0 and 2.0 percent for the aluminum and G/E lifting surface, respectively. Fig. 6.3 plots the compensator $\mathbf{K}(s)$ and loop $\mathbf{T}(s)$ maximum singular values of a low gain ($\rho = 1.0$) compensator design and Fig. 6.4 displays the singular values of a high gain ($\rho = 10^{-1}$) design for the G/E lifting surface with a sensor noise of 1.0 percent. The figures show the increased low frequency control authority and the decreased actual control bandwidth (about 80 Hz) of these gust alleviation compensators relative to the bench-top compensators. As before,

significant notching occurs in the roll-off region for these gust alleviation controllers.

Wind Tunnel Command Following Compensator Details

Figs. 6.5 and 6.6 show the compensator and loop transfer function maximum singular values of a low frequency and high frequency command following compensator designed for the G/E lifting surface, respectively. The low frequency command following compensators were designed so that the loop transfer functions would cross over at about 80 Hz. The best performing stable low frequency command following compensator was designed with a control weight ρ of 10^{-4}. This compensator was only able to recover the desired filter loop ($\mu I/s$) enough to yield a cross-over frequency of about 10 Hz, as shown in Fig. 6.5. The high frequency compensators were designed for a loop cross-over of roughly 160 Hz. The best performing stable high frequency command following compensator was designed with a control weight ρ of 10^{-6}. As with the low frequency design, even this very low control weight was not sufficient to properly recover the loop of this higher bandwidth compensator. As seen in Fig 6.6, cross-over is only at about 50 Hz. The figures also show the large low frequency gain of these compensators and the quasi-integrator poles which limit the very low frequency gain so that quasi-steady actuator saturation is avoided. Finally observe that command following performance was not limited by the low cross-over frequency of the desired filter loops (80 and 160 Hz), since small modeling errors and large compensator gains prevented good loop recovery even for these modest designs.

Wind Tunnel Flutter Suppression Compensator Details

The wind tunnel flutter suppression compensators were designed from the 38 state design models using sensor noise estimates of 1.0 percent for the modified-for-flutter aluminum lifting surface. Fig. 6.7 plots the compensator maximum singular values for a medium gain (ρ = 1.0) flutter suppression compensator. The singular values show control being applied to the first two flexible modes, which coalesce in the open loop causing flutter. The compensator then rolls off through the higher frequency modes. Notice that this controller also exhibits high gain at low frequencies and notching in the roll-off region.

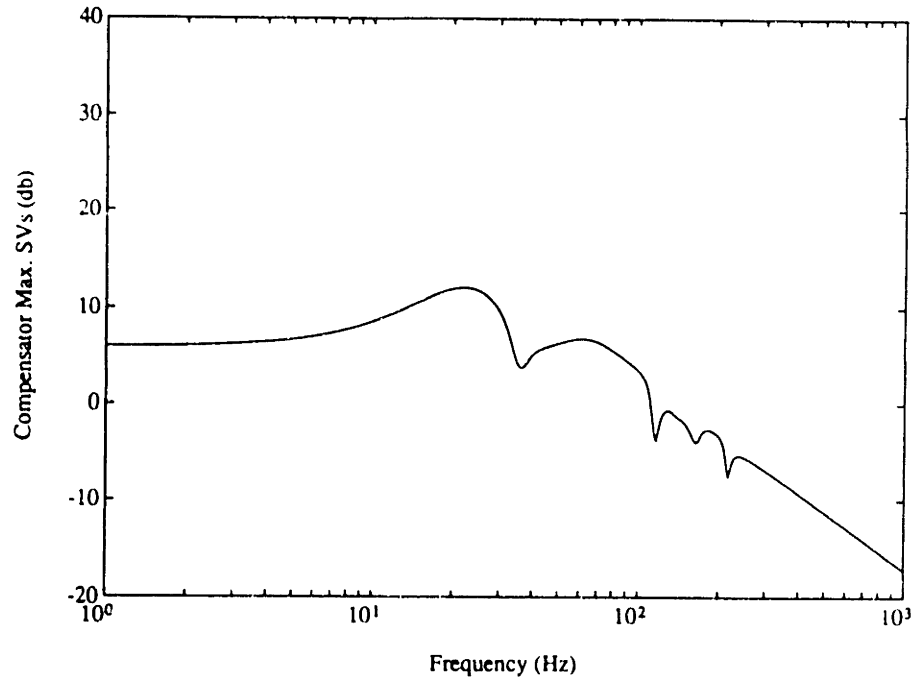

Figure 6.1a. Maximum singular values of a low gain compensator K(s) transfer function matrix for the G/E test article on the bench-top.

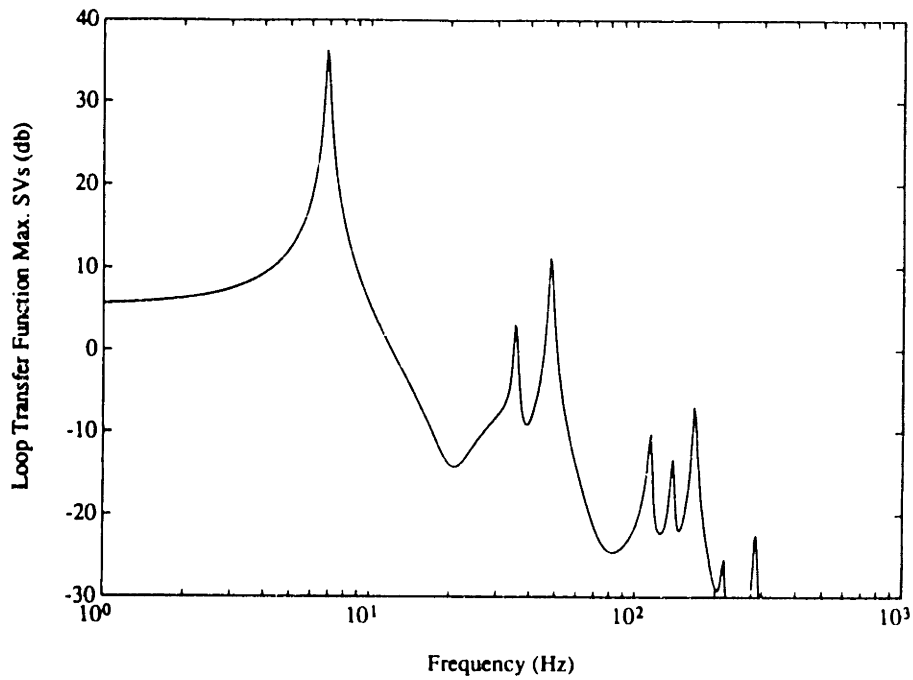

Figure 6.1b. Maximum singular values of the loop T(s) transfer function associated with the low gain compensator for the G/E test article on the bench-top.

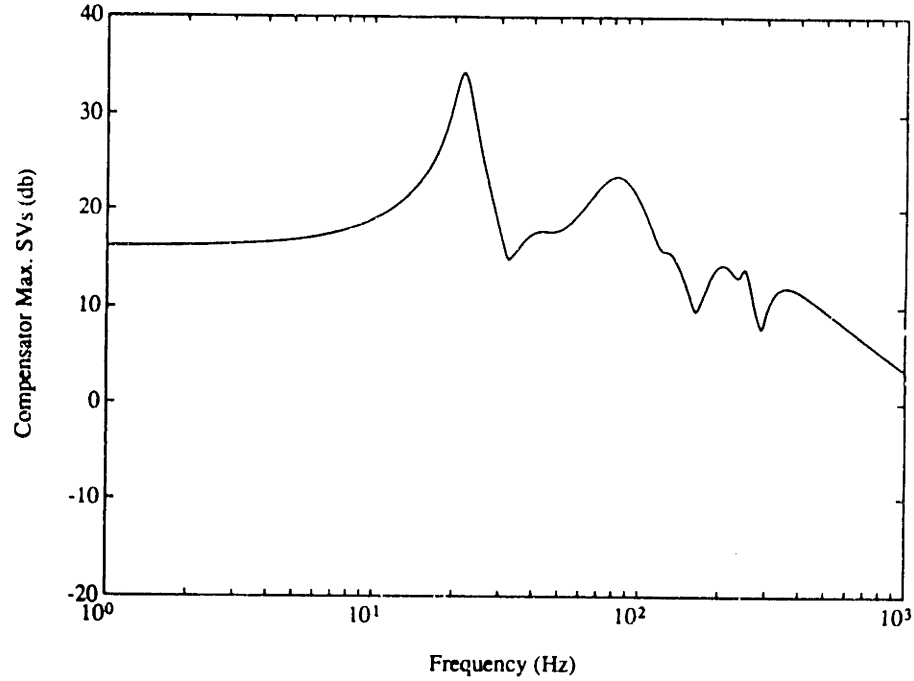

Figure 6.2a. Maximum singular values of a high gain compensator K(s) transfer function matrix for the G/E test article on the bench-top.

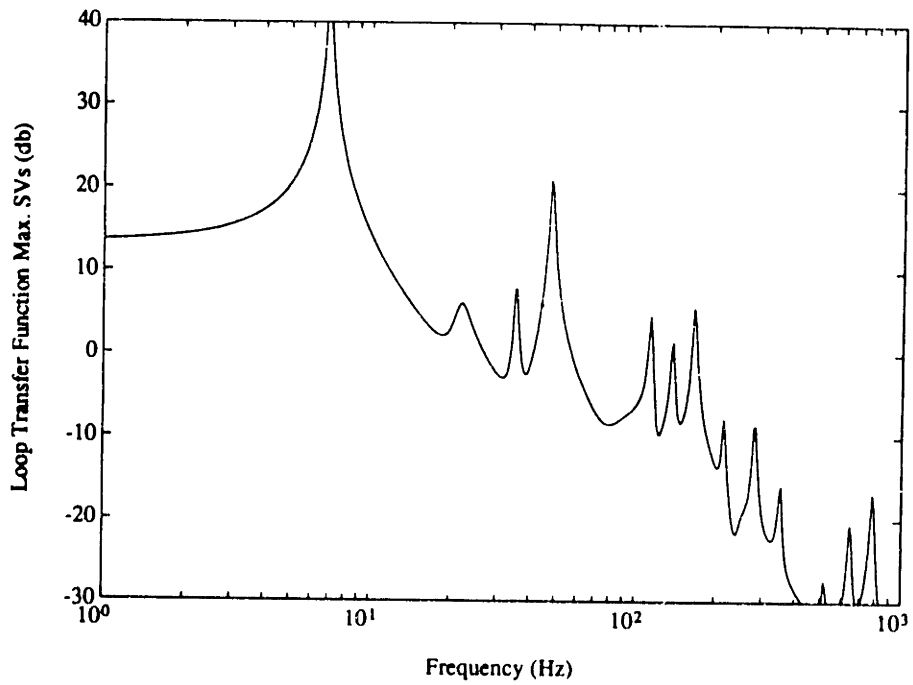

Figure 6.2b. Maximum singular values of the loop T(s) transfer function associated with the high gain compensator for the G/E test article on the bench-top.

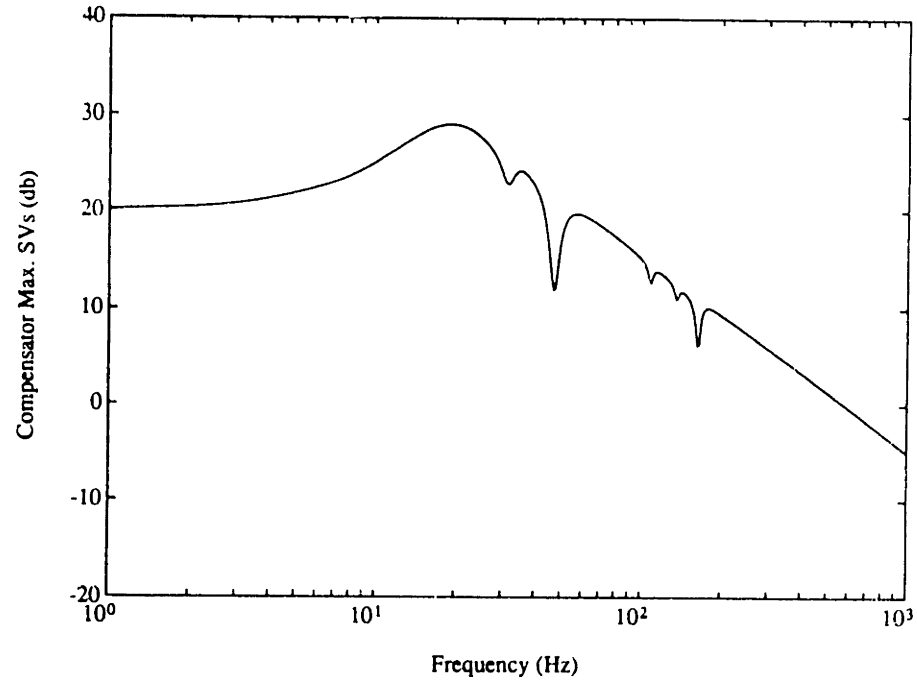

Figure 6.3a. Maximum singular values of a low gain compensator K(s) transfer function matrix for the G/E lifting surface in the wind tunnel.

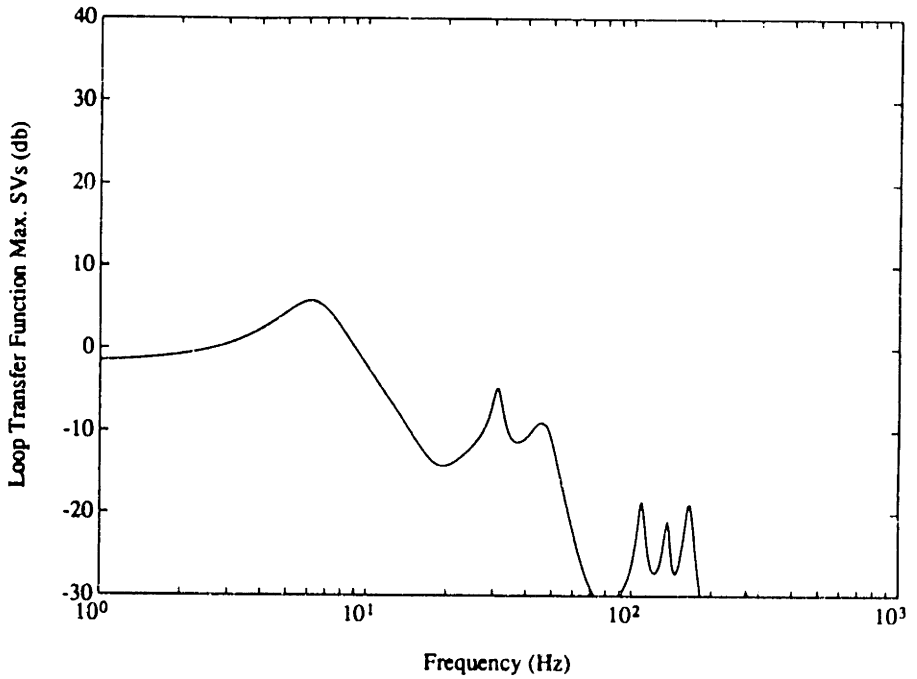

Figure 6.3b. Maximum singular values of the loop T(s) transfer function associated with the low gain compensator for the G/E lifting surface in the wind tunnel.

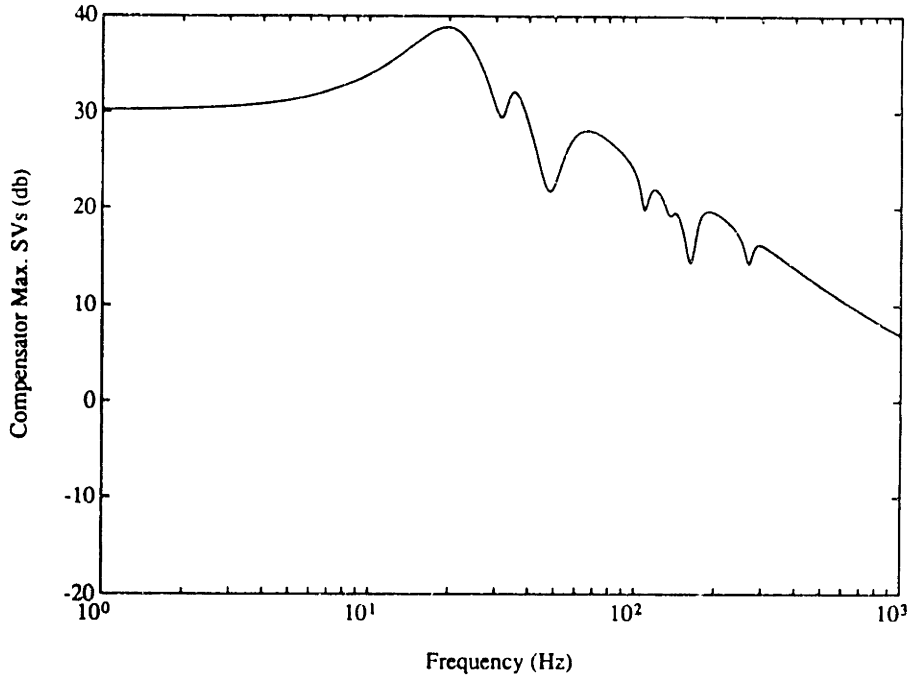

Figure 6.4a. Maximum singular values of a high gain compensator K(s) transfer function matrix for the G/E lifting surface in the wind tunnel.

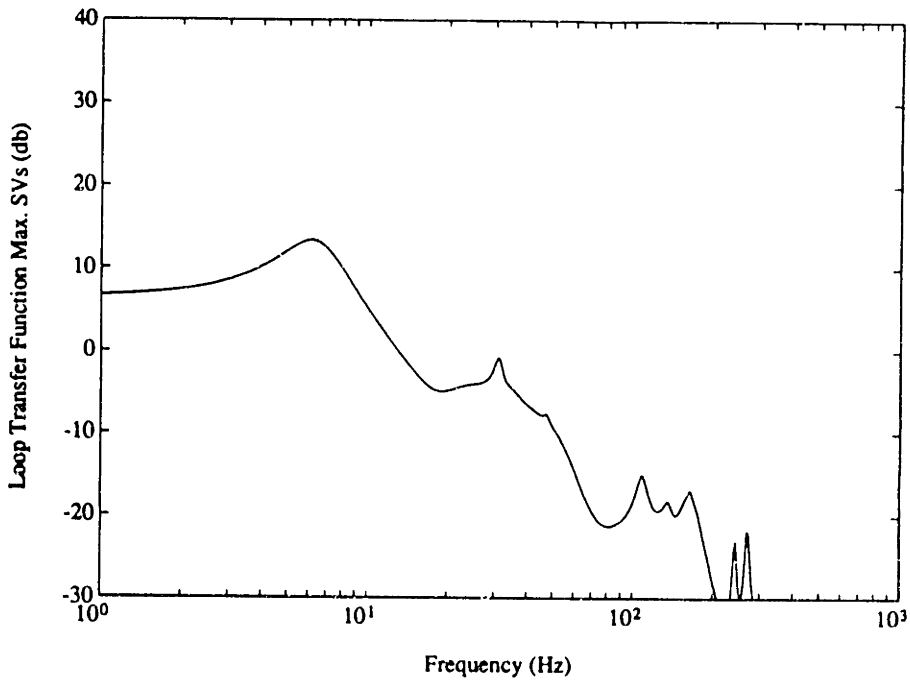

Figure 6.4b. Maximum singular values of the loop T(s) transfer function associated with the high gain compensator for the G/E lifting surface in the wind tunnel.

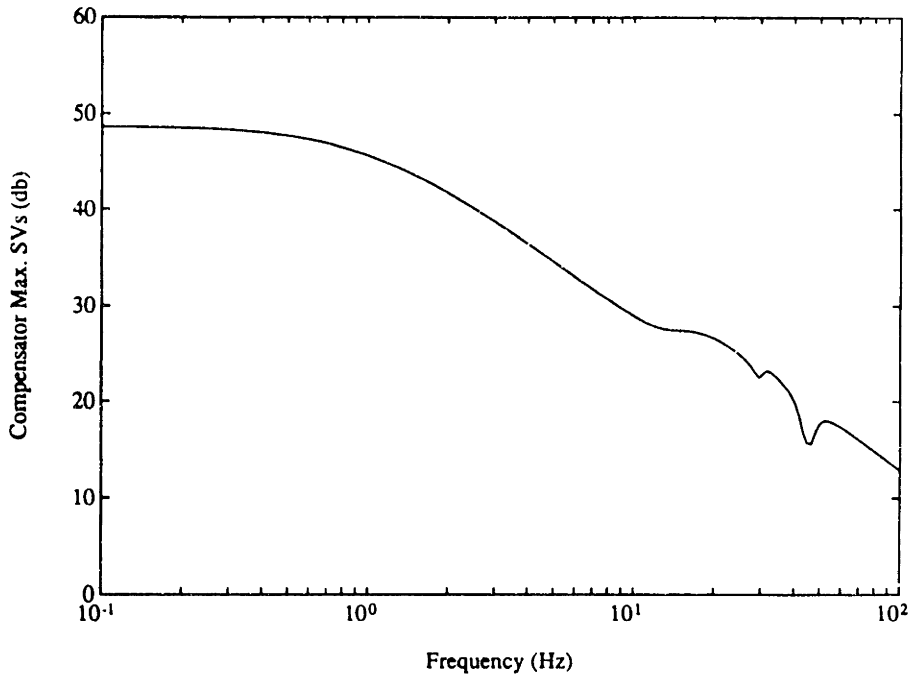

Figure 6.5a. Maximum singular values of a low frequency command following compensator K(s) transfer function matrix for the G/E lifting surface in the wind tunnel.

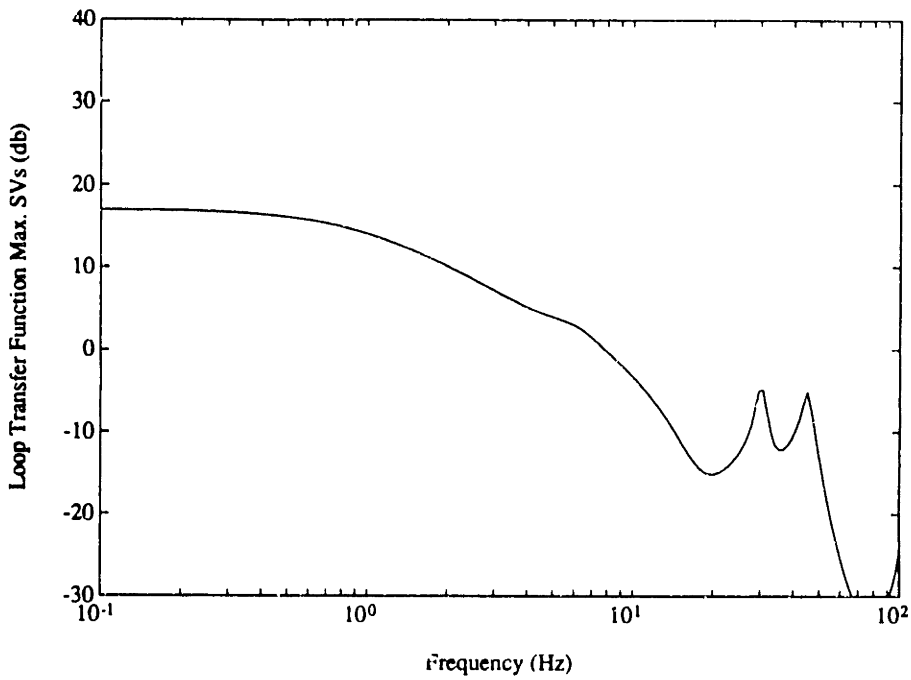

Figure 6.5b. Maximum singular values of the loop T(s) transfer function associated with the low frequency command following compensator for the G/E lifting surface in the wind tunnel.

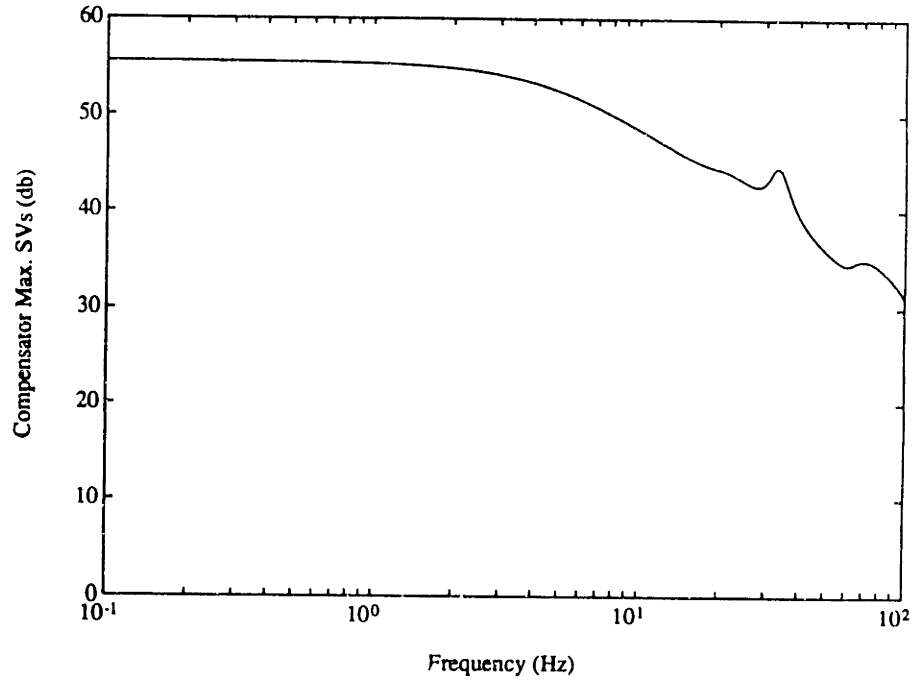

Figure 6.6a. Maximum singular values of a high frequency command following compensator K(s) transfer function matrix for the G/E lifting surface in the wind tunnel.

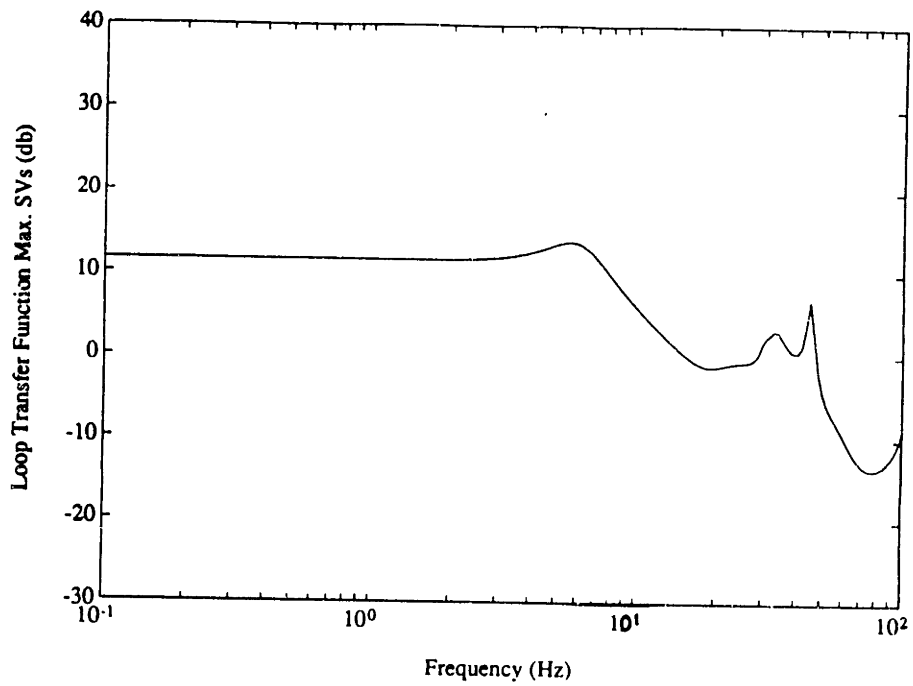

Figure 6.6b. Maximum singular values of the loop T(s) transfer function associated with the high frequency command following compensator for the G/E lifting surface in the wind tunnel.

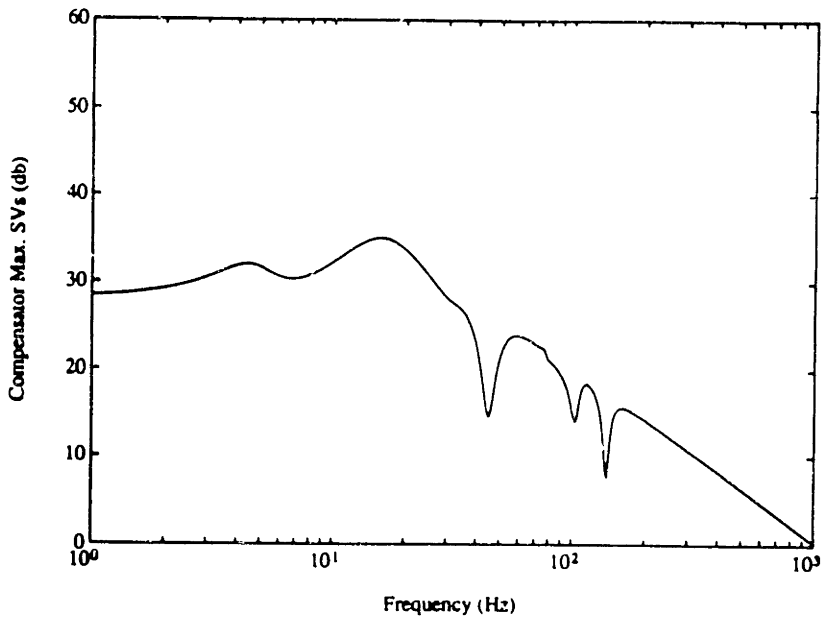

Figure 6.7. Singular values of a high gain flutter suppression compensator K(s) for the modified-for-flutter aluminum test article.

Chapter 7. Bench Experiment

Although the ultimate objective of this study is aeroelastic control, it is desirable to first demonstrate that multivariable compensators can be designed and implemented to control the active test articles in a bench-top setting. Before closed loop wind tunnel testing, it is important to check as much of the analytical model as possible, verifying the control law design procedure and acquire needed control law design experience. Further it is essential to check the functionality of the digital control computer, power amplifiers and other associated hardware. These tasks are much easier to accomplish in a laboratory bench-top setting than in the wind tunnel where aerodynamic forces introduce additional complications and time constraints are severe.

The bench-top experiments are also important because of the high-bandwidth nature of the bench-top disturbance source, which enables the demonstration of high-authority and high-bandwidth disturbance attenuation. Therefore, another goal of the closed loop bench-top experiments is to show the ability of distributed strain actuators and multivariable compensators to control the quasi-steady lifting surface response as well as add significant amounts of damping to several structural modes in the control bandwidth.

7.1 Closed Loop System Evaluation Criteria

The compensators were evaluated analytically for stability and performance using the 73 state evaluation model (the full order model without aerodynamics). The ability of the compensators designed to control the active test articles was determined from numerical simulation and closed loop bench-top testing in three different experiments. First, performance was evaluated by comparing the experimentally measured and analytically predicted closed loop disturbance attenuation to the open loop output $\mathbf{G}_d(s)$, described by Eq. 5.3.2. The closed loop response was calculated using a state space representation of the reduced order compensator and full order evaluation model.

$$\begin{bmatrix} \dot{\mathbf{x}} \\ \dot{\hat{\mathbf{x}}} \end{bmatrix} = \begin{bmatrix} \mathbf{A} - \mathbf{B}\mathbf{D}_c\mathbf{C} & -\mathbf{B}\mathbf{F}_c \\ \mathbf{K}_c\mathbf{C} & \mathbf{A}_{cc} \end{bmatrix} \begin{bmatrix} \mathbf{x} \\ \hat{\mathbf{x}} \end{bmatrix} + \begin{bmatrix} \mathbf{L} \\ \mathbf{0} \end{bmatrix} \mathbf{d}$$

$$\mathbf{y} = [\mathbf{C} \quad \mathbf{0}] \begin{bmatrix} \mathbf{x} \\ \hat{\mathbf{x}} \end{bmatrix} \tag{7.1.1}$$

Second, the performance obtained was evaluated in terms of the greatest disturbance attenuation achieved before encountering instabilities, by examining the stability robustness of the systems. Stability robustness measures how near to instability particular controllers are, and the likelihood of driving the system unstable by increasing the control gain. The stability robustness is measured by comparing the closed loop and inverse error maximum singular values. In this study, a modified stability robustness criteria is developed which is shown to be significantly better at predicting stability boundaries for lightly damped flexible structures than the usual methods.

Third, performance was further assessed by comparing the experimentally measured and analytically predicted state versus control cost of each controller. The closed loop state cost is directly related to the RMS response of the outputs and measures the performance of each control design. Similarly, the control cost is directly related to the RMS response of the control inputs and is a measure of the amount of control used. By solving the Lyapunov equation associated with the closed loop system

$$\begin{bmatrix} \dot{\mathbf{x}} \\ \dot{\hat{\mathbf{x}}} \end{bmatrix} = \begin{bmatrix} \mathbf{A} - \mathbf{B}\mathbf{D}_c\mathbf{C} & -\mathbf{B}\mathbf{F}_c \\ \mathbf{K}_c\mathbf{C} & \mathbf{A}_{cc} \end{bmatrix} \begin{bmatrix} \mathbf{x} \\ \hat{\mathbf{x}} \end{bmatrix} + \begin{bmatrix} \mathbf{L} & -\mathbf{B}\mathbf{D}_c \\ \mathbf{0} & \mathbf{K}_c \end{bmatrix} \begin{bmatrix} \mathbf{d} \\ \Theta \end{bmatrix} \tag{7.1.2}$$

the state and control costs can be found directly from the covariance matrices.

$$\text{State Cost} = \text{Trace}\left(\mathbf{Q}E\left[\mathbf{x}\mathbf{x}^T\right]\right)$$

$$\text{Control Cost} = \frac{1}{\rho}\text{Trace}\left(\mathbf{G}\mathbf{R}^{-1}\mathbf{G}^T E\left[\hat{\mathbf{x}}\hat{\mathbf{x}}^T\right]\right) \tag{7.1.3}$$

Note that the experimental RMS values were calculated by integrating the frequency responce over the 500 Hz evaluation bandwidth.

7.2 Performance Results

The frequency response of the open versus closed loop analytical and experimental disturbance to leading edge sensor ($y_1/\mathbf{d}$) transfer functions are displayed in Figs. 7.1 and 7.2 for the aluminum and G/E test articles, respectively. Notice the good agreement between the analytic model and the experimental results, verifying the ability of the Ritz model to correctly predict the steady state magnitudes, poles, zeros, and lags of the dynamic systems. The agreement between the model and the experiment also indicates that the dynamics of the other system components (such as sensor roll-off and filter dynamics) were modeled correctly. Further, the excellent closed loop performance validates the compensator design, order reduction and digital implementation methods utilized.

Figs. 7.1 and 7.2, which display the tip displacement due to a broadband (500 Hz) excitation from the magnetic probe, illustrate the high-authority, large-bandwidth nature of these controller designs. Significant amounts of damping were introduced into the first four structural modes by these control designs ($\rho = 10^{-2}$) without destabilizing any high frequency modes. For both test articles the magnitude of the closed loop frequency response was reduced from that of the open loop system (which had an estimated 1.5 percent structural damping in each mode) by approximately 30, 10, 20, and 10 db in the first four modes, respectively. Comparison of Figs. 7.1 and 7.2 shows the increased torsional (2^{nd} and 4^{th} modes) control authority of the bending/twist coupled G/E plate, however the ability of the bend/twist coupled G/E plate to effect additional torsional control was not as pronounced as expected in the bench-top tests.

Figs. 7.1 and 7.2 clearly illustrate the high-authority nature of the compensator designs. In addition to significantly reducing the steady state response (by approximately 10 db), the controllers are able to completely eliminating the resonant behavior of first structural mode in both test articles. These results demonstrate that strain actuation, which provides direct control of the strain in the structure, can be used to implement high-authority control designs.

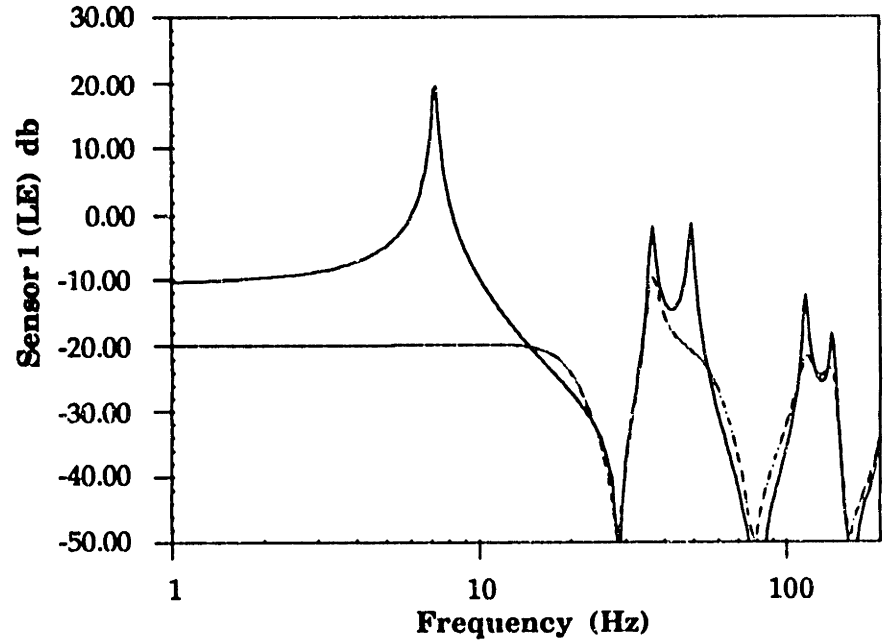

Figure 7.1a. Analytical open and closed loop frequency response of the aluminum test article for a LQG disturbance rejection compensator designed with $\rho = 10^{-2}$ and the sensor noise estimated at 3%.

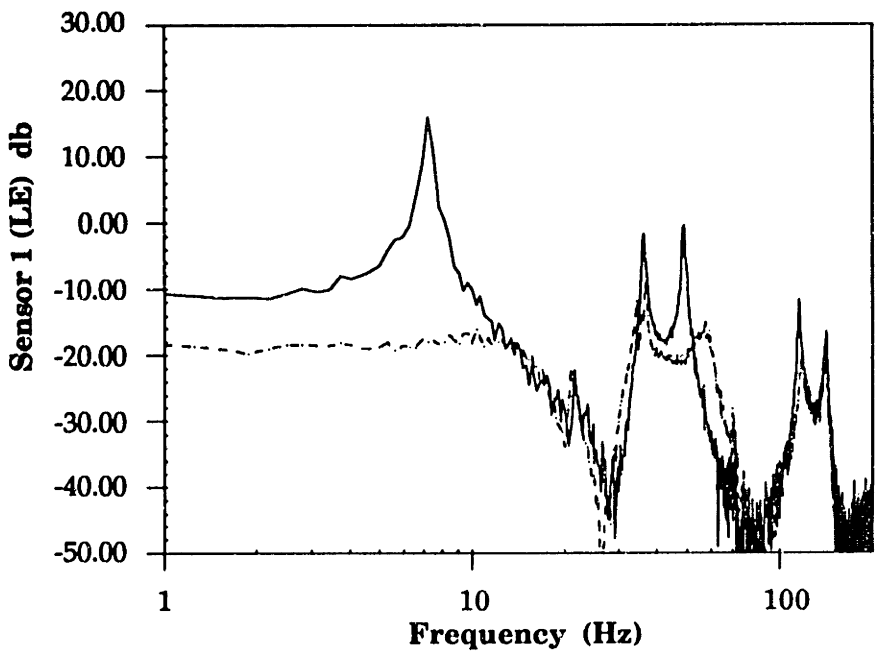

Figure 7.1b. Experimental open and closed loop frequency response of the aluminum test article for a LQG disturbance rejection compensator designed with $\rho = 10^{-2}$ and the sensor noise estimated at 3%.

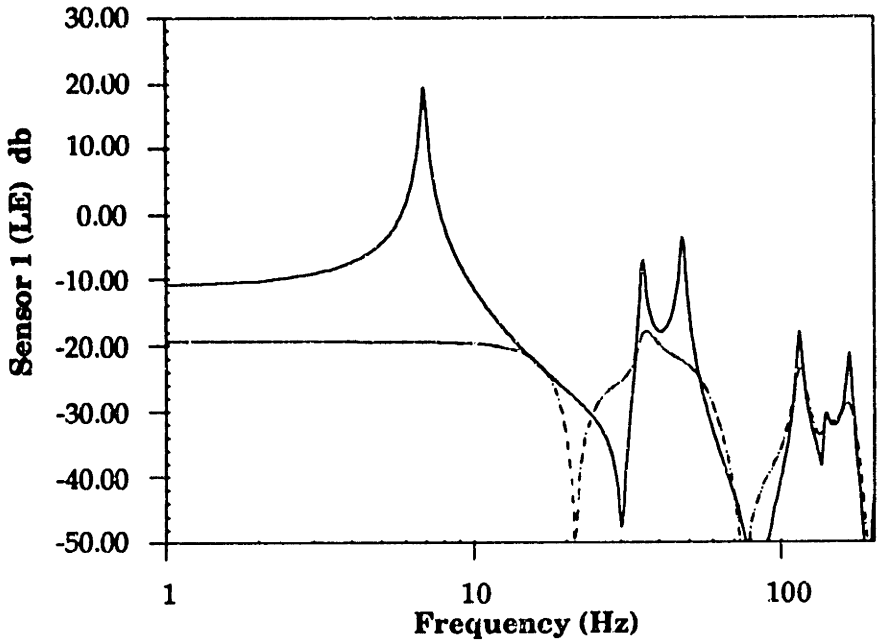

Figure 7.2a. Analytical open and closed loop frequency response of the G/E test article for a LQG disturbance rejection compensator designed with $\rho = 10^{-2}$ and the sensor noise estimated at 3%.

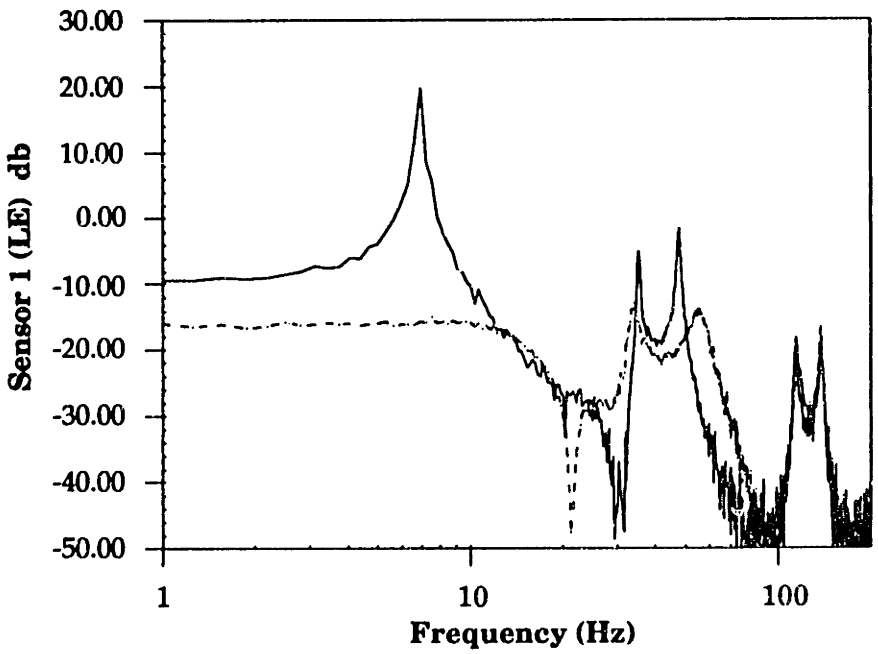

Figure 7.2b Experimental open and closed loop frequency response of the G/E test article for a LQG disturbance rejection compensator designed with $\rho = 10^{-2}$ and the sensor noise estimated at 3%.

7.3 Stability Robustness

Transfer functions such as those in Figs 7.1 and 7.2 show the ability of strain actuation to effect significant amounts of disturbance attenuation, but offer no information with regard to the amount of control authority used or the amount which can be applied to the system before errors in the analytic model cause instabilities. Therefore, a stability robustness test is needed which can predict the control authority which can be successfully applied to the system. Unfortunately, most currently employed stability robustness test are overly conservative for lightly damped flexible structures. One of the more common stability robustness tests employed [Lehtomaki, *et. al.*, 1984] requires the maximum singular values of the closed loop transfer function $\sigma_{max}[\mathbf{C}(s)]$ to be less than the reciprocal of the maximum singular values of the multiplicative model error $1/\sigma_{max}[\Delta(s)]$ acting at the plant output

$$\sigma_{max}[\mathbf{C}(s)] < \frac{1}{\sigma_{max}[\Delta(s)]}$$

$$\mathbf{C}(s) = [\mathbf{I} + \mathbf{T}(s)]^{-1}\mathbf{T}(s)$$

$$\Delta(s) = \left[\mathbf{G}_c(s)_{exp} - \mathbf{G}_c(s)\right]\mathbf{G}_c(s)^{-1}$$

$$\text{where} \qquad \mathbf{T}(s) = \mathbf{G}_c(s)\mathbf{K}(s) \tag{7.3.1}$$

where T(s) is the loop transfer function (Eq. 6.3.3), with the loop broken at the sensor outputs. The stability robustness test of Eq. 7.3.1 assumes all model errors are reflected at the plant output, as opposed to several other possibilities [Doyle, Wall and Stein, 1982]. The actual model error is computed using the evaluation model calculated $\mathbf{G}_c(s)$ and experimentally measured $\mathbf{G}_c(s)_{exp}$ control transfer functions (Eq. 5.3.2). Note that this robustness test guarantees stability.

Unfortunately, this method yields overly large error maximum singular values and an extremely conservative stability robustness test. The conservatism of this nominal test is illustrated in Fig. 7.3 which shows the maximum singular values of the closed loop control transfer function $\sigma_{max}[\mathbf{C}(s)]$ and the inverse error matrix $1/\sigma_{max}[\Delta(s)]$ for the aluminum test article. Notice that the test is violated (predicting instabilities) over the entire evaluation bandwidth for a compensator designed with a control

weighting $\rho = 1$, two orders of magnitude greater (resulting in much lower control gains) than that of the stable high-performance compensator depicted in Fig. 7.1. Obviously this nominal test is very conservative, and not a useful tool for predicting the amount of control effort which can be utilized before instabilities are encountered.

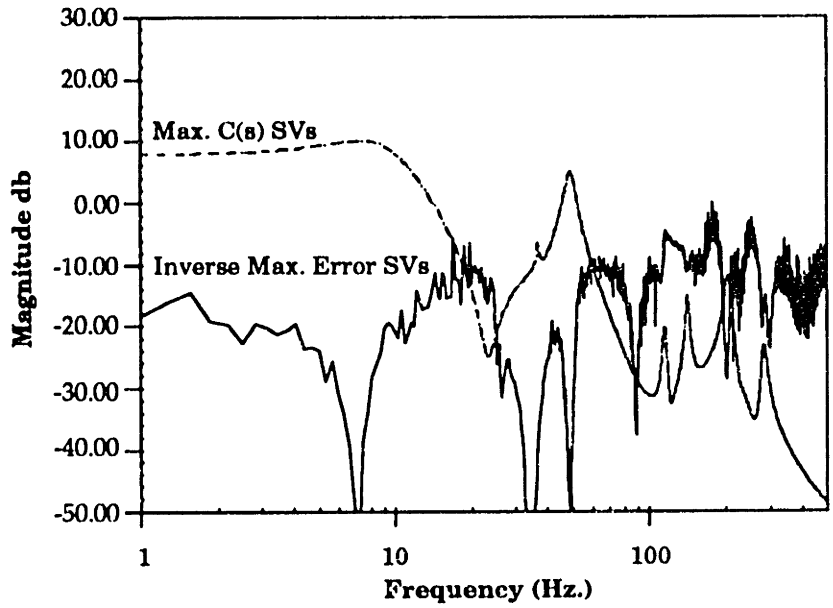

Figure 7.3. Bench-top closed loop C(s) maximum singular values and the reciprocal of the error Δ(s) maximum singular value for the aluminum plate with a LQG compensator designed with $\rho = 1$ and the sensor noise estimated at 3%. The plot shows the inability of the nominal robustness test to predict stability.

Motivated by the deficiencies of this nominal method, a new stability robustness test was developed in order to provide a more realistic estimate of the maximum control effort which can be utilized before such instabilities occur. This test is derived from the small gain theorem [Maciejowski, 1989], as is the test described above. However, rather than breaking the loop transfer function at the sensor outputs (as in Eq. 7.3.1), a singular value decomposition (SVD) is performed on the plant control transfer function, $\mathbf{G_c}(s) = \mathbf{U\Sigma V}$, and a new loop transfer function $\mathbf{T_\Sigma}$ is found by breaking the loop at the output of the plant singular values Σ. A new closed loop transfer function matrix $\mathbf{C_\Sigma}$ is then formed and compared to the error Δ_Σ, which is found from the calculated and experimentally measured singular values.

Because the error Δ_Σ is calculated from the singular values, the error matrix is made up of only diagonal terms, each of which is essentially a measure of the percent error in the particular singular value. This method disregards any difference between the analytical and experimental singular vectors collected in the unitary matrices, U(s) and V(s), in the formulation of the multiplicative error. However, since the stability robustness test is derived from the small gain theorem, which does not consider directional information, disregarding the directional information contained in the unitary matrices is considered consistent, and leads to a modified stability robustness test useful for actual controlled flexible structures.

$$\max\left[\mathbf{C}_\Sigma(s)\right] < \frac{1}{\sigma_{\max}\left[\Delta_\Sigma(s)\right]}$$

$$\mathbf{C}_\Sigma(s) = \left[\mathbf{I} + \mathbf{T}_\Sigma(s)\right]^{-1}\mathbf{T}_\Sigma(s)$$

$$\Delta_\Sigma(s) = \left[\Sigma(s)_{exp} - \Sigma(s)\right]\Sigma(s)^{-1}$$

$$\text{where} \quad \mathbf{G}_c(s) = \mathbf{U}(s)\Sigma(s)\mathbf{V}(s)$$

$$\text{and} \quad \mathbf{T}_\Sigma(s) = \mathbf{V}(s)\mathbf{K}(s)\mathbf{U}(s)\Sigma(s) \qquad (7.3.2)$$

This modified stability robustness test carries no guarantees of stability (in contrast with the nominal conservative test) but was found to be fairly accurate at predicting robustness to model errors. This new robustness test was applied to the test articles used in this study. Example results are plotted in Figs. 7.4 and 7.5 for the aluminum and G/E plates, respectively. In the region where control is being effected, the control law utilizes directional (phase) information to maintain stability even when the small gain theorem is violated. However, in the bench-top roll-off region (above 120 Hz) the compensator uses gain notching to avoid destabilizing higher modes, as shown in Fig. 7.6, and makes no use of any directional information. It is in this roll-off region that any violation of the robustness test will cause an instability. Figs 7.4 and 7.5 clearly show that the new robustness test predicts stability for the ρ=1 compensator design ($\sigma_{max}[\mathbf{C}_\Sigma(s)]$ does not penetrate through $1/\sigma_{max}[\Delta_\Sigma(s)]$ in the controller roll-off region). In contrast, the commonly employed method (Fig. 7.3) predicts that instabilities will occur ($\sigma_{max}[\mathbf{C}_\Sigma(s)]$ penetrates and extends above $1/\sigma_{max}[\Delta_\Sigma(s)]$ in the roll-off region). Note that this compensator design was found experimentally to be stable.

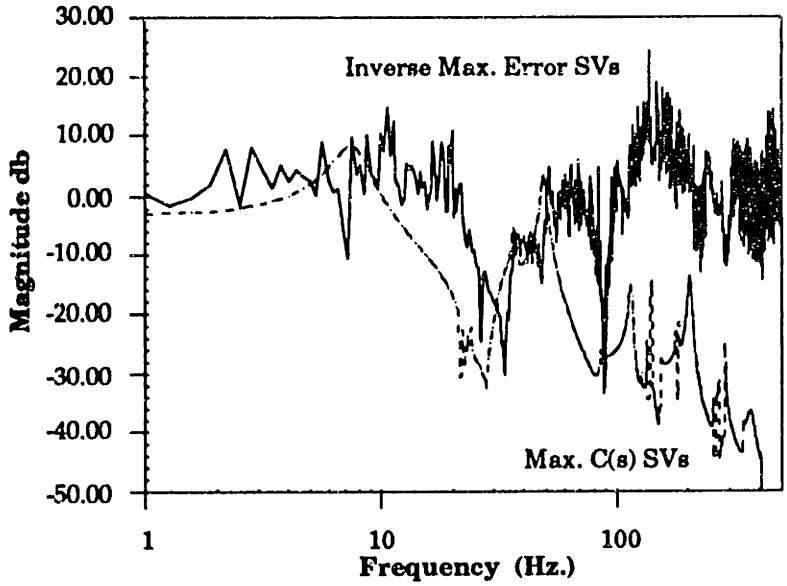

Figure 7.4a. Bench-top closed loop transfer function $C_\Sigma(s)$ maximum singular values and the reciprocal of the error $\Delta_\Sigma(s)$ maximum singular values for the aluminum plate with a LQG compensator designed with $\rho = 10^0$ and the sensor noise estimated at 3%.

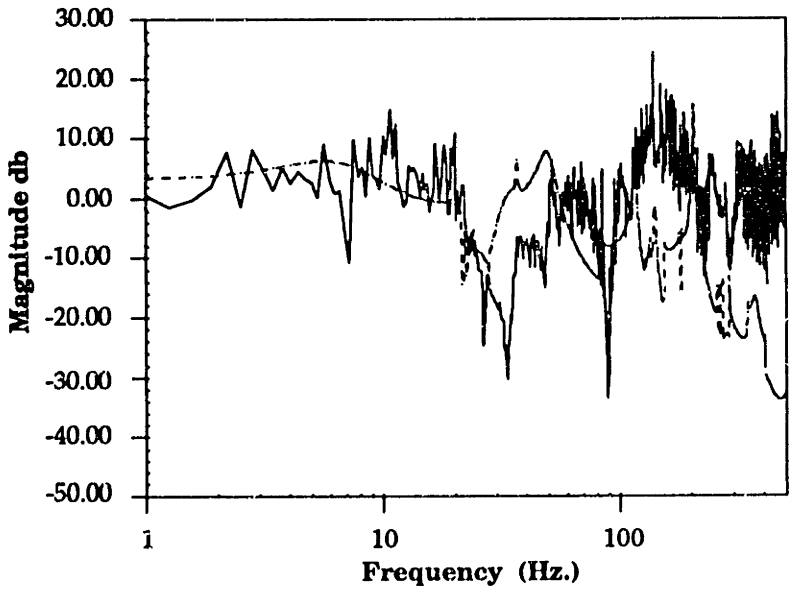

Figure 7.4b. Bench-top closed loop transfer function $C_\Sigma(s)$ maximum singular values and the reciprocal of the error $\Delta_\Sigma(s)$ maximum singular values for the aluminum plate with a LQG compensator designed with $\rho = 10^{-2}$, and the sensor noise estimated at 3%.

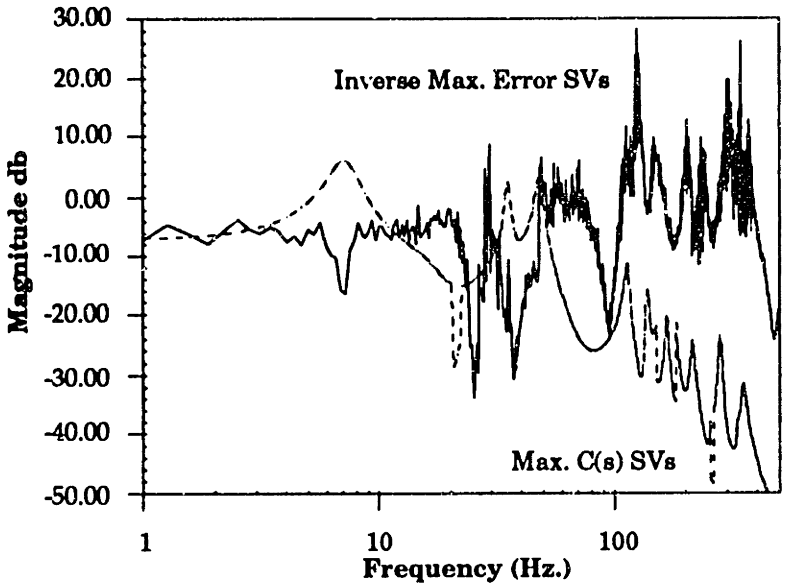

Figure 7.5a. Bench-top closed loop transfer function $C_\Sigma(s)$ maximum singular values and the reciprocal of the error $\Delta_\Sigma(s)$ maximum singular values for the G/E plate with a LQG compensator designed with $\rho = 10^0$ and the sensor noise estimated at 3%.

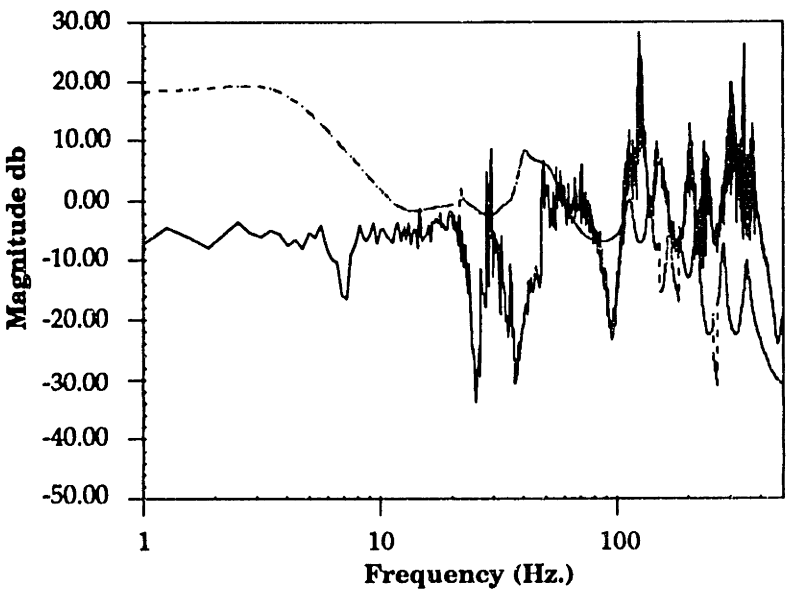

Figure 7.5b. Bench-top closed loop transfer function $C_\Sigma(s)$ maximum singular values and the reciprocal of the error $\Delta_\Sigma(s)$ maximum singular values for the G/E plate with a LQG compensator designed with $\rho = 10^{-2}$, and the sensor noise estimated at 3%.

As the relative control weighting is decreased and the control designs utilize higher gains, the maximum singular values of the closed loop transfer function $\sigma_{max}[C_{\Sigma}(s)]$ increases and moves closer to the reciprocal of the maximum singular values of the error $1/\sigma_{max}[\Delta_{\Sigma}(s)]$ in the roll-off region. The plots indicate that model errors, even if relatively small, will eventually cause instabilities as the gain increases. These instabilities are associated with notches found in the roll-off region of LQG compensators, which become sharper and deeper as the gain is increased and eventually miss the mode targeted for gain stabilization.

For a control weight of $\rho = 10^{-2}$ the two curves are very close in the roll-off region, indicating that the amount of control used is very close to causing an instability. It was found experimentally that controllers with relative control weights greater than or equal to 10^{-2} were stable while those designed with control weights less than 10^{-2} were unstable for both test articles, demonstrating that this stability robustness test is useful for obtaining good order of magnitude estimates of the control authority which can be applied to the test articles without destabilizing mis-modeled modes.

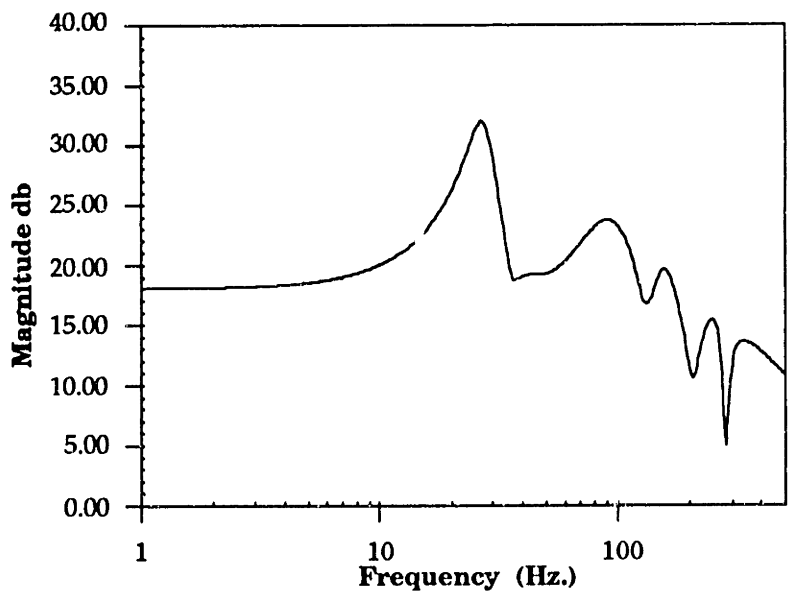

Figure 7.6. Typical bench-top compensator maximum singular value plot. The graph shows high gain in the control bandwidth and notching in the roll-off region. The compensator was designed for the aluminum test article with of control weight of 10^{-2} and sensor noise of 3 percent.

7.4 Performance Robustness Correlation

The stability robustness test provides a means for comparing the amount of control authority being used to the amount which can be applied to the system without causing instabilities. It is instructive to combine this control authority information with performance measurements for comparison of the relative control effectiveness of various compensator designs. Further, the stability robustness test is used to explain the cause of high gain compensator instabilities which limit the maximum achievable performance.

Such a comparison can be made by plotting the analytically predicted and experimentally measured closed loop state cost versus control cost (normalized by the open loop state cost). Cost curves for the compensators designed with an assumed measurement noise of 3.0 percent are plotted in Fig. 7.7 for the aluminum test article. Analytically predicted cost curves are shown in the figure for design model LQG, reduced order LQG and optimal projection compensators. The figure shows that the reduced order LQG compensators deviated from the design model compensators only for those designs with very high control gains ($\rho = 10^{-3}$ and 10^{-4}). The reduced order LQG and optimal projection experimentally measured cost curves are compared to the analytic results in Fig. 7.7. Experimental results are plotted for designs with relative control weights ρ of 1 (large state cost and low control cost), 10^{-1} and 10^{-2} (low state cost and large control cost). Notice that the two experimental compensator cost curves provide the same disturbance attenuation performance (optimal projection offers no improvement) and that these results compare favorably to those predicted analytically.

It was determined analytically that the high gain stable reduced order compensator (relative state to control cost weighting $\rho = 1e^{-3}$) decreased the state cost by 97.2 percent (83.4 percent RMS) or 15.6 db for the aluminum plate test article. However, model errors predicted by the stability robustness test prevented such performance from being achieved experimentally. Fig. 7.7 shows that the most effective controller implemented ($\rho = 10^{-2}$) was able to reduce the state cost significantly. This reduced order LQG compensator was analytically predicted to decrease the state cost by 97.1 percent (83.1 percent RMS) or 15.4 db. It was found experimentally that

this controller actually reduced the state cost by 96.3 percent (80.8 percent RMS) or 14.3 db.

Similarly, excellent disturbance attenuation results were found for the G/E test article. Analytical and experimental cost curves for compensators designed with an assumed measurement noise of 3.0 percent are plotted in Fig. 7.8. As with the aluminum test article compensators, the G/E plate design model and reduced order LQG compensator cost curves deviate only for the very high gain controllers derived using a control weight ρ of 10^{-3}. Also, the experimentally measured and analytically predicted costs are in good agreement over the entire set of compensator designs. Further, only those designs which were predicted to be stable by the stability robustness test were experimentally found to be stable.

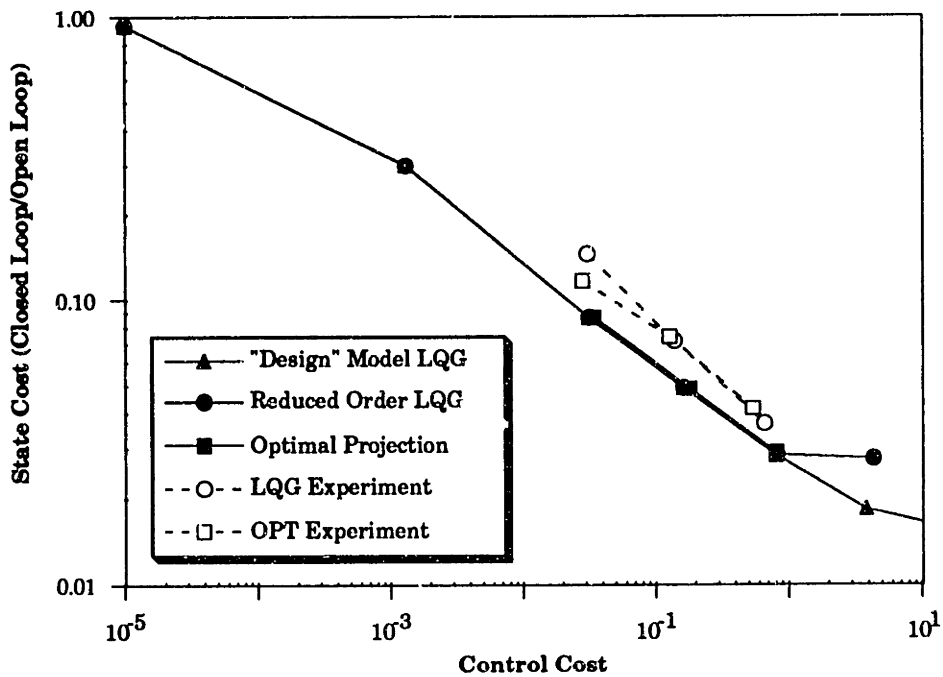

Figure 7.7. Analytical and experimental state versus control closed loop cost curves for the aluminum test article disturbance rejection compensators designed for a sensor noise estimate of 3%.

The best (largest state cost reduction) experimentally stable G/E plate compensator was predicted to reduce the state cost by 97.5 percent (84.2 percent RMS) or 16.0 db. This compensator ($\rho = 10^{-2}$) was experimentally found to attenuate the state cost response by 97.1 percent (83.0 percent RMS) or 15.4 db. Such a large reduction in the state cost or

RMS response is especially significant in light of the 500 Hz bandwidth over which the cost was calculated, which included 10 structural modes.

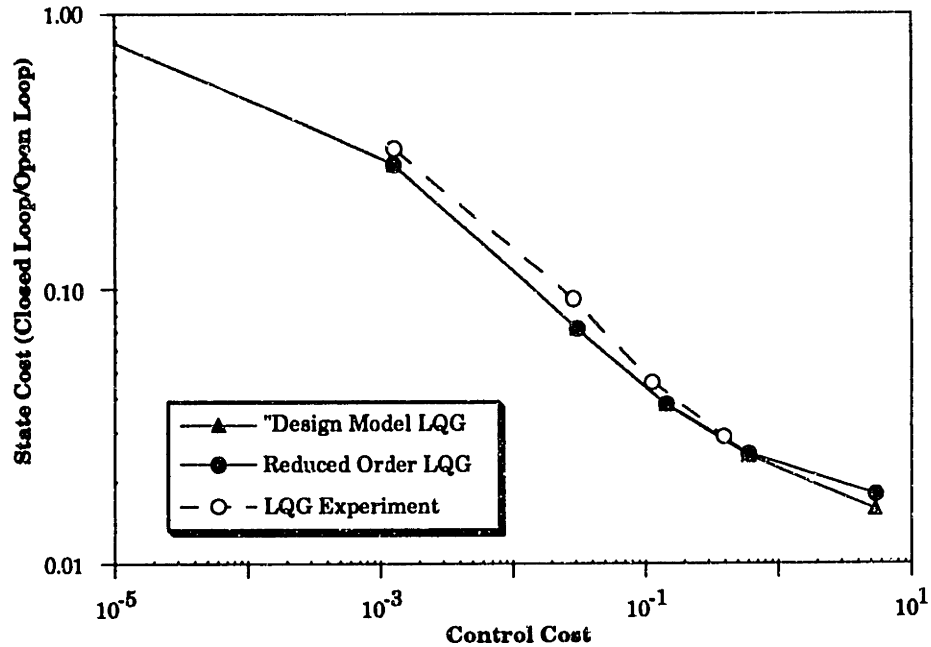

Figure 7.8. Analytical and experimental state versus control closed loop cost curves for the G/E test article disturbance rejection compensators designed using a sensor noise estimate of 3%.

The cost curves showed that reducing the order of the compensator had essentially no effect on controller performance, and the compensators designed using optimal projection performed no better that those derived from the design model and then reduced. Additionally, it was observed that increasing the order (above 14 states) of the compensators implemented had no effect on closed loop performance. Therefore, all experimental instabilities were attributed to model errors, as predicted by the modified stability robustness test, rather than model or compensator order reduction.

Chapter 8. Wind Tunnel Experiments

The bench-top experiments showed the ability of the controllers designed to add significant amounts of damping to the lightly damped test articles. The control laws were able to add damping to several flexible modes, each of which had roughly the same low (1.5 percent) structural damping. Similar performance results are desired in the wind tunnel. However, the structural dynamics of the test articles and the nature of the controllers designed are different in the wind tunnel due to the unsteady aerodynamic forces. The presence of the unsteady aerodynamic forces influences the mode shapes, natural frequencies and damping of the lifting surface test articles. The unsteady aerodynamics also adds additional lags to the system. Further, the nature of the gust disturbance forces are much different (higher force, lower bandwidth) than those disturbances encountered on the bench-top.

Three sets of wind tunnel investigations were performed. First, gust alleviation experiments, similar to the bench-top disturbance rejection tests, were carried out to show the ability of strain actuation to attenuate simulated atmospheric gusts. Second, command following experiments were performed to access the ability of active lifting surfaces to follow commands typical of those required for aircraft maneuverability. Third, flutter suppression experiments were conducted to not only demonstrate flutter suppression, but also to show that the response to disturbances in the air steam could be suppressed using strain actuation.

The wind tunnel experiments served to both validate the analytical aeroelastic model and demonstrate the ability of distributed strain actuators to control aeroelastic lifting surfaces. Since effective model-based compensators can only be derived from accurate models, the ability to implement effective controllers simultaneously demonstrates modeling and control capability. Further, the degree of model fidelity determines the performance which can be achieved, as shown by the performance achieved in the bench-top tests. Similar performance, stability robustness and performance robustness correlation results are reported for the wind tunnel experiments.

8.1 Gust Alleviation Performance Results

The unsteady aerodynamic forces created by the lifting surface motion were found to add large amounts of damping to the first bending and torsion modes at the gust alleviation test velocity of 60 mph. The analytical models (see Tables 5.3 and 5.4) predict damping increases of roughly 10 and 20 times for the first bending mode and 2 and 3 times for the first torsion mode over the bench-top values for the aluminum and washin configured G/E test articles, respectively. The fact that these low frequency modes are so heavily damped, along with the large low frequency disturbance forces created by the gust generator, means that large actuator forces must be applied by the strain actuators to achieve significant disturbance attenuation. These large actuator forces can be created by designing compensators with large low frequency gain. However, the compensator gain must roll-off without destabilizing the high frequency modes, which are not heavily influence by the aerodynamics and remain lightly damped. The combination of having large compensator gains at low frequencies and needing to roll-off the compensator through lightly damped modes makes the problem of achieving good gust alleviation performance while maintaining stability robustness very challenging.

Despite the aforementioned difficulties, good gust alleviation can be obtained from lifting surfaces with distributed strain actuators. Figs. 8.1 and 8.2 display the analytical and experimental gust generator input $\mathbf{d}$ to leading edge laser sensor y_1 open and closed loop response. The open loop response was calculated from Eq. 5.3.2 and the closed loop response was calculated using Eq. 7.1.1, as were the bench-top disturbance transfer functions. However the disturbance forcing matrix $\mathbf{L}$ now represents the gust generator forces and the system matrices include aerodynamic forces and additional states. As for the bench-top experiments, 14 state reduced order compensators were implemented experimentally and evaluated analytically. The compensators were evaluated using the 98 state full order aeroelastic evaluation model. Figs. 8.1 and 8.2 show the disturbance transfer functions for the compensator designs which achieved the best gust response attenuation for the aluminum and G/E washin configured lifting surfaces, respectively. The controllers were designed using a control weight ρ of 10^{-1}

and a sensor noise of 1.0 percent for both the aluminum the G/E lifting surfaces.

The gust response transfer functions show both the accuracy of the aeroelastic analytical model and the ability of the actively controlled lifting surfaces to alleviate gust disturbances. The validity of the analytical model is shown by comparing the quasi-steady response and the pole and zero locations of the analytical and experimental disturbance transfer functions. In each case the agreement was found to be quite good. The active lifting surface gust alleviation effectiveness can be observed from the first bending and quasi-steady response in Figs. 8.1 and 8.2. For both lifting surfaces, controllers are shown which reduce the response of the first bending mode by approximately 10 db, even though there was about 14 and 29 percent open loop damping in this mode of the aluminum and G/E test articles, receptively. Control effectiveness is also shown in the quasi-steady response which was observed to decrease that of the open loop by 3 db for the aluminum and 6 db for the G/E test article. Note that the G/E lifting surface was more effective in controlling the quasi-steady response because of its bending/twist coupling.

It was also expected that the G/E plate bending/twist coupling would allow for enhanced control of the torsional vibration modes. However, this control was not realized because the gust forces barely excited the torsional modes (compared to the first bending mode), which caused the compensators designed to only attempt to effect control of the bending mode. In fact, so much of the vibration energy and therefore the cost was associated with the first bending mode and quasi-steady response, that other modes were purposely destabilized (but not made unstable) in favor of applying more control to the first bending mode and quasi-steady response. The fact that all control efforts are concentrated in the frequency range only up to the first bending mode is shown by the destabilized third mode (second bending) seen in the figures. Note that the destabilized mode is not a result of either model error or reduction, since this behavior was found even when evaluating design model compensators using the design model itself. Finally, note that the disturbance forces are large compared to those experienced on the bench-top (no times ten output factor was used in the wind tunnel).

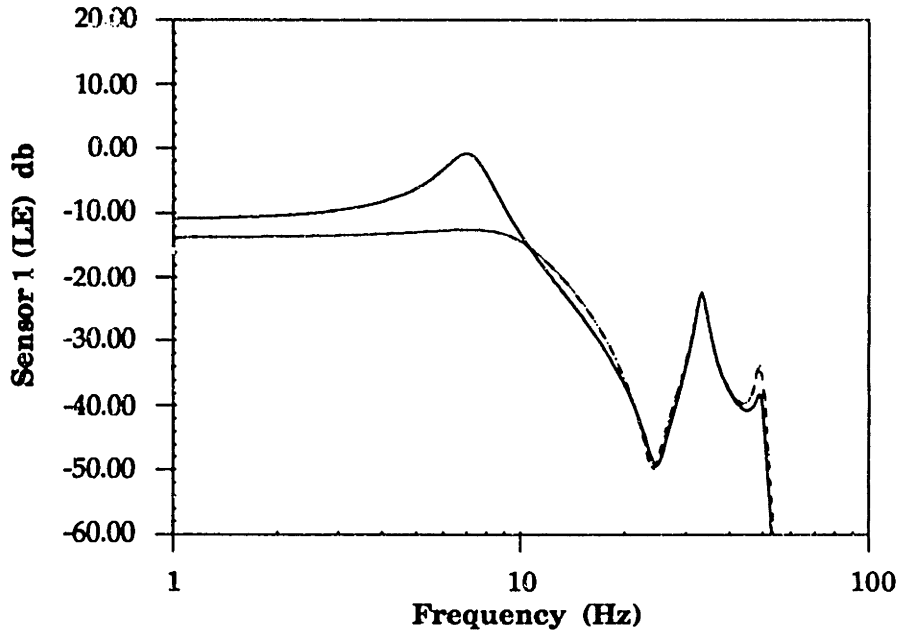

Figure 8.1a. Analytical open and closed loop frequency response of the aluminum lifting surface for a LQG gust alleviation compensator designed with $\rho = 10^{-1}$ and a sensor noise of 1.0 percent.

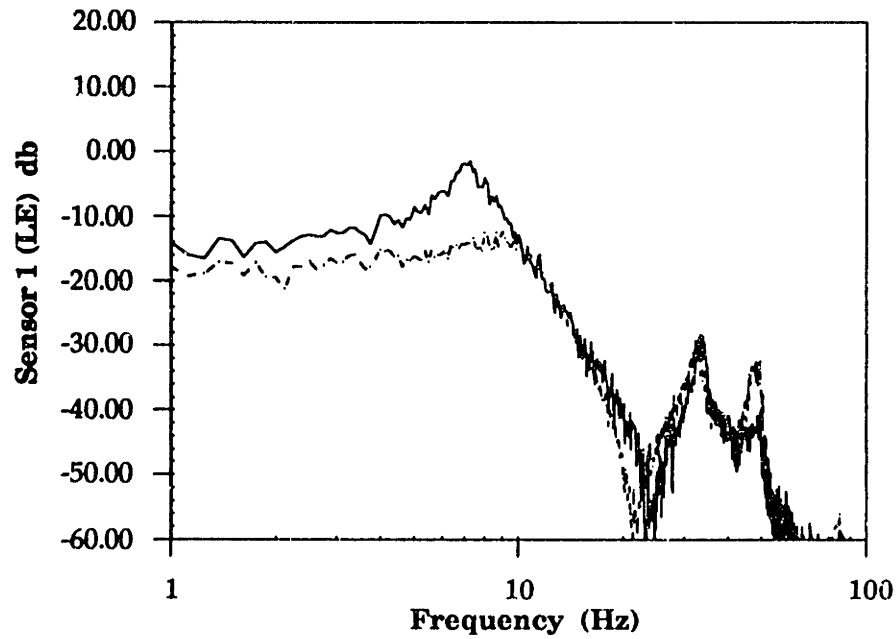

Figure 8.1b. Experimental open and closed loop frequency response of the aluminum lifting surface for a LQG gust alleviation compensator designed with $\rho = 10^{-1}$ and a sensor noise of 1.0 percent.

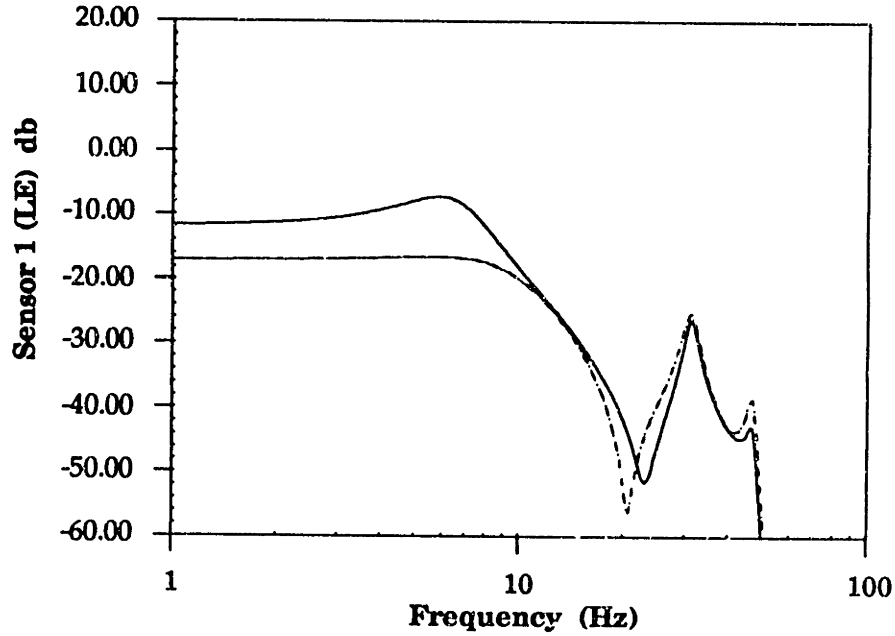

Figure 8.2a. Analytical open and closed loop frequency response of the G/E lifting surface for a LQG gust alleviation compensator designed with $\rho = 10^{-1}$ and a sensor noise of 1.0 percent.

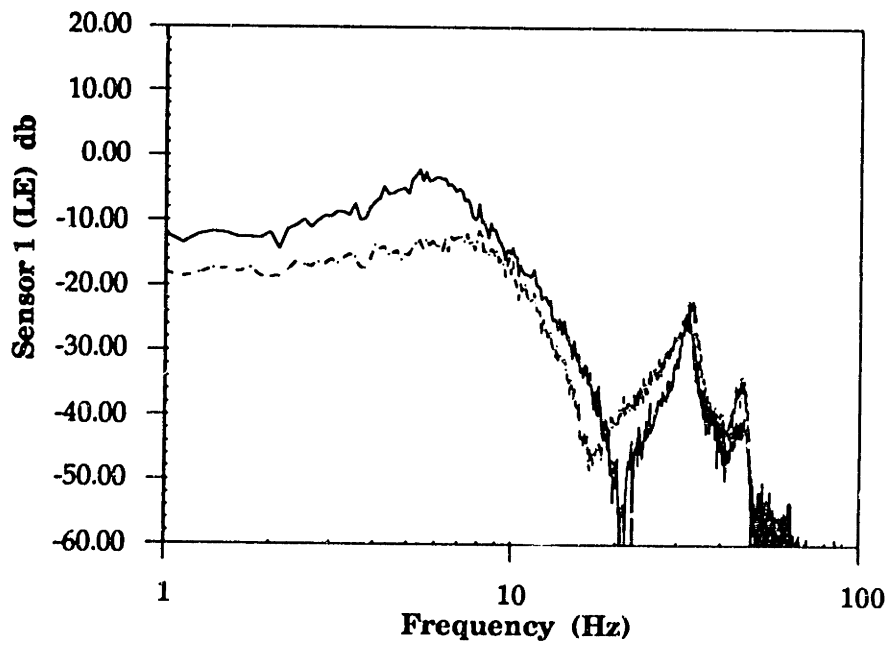

Figure 8.2b. Experimental open and closed loop frequency response of the G/E lifting surface for a LQG gust alleviation compensator designed with $\rho = 10^{-1}$ and a sensor noise of 1.0 percent.

8.2 Gust Alleviation Stability Robustness

The compensators used to calculated the analytical and implemented to measure the experimental disturbance transfer functions (Figs. 8.1 and 8.2) were those found to be most effective at attenuating gust disturbances. These compensators were designed using a control weight ρ of 10^{-1}. Compensators designed with lower control weights (higher gains) were found experimentally to be unstable. The stability of both the stable high performance compensators ($\rho = 10^{-1}$) and the unstable compensators ($\rho < 10^{-1}$) was predicted using the modified stability robustness test described in section 7.3. The modified stability robustness test was able to give a good order-of-magnitude estimate of the maximum control authority which could be used before encountering instabilities for both the aluminum and G/E lifting surfaces.

The results of applying the modified stability robustness test (Eq. 7.2.2) to the gust alleviation compensators designed for the aluminum and G/E test articles are shown in Figs. 8.3 and 8.4, respectively. The figures display the maximum singular values of the modified closed loop transfer function matrix $\sigma_{max}[\mathbf{C}_\Sigma(s)]$ verses the inverse of the error maximum singular values $1/\sigma_{max}[\Delta_\Sigma(s)]$ for low ($\rho = 1.0$) and high ($\rho = 10^{-1}$) gain stable compensator designs. For both lifting surfaces, the closed loop maximum singular values are below the inverse error maximum singular values in the wind tunnel gust alleviation compensator roll-off region (above 80 Hz). Therefore, the modified stability robustness test suggests that these compensator designs will be stable.

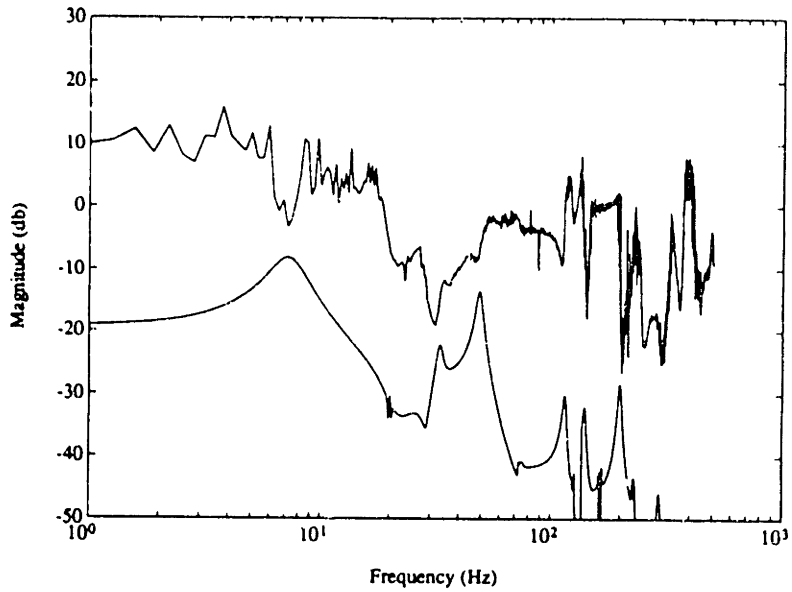

Figure 8.3a. Wind tunnel closed loop transfer function $C_\Sigma(s)$ maximum singular values and the reciprocal of the error $\Delta_\Sigma(s)$ maximum singular values for the aluminum plate with a LQG compensator designed with $\rho = 10^0$ and the sensor noise estimated at 1.0%.

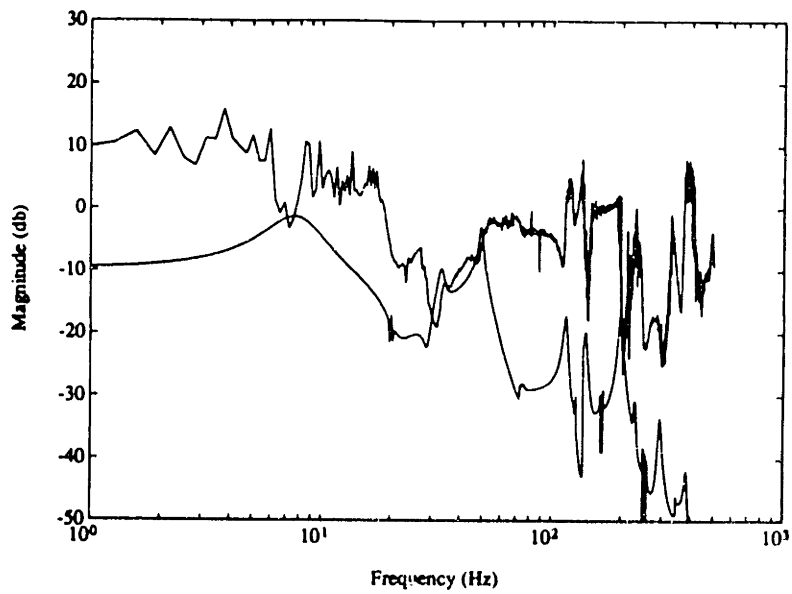

Figure 8.3b. Wind tunnel closed loop transfer function $C_\Sigma(s)$ maximum singular values and the reciprocal of the error $\Delta_\Sigma(s)$ maximum singular values for the aluminum plate with a LQG compensator designed with $\rho = 10^{-1}$ and the sensor noise estimated at 1.0%.

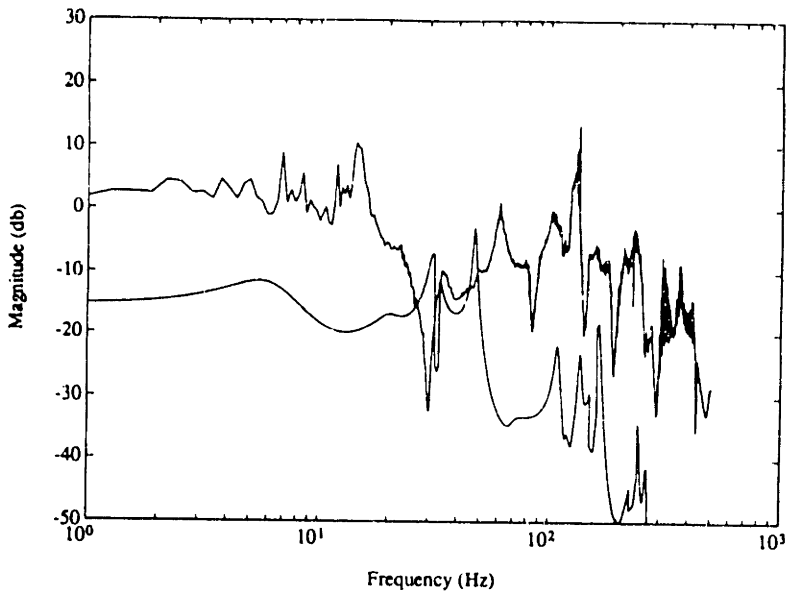

Figure 8.4a. Wind tunnel closed loop transfer function $C_\Sigma(s)$ maximum singular values and the reciprocal of the error $\Delta_\Sigma(s)$ maximum singular values for the G/E plate with a LQG compensator designed with $\rho = 10^0$ and the sensor noise estimated at 1.0%.

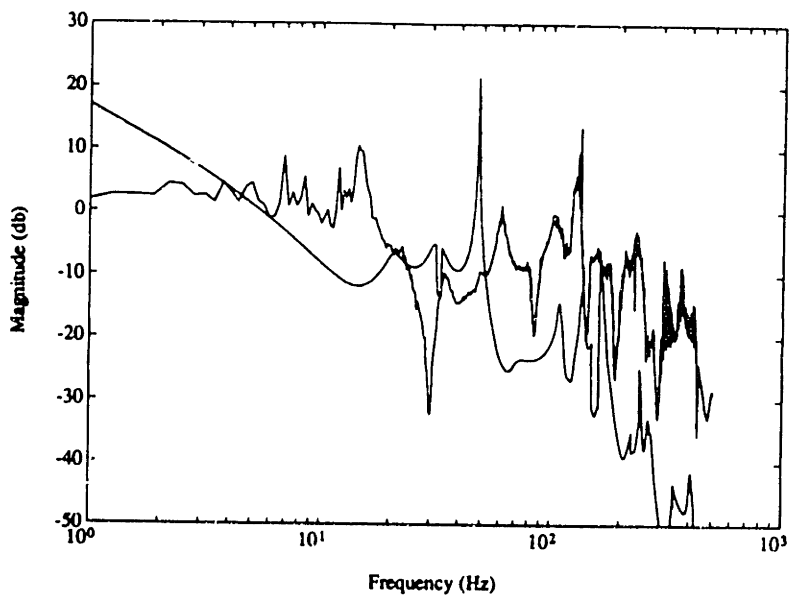

Figure 8.4b. Wind tunnel closed loop transfer function $C_\Sigma(s)$ maximum singular values and the reciprocal of the error $\Delta_\Sigma(s)$ maximum singular values for the G/E plate with a LQG compensator designed with $\rho = 10^{-1}$ and the sensor noise estimated at 1.0%.

As observed in the bench-top stability robustness section, decreasing the control weight increases the control gain and moves the maximum singular values of the closed loop transfer function closer to the inverse error maximum singular values. Figs. 8.3 and 8.4 show that the high gain stable compensators designed with a control weight ρ of 10^{-1} have closed loop maximum singular values $\sigma_{max}[\mathbf{C}_\Sigma(s)]$ which just touch the inverse error maximum singular values $1/\sigma_{max}[\Delta_\Sigma(s)]$ in the roll-off region. The proximity of the two singular value curves indicates that some of the poles in the roll-off region are close to being driven unstable, and any increase in gain will cause such instabilities to occur. Further, during closed loop wind tunnel testing it was found that controllers designed for both gust alleviation test articles with a control weight of 10^{-2} were, in fact, unstable. But, factors other than modeling errors (accounted for by the modified stability robustness test) could have contributed to such instabilities. For example, aerodynamic, substructure and actuator non-linearities (especially important for compensators with high gains) can help drive a system unstable. Note that a considerable amount of non-linear behavior, in the form of limit cycle oscillations and saturated actuators, was observed during wind tunnel testing.

8.3 Gust Alleviation Performance Robustness Correlation

The performance shown by the gust disturbance response transfer functions can be quantified and correlated with the control authority needed and the maximum control authority available (determined by the stability robustness test) by plotting the state cost versus control cost. Wind tunnel gust alleviation state versus control cost plots identify the incremental state cost reduction obtained from increased control authority, as was found for the bench-top experiments. Analytical and experimental cost curves are plotted in Figs. 8.5 and 8.6 for the gust alleviation experiments. The analytic values were calculated by solving the associated closed loop Lyapunov problem defined by Eqs. 7.1.2 and 7.1.3. The experimental values were found from the RMS sensor outputs and control inputs measured over the 200 Hz wind tunnel test evaluation bandwidth. All values were normalized by the open loop state cost, so that the infinite control weighting (zero control gain) cost is unity.

Controllers designed for the gust alleviation experiments with sensor noise estimates of 1.0 percent are shown in Figs. 8.5 and 8.6 for the aluminum and G/E lifting surfaces, respectively. The analytic curves show the expected state cost reduction for the design model and reduced order LQG compensators. The curves, calculated using the full order evaluation model, show that no performance degradation results from the compensator reduction process needed to implement the compensators on the digital control computer, even for very high gain (experimentally unstable) compensator designs. Reducing the compensators had no effect on performance due to the high-authority, but lower bandwidth (compared with the bench-top tests) nature of the compensators. Experimental results are plotted for controllers designed with control weights of 1.0 and 10^{-1} for the aluminum and 10^{1}, 1.0 and 10^{-1} for the G/E lifting surface. The figures show excellent agreement between the analytical and experimental results, and that significant disturbance attenuation was achieved despite the relatively high open loop damping in the lower modes.

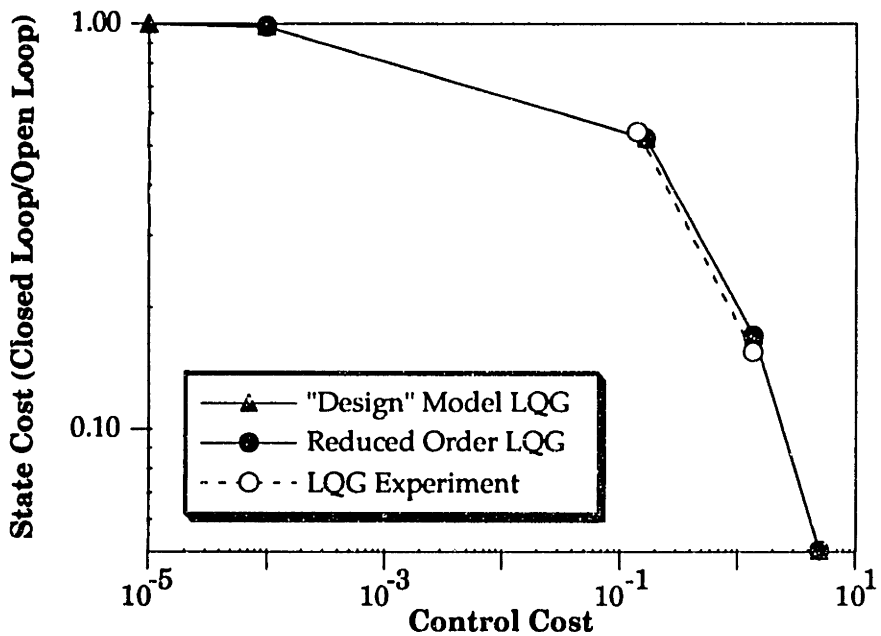

Figure 8.5. Analytical and experimental state versus control closed loop cost curves for the aluminum lifting surface gust alleviation compensators designed with a sensor noise estimate of 1.0%.

It was found that the compensators best able to attenuate disturbances were designed with a control weight ρ of 10^{-1}. Compensators designed with lower control weights (higher gains) were unstable, as discussed in the stability robustness section. The high performance gust alleviation compensator designs ($\rho = 10^{-1}$) were analytically predicted to reduce the aluminum lifting surface state cost by 77.3 percent (52.3 percent RMS) or 6.4 db, and the G/E lifting surface compensator was predicted to reduce the state cost by 84.1 percent (60.1 percent RMS) or 8.0 db. The aluminum lifting surface compensator was experimentally found to reduce the state cost by 79.2 percent (54.3 percent RMS) or 6.8 db, while the G/E lifting surface compensator was able to reduce the state cost by 83.6 percent (59.6 percent RMS) or 7.9 db.

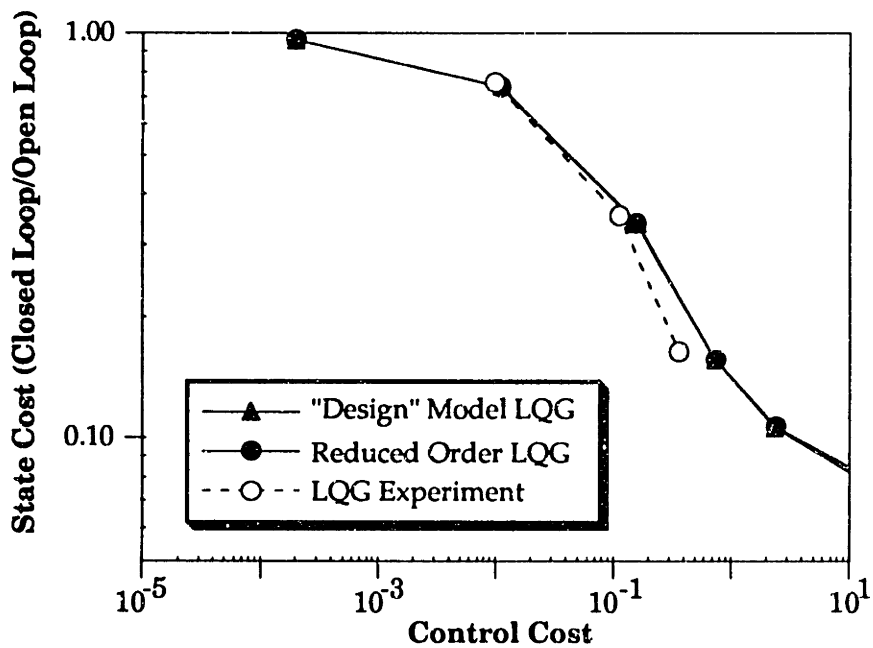

Figure 8.6. Analytical and experimental state versus control closed loop cost curves for the G/E lifting surface gust alleviation compensators designed with a sensor noise estimate of 1.0%.

Note that the control authority, measured by the voltage supplied to the piezoceramics, used by the highest performing stable controllers (roughly 100-140 V RMS) was about double the largest amount used in the bench-top experiments. Therefore, not only were the actuators behaving non-linearly

due to the high voltages relative to the coercive field [Lazarus and Crawley, 1989], but also, the peak voltages commanded were being clipped by the power amplifiers which were limited to plus or minus 200 V. The amplifier clipping added yet another factor which contributed to causing very high gain compensator designs (control weights less that 10^{-1}) to be unstable.

8.4 Command Following Performance Results

The previous sections showed the ability of active control systems to suppress unwanted lifting surface vibrations due to gust disturbances. Active gust alleviation is desirable for improving ride quality and reducing loads. It is also desirable to enhance aircraft maneuverability through the use of active controls. Aircraft maneuverability can be improved by using distributed strain actuators to control the shape of the lifting surface and thus the aerodynamic forces needed for pull-up and roll maneuvers. One command in particular, which could be used to generate such maneuver forces, is that of a commanded lifting surface tip twist.

The ability of active lifting surfaces to respond to a commanded tip twist is investigated in the command following wind tunnel experiments. Specifically, the leading y_1 and trailing y_3 edge tip displacements, which results from the tip twist associated with a constant spanwise bending moment acting on the bending/twist coupled G/E test article, is examined. The ability of the leading and trailing edge tip positions to track quasi-steady, low frequency and high frequency commands in the presence of disturbance forces is assessed in closed loop wind tunnel experiments. The performance achieved by the compensators designed for command following is determined in the frequency domain by examining the closed loop error transfer functions, which are the response from a commanded signal to the error. The closed loop error transfer functions can be expressed in state space form as

$$\begin{bmatrix} \dot{\mathbf{x}} \\ \dot{\hat{\mathbf{x}}} \end{bmatrix} = \begin{bmatrix} \mathbf{A} - \mathbf{B}\mathbf{D}_c\mathbf{C} & -\mathbf{B}\mathbf{F}_c \\ \mathbf{K}_c\mathbf{C} & \mathbf{A}_{cc} \end{bmatrix} \begin{bmatrix} \mathbf{x} \\ \hat{\mathbf{x}} \end{bmatrix} + \begin{bmatrix} \mathbf{B}\mathbf{D}_c \\ -\mathbf{K}_c \end{bmatrix} \mathbf{r}_c$$

$$\mathbf{e} = [\mathbf{C} \quad \mathbf{0}] \begin{bmatrix} \mathbf{x} \\ \hat{\mathbf{x}} \end{bmatrix} - [\mathbf{I}]\mathbf{r}_c \tag{8.4.1}$$

where the error $\mathbf{e}$ is defined as the difference between the commanded tip displacements $\mathbf{r}_c$ and the displacements measured by the laser sensors $\mathbf{y}$.

Controllers were designed to enhance the command following performance of the G/E lifting surfaces using the LQG-LTR method described in section 6.2. The results of the command following wind tunnel experiments, which were conducted at 60 mph, are reported in the form of command $\mathbf{r}_c$ to leading y_1 and trailing y_3 edge sensor closed loop error transfer functions. Analytical and experimental closed loop error transfer functions are reported in Figs. 8.7 and 8.8 for reduced order LQG-LTR compensators designed to achieve low frequency and high frequency command following, respectively. The analytical transfer functions were calculated by substituting reduced order compensators and the full order model into Eq. 8.4.1. The experimental transfer functions were found by subtracting the control input from the sensor output signal.

Fig. 8.7 shows the leading edge sensor closed loop error achieved by a LQG-LTR controller designed for low frequency command following. As discussed in section 6.2, the measurement noise was used to set the cross over frequency at about 80 Hz. The control weight ρ was chosen to be 10^{-4}, which was the lowest control weight (highest gain) that yielded a stable compensator. This control weighting gave excellent loop recovery in this low frequency control bandwidth. Therefore, this controller was expected to exhibit good command following performance up to 8.0 Hz. The closed loop error transfer function shows that adequate command following was obtained up to about 7 Hz (note that the command following performance is arbitrarily considered adequate as long as the magnitude of the error transfer function is below -6 db). Fig. 8.7 shows the error approaching zeros as the command frequency decreases towards the steady state, due to the "free" integrators in the compensator. However, the error actually does not continue to decrease past 1.0 Hz since the "free" integrators have been replace with quasi-integrator poles at this frequency to avoid very low frequency actuator saturation. This causes the error from D.C. to the frequency of the quasi-integrator pole to be constant and equal to the value at the frequency of the quasi-integrator. The quasi-steady (about 1.0 Hz) error was analytically predicted to be 20 percent (-14 db). The actual error was measured at 10 percent (-20 db), where the discrepancy between the expected and measured error is due to difficulties in measuring the turbulence in the free stream flow (the gust generator was not activated during these experiments).

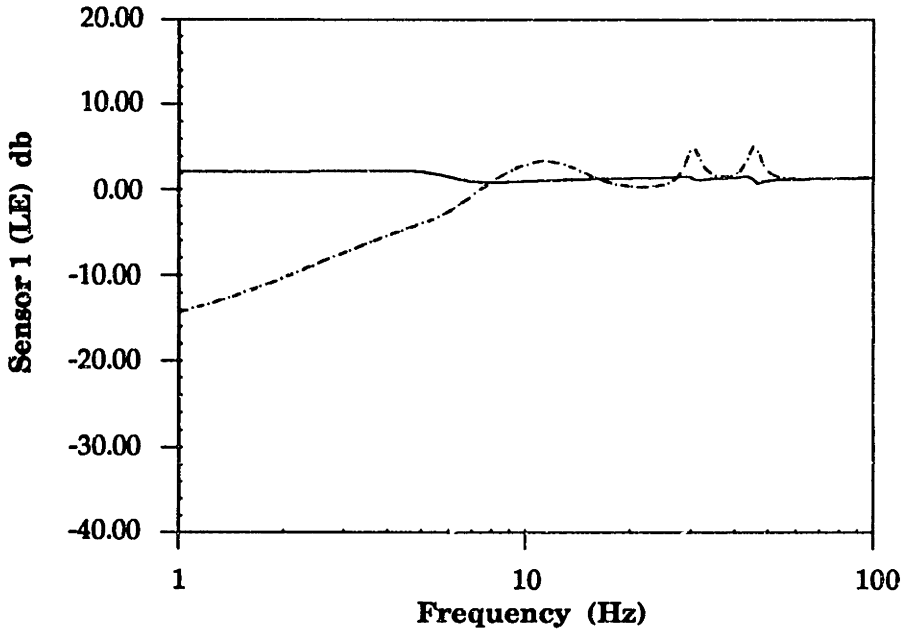

Figure 8.7a. G/E command following analytical closed loop error transfer function for a low frequency LQG-LTR compensator designed with cross over at 80 Hz and $\rho = 10^{-4}$.

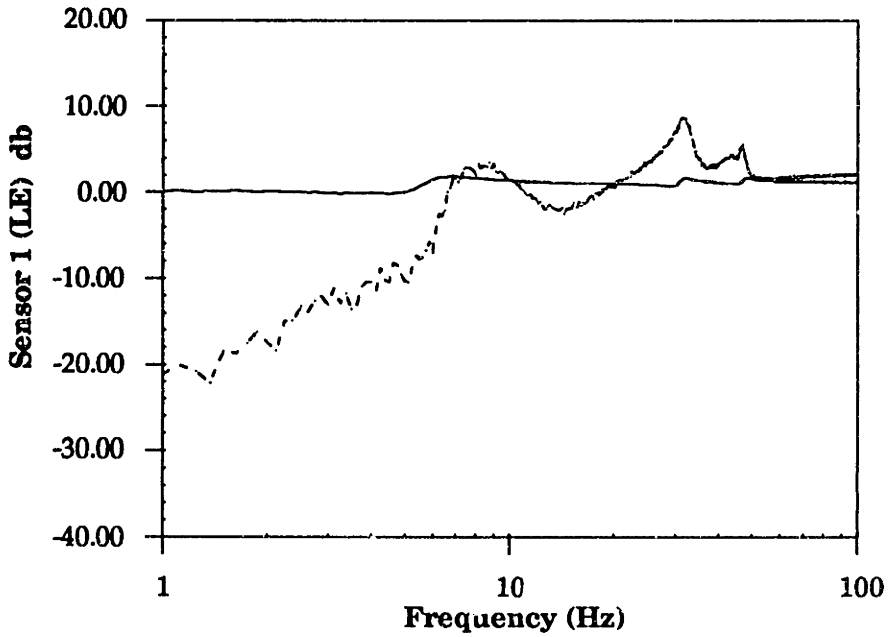

Figure 8.7b. G/E command following experimental closed loop error transfer function for a low frequency LQG-LTR compensator designed with cross over at 80 Hz and $\rho = 10^{-4}$.

Fig. 8.8 displays the closed loop trailing edge y_3 error found using a LQG-LTR compensator designed for higher frequency command following. The compensator was designed with a cross-over frequency of 160 Hz and a control weight of 10^{-6}, which gave good loop recovery only to about 30 Hz. The compensator was analytically predicted to follow commands from quasi-steady though the first bending mode up to about 10 Hz. The controller was also predicted to follow commands near the first torsional frequency at about 30 Hz. The experiment shows that adequate command following was achieved up to 8 Hz and again at about 30 Hz, although performance was found to be a few decibels worse that predicted. Also, Fig. 8.8 shows that the quasi-steady command following performance suffers considerably when attempting to follow commands at higher frequencies. The reduced quasi-steady performance was caused by the need to move the quasi-integrator pole up to 5 Hz in order to avoid very low frequency (less than 1.0 Hz) actuator saturation.

The less than ideal performance achieved emphasizes several problems with using the LTR method for designing compensators to control the command following response of flexible structures. First, it is very difficult to obtain a model of sufficient accuracy to fully recover the desired filter loops. A detailed plant model is required at least one decade above the bandwidth in which command following is desired, since cross-over of the loop transfer function maximum singular values will occur above this bandwidth. Second, an order of magnitude increase in control authority is needed for each decade in which commands are to be followed, since the design method employed shaped the loop singular values to a 20 db per decade $\mu I/s$ roll-off. In the command following experiments carried out, both modeling inadequacies and low frequency actuator saturation limited performance. However, a more sophisticated target filter loop, designed using $\mathcal{H}_\infty$ techniques, would probably have provided better performance results.

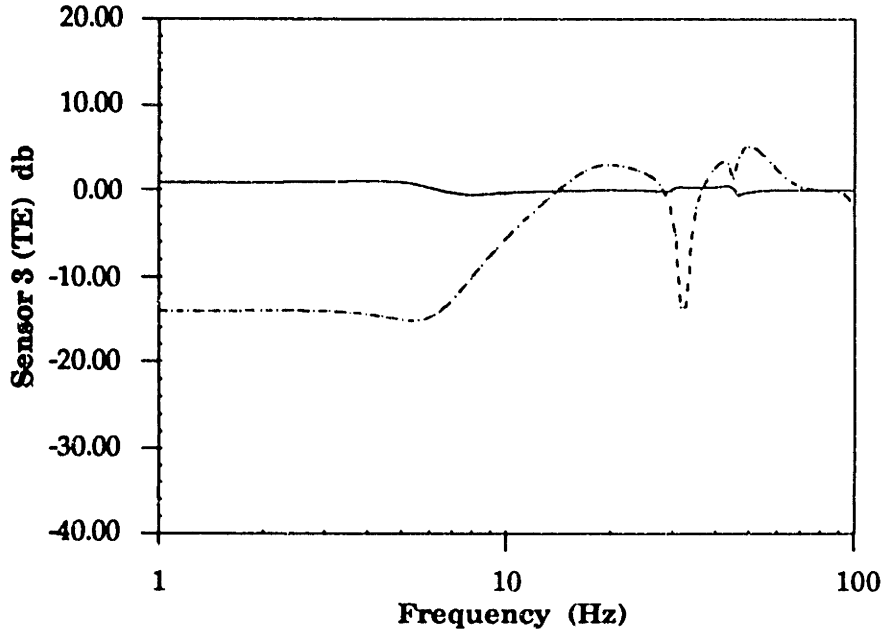

Figure 8.8a. G/E command following analytical closed loop error transfer function for a high frequency LQG-LTR compensator designed with cross over at 160 Hz and $\rho = 10^{-6}$.

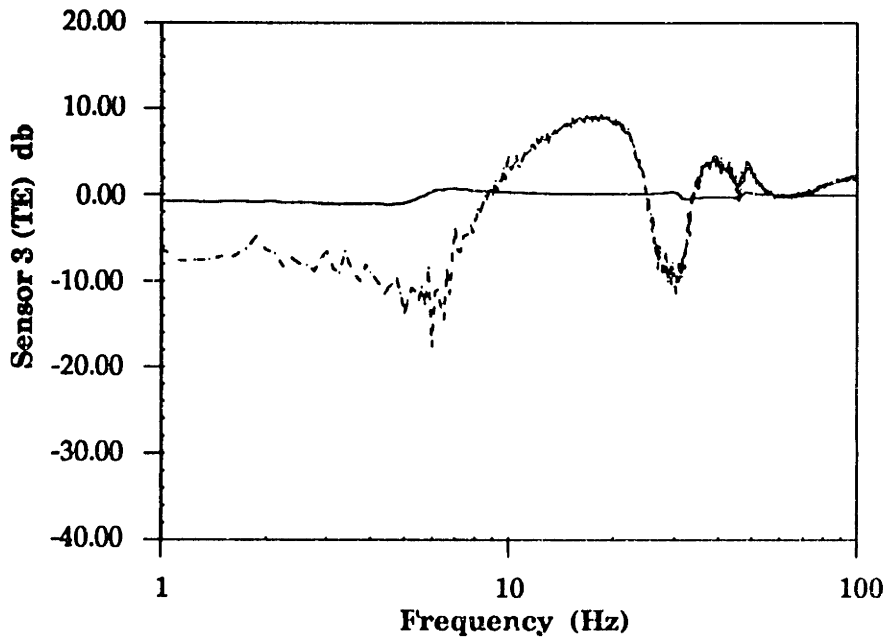

Figure 8.8b. G/E command following experimental closed loop error transfer function for a high frequency LQG-LTR compensator designed with cross over at 160 Hz and $\rho = 10^{-6}$.

8.5 Flutter Suppression Performance Results

After completing the bench-top disturbance rejection, wind tunnel gust alleviation and wind tunnel command following experiments, a lead mass was attached to the aluminum lifting surface for the purpose of performing flutter experiments (configuration details are provided in Chapter 4). The added mass lowered the predicted flutter speed of this modified-for-flutter lifting surface to 88 mph. The flutter mode was observed in the wind tunnel to be the result of a classical coalescence of the first bending and torsion modes, which occurred at the predicted air speed of 88 mph (flutter analysis details can be found in Chapter 5). The gust generator was removed from the wind tunnel for the flutter suppression experiments since the gust vanes themselves fluttered at about 80 mph. Therefore, the disturbance source for the flutter experiments was generated only by the turbulence in the free stream flow, which produced significant disturbance forces because of the high speeds (relative the tunnel maximum speed of 100 mph) at which the flutter suppression experiments were conducted.

Flutter suppression controllers were designed and tested at 90 mph. The flutter suppression controllers were also evaluated analytically for stability and performance at 80 and 85 mph. All compensators designed to suppress flutter at 90 mph were predicted analytically and found experimentally to be stable at both 80 and 85 mph. Therefore, the experimental procedure was as follows: First, the air speed was set at 80 mph and the open loop response of the laser sensors, due to the flow turbulence, was measured. Then, the control computer was turned on and the wind speed was slowly raised to the flutter suppression design speed of 90 mph. At the design speed, the RMS sensor outputs and control inputs were measured using the Fourier analyzer. Finally, the wind speed was increased until either the system became unstable or the tunnel limit was reached.

The results of the wind tunnel flutter suppression experiments are reported by plotting closed loop state versus control cost curves, similar to those reported for the bench-top disturbance rejection and wind tunnel gust alleviation tests. The costs curves show the incremental improvement of the

state cost gained (reduction in RMS response) as the control effort is increased, relative to the maximum control authority which could be used before high frequency modes were destabilized. As before the analytical costs were calculated by inserting the compensators and the full order aeroelastic model into Eqs. 7.1.2 and 7.1.3, and the experimental costs were found by measuring the RMS sensor outputs and control inputs (200 Hz bandwidth). However unlike the previous tests, there is no open loop state cost by which the results can be normalized since the open loop system is unstable at 90 mph. Thus, the closed loop state and control costs are normalized by the open loop state cost at 80 mph. In addition, the open loop state cost is not recovered and the control gains do not go to zero as the control weigh ρ becomes large because the open loop system is unstable. Instead, some amount of control authority is needed, indicated by a finite control cost and a vertical asymptote of the cost curve, to stabilize the system.

Fig. 8.9 displays the analytical and experimental cost curves for the modified-for-flutter aluminum lifting surface tested at 90 mph with compensators designed using an assumed sensor noise of 1.0 percent. Observe that stable flutter suppression compensators (finite state costs) have been designed and implemented, and that agreement between the analytically predicted and experimentally measured results are quite good. Also note that the figure shows the minimum control effort needed to stabilize the initially unstable system, indicated by the low control weight asymptote. Compensators designed with control weights greater than 1.0 are observed to only have enough control authority to stabilize the system. However, as the control weight is decreased, higher gain compensators are designed which are capable of not only stabilizing the system, but also of reducing the disturbance response. The disturbance response continues to decrease as the control weight is decreased (gains increase) until the design with the minimum disturbance response is found ($\rho = 10^{-2}$). The figure indicates that compensators with higher gains ($\rho = 10^{-4}$) were analytically predicted to further decrease the state cost, however stability robustness issues prevented any of these designs from actually achieving better performance. These designs were found either to destabilize high frequency modes, indicated in the figure by the design with an experimentally measured

high state cost and high control cost, or to be unstable (not shown in the figure).

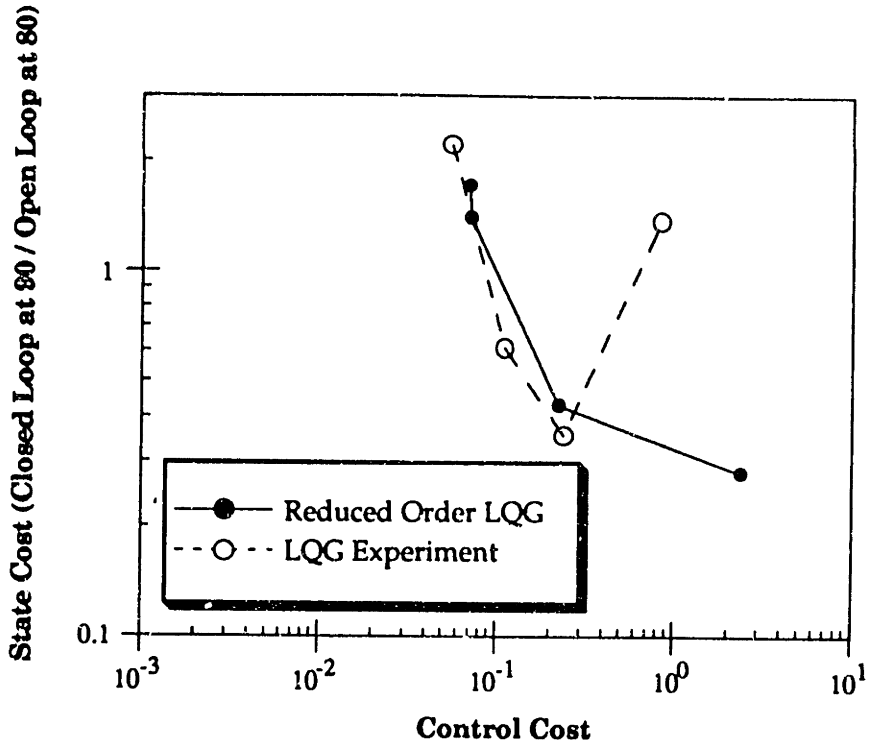

Figure 8.9. Analytical and experimental state versus control closed loop cost curves for the modified-for-flutter aluminum lifting surface 90 mph flutter suppression experiments. Compensators were designed with a sensor noise estimate of 1.0%, and all values are normalized by the 80 mph open loop state cost.

The compensator design ($\rho = 10^{-2}$) which stabilized the system at 90 mph and minimized the disturbance response was analytically predicted to decrease the state cost from that of the 80 mph open loop system by 71.9 percent (47.0 percent RMS) or 5.5 db. This compensator was found experimentally to stabilize the system and reduce the disturbance response by 76.0 percent (51.0 percent RMS) or 6.2 db. In addition, this controller was able to suppress flutter up to 98 mph, 11 percent above the flutter speed and 9 percent above the 90 mph air speed for which the compensator was designed.

Conclusions

This thesis has investigated and developed the basic technology necessary for the aeroelastic control of plate-like lifting surfaces using distributed strain actuators. Simple models were used to reveal the fundamental mechanisms and limitations of aeroelastic control. This analysis showed that the poles of an aeroelastic system and the zeros of various actuator to sensor transfer functions move rapidly with airspeed, which indicates that certain actuator and sensor combinations may be more desirable than others. In particular, it was found that combinations which include strain actuators often lead to input/output combination which are advantageous for closed loop control, especially compared with conventional aileron controlled transfer functions which sometimes contain non-minimum phase zeros. This analysis also pointed out the advantages of having multiple actuator inputs, and that only through the use of strain actuation can such multiple input systems be realized. Simple models were also used to identify the parameters important for the effective use of strain actuators integrated in plate-like structures. It was found that strain actuators are most effective when the mechanical impedance of the actuators are matched to that of the substructure, not dissimilar to the impedance matching arguments familiar to electrical engineers.

The concepts revealed by the simple models were used to design scale model active lifting surface test articles. Detailed analytic models were then formed to analyze the test articles. An aeroelastic model was developed for plate-like structures with integrated strain actuators which gave sufficient fidelity so that implementable high-authority, high-bandwidth model-based compensators could be designed. The model combined the Rayleigh-Ritz assumed mode method, kernel function unsteady aerodynamics and a non-linear least squares rational approximation procedure. It was found that by carefully selecting the assumed modes and number of aerodynamic lags, and incorporating experimentally measured damping estimates, a model of sufficient fidelity for designing high-authority compensators could be obtained.

A control law development procedure was established which utilized performance measurements and LQG design variables in a consistent manner in order to design high-authority multivariable compensators. A model order reduction procedure was also developed for the purpose of implementing the controllers on a real time digital computer. Further, a stability robustness test was found which could estimate, *a priori*, the amount of control authority which could be applied to the system without destabilizing high frequency modes. The robustness test was able to give reasonably good estimates of closed loop stability based only on open loop transfer function data and the analytic model.

Closed loop bench-top and wind tunnel experiments validated the modeling and control law development procedures, and demonstrated the ability of integrated strain actuators to effect high-authority multivariable control on flexible plate-like structures. The bench-top results showed that considerable disturbance attenuation could be achieved throughout large bandwidths containing several flexible modes. Controllers implemented reduced the quasi-steady response by over 10 db and the response of the first flexible mode by over 30 db. These high performance controllers decreased the RMS response of the system by more than 83 percent.

Wind tunnel testing demonstrated the ability of strain actuated active lifting surfaces to effect a variety of aeroelastic control objectives such as gust alleviation, command following and flutter suppression. These objectives relate directly to aircraft design criteria such as ride quality and maximum wing loading, maneuverability, flight envelope and overall performance. The wind tunnel tests showed that significant performance improvements could be obtained through strain actuated active aeroelastic control. The active lifting surface test articles were found to attenuated the RMS gust response by over 60 percent in the gust alleviation experiments. And, flutter suppression test demonstrated the ability of stain actuated active lifting surfaces to not only suppress flutter, but also to significantly reduce the response to disturbances in the free stream flow.

Note that the importance of the active lifting surface scaling laws developed should not be overlooked, for it is these fundamental relations which governs the applicability of the results obtained to the active control of

actual lifting surfaces. The lifting surface test articles used in this study were able to achieve a remarkable degree of aeroelastic control authority. However these results may only be generalized to other lifting surfaces with the same non-dimensional parameters, such as aspect ratio, thickness ratio, force stiffness ratio and force pressure ratio. In certain applications, such as panel flutter or stabilizer control, scaling the results may require little effort because the geometric parameters are similar. However, scaling the results for some applications may be problematic. For example, typical wings are made of box beam construction and have thickness ratios of at least 2 percent. In order to apply the results of the test articles (thickness ratio of 0.5 percent) to such a wing, the actuator thickness would have to be considerably larger in order to match the force stiffness ratio. On the other hand, engineering ingenuity can be applied to increase control authority using other mechanisms such as increasing the bending/twist coupling (by sweeping the wing) or actuation strain (by making use of d_{33}).

A final concern is that of added actuator weight. With a density more than twice that of aluminum, piezoceramics are hardly the ideal aerospace material. It must be admitted that the implications of such a large actuator weight penalty have been largely ignored in this study, but is a topic which should certainly be investigated thoroughly. One can only hope recent advances in material science are able to provide improved strain actuators which are light in weight, high in strength and have high actuation strains, because this is what is needed to make strain actuated aeroelastic control a truly useful technology.

References

Akishita, S., Mitani, Y.-U., Miyano, K. and Lee, H. G., "Active Control of Sound Transmission Through Rectangular Plate By Piezoelectric Actuator," Proceeding of the Conference on Resent Advances in Active Control of Sound and Vibration, Blacksburg, VA, April, 1991, pp. S22-S34.

Albano, E. and Rodden, W. P., "A Doublet-Lattice Method for Calculating Lift Distributions on Oscillating Surfaces in Subsonic Flows," *AIAA Journal*, Vol. 7, No. 2, Feb., 1969, pp. 279-285. Errata, Vol. 7, No. 11, Nov., 1969, p. 2192.

Balas, M. J., "Trends in Large Space Structures Control Theory: Fondest Hopes, Wildest Dreams," *IEEE Transactions on Automatic Control*, Vol AC-27, No. 3, June, 1982, pp. 522-535.

Bisplinghoff, R. L., Ashley, H. and Halfman, R. L., *Aeroelasticity*, Addison-Wesley Publishing Company, Reading, Massachusetts, 1957.

Blevins, R. D., *Formulas for Natural Frequency and Mode Shape*, Robert E. Krieger Publishing Company, Malabar, Florida, 1984.

Bryson, A. E. and Ho, Y. C., *Applied Optimal Control*, Blaisdell, Waltham, MA, 1969.

Carrier, A., Bryson, A. E. Jr., Aubrun, J.-N. and Lorell, K., "H_∞ Control Design for the ASCIE Segmented Optics Test Bed: Analysis, Synthesis and Experiment," Proceedings of the AIAA Guidance, Navigation and Control Conference, New Orleans, LA, August, 1991, pp. 807-817.

Chiarappa, D. J. and Claysmith, C. R., "Deformable Mirror Surface Control Techniques," *Journal of Guidance and Control*, Vol. 4, No. 1, 1981.

Christhilf, D. M. and Adams, W. M. Jr., "Multifunction Tests of a Frequency Domain Based Flutter Suppression System," Proceeding of the AIAA Dynamics Specialist Conference, Dallas, TX, April, 1992.

Crawley, E. F. and Dugundji, J., "Frequency Determination and Non-Dimensionalization for Composite Cantilever Plates," *Journal of Sound and Vibration*," Vol. 72, No. 1, 1980, pp. 1-10.

Crawley, E. F. and Lazarus, K. B., "Induced Strain Actuation of Isotropic and Anisotropic Plates," *AIAA Journal*, Vol. 29, No. 6, June 1991, pp. 944-951.

Crawley, E.F. and de Luis, J., "Use of Piezoelectric Actuators as Elements of Intelligent Structures," *AIAA Journal*, Vol. 25, No. 10, Oct., 1987, pp. 1373-1385.

Cunningham, A. E., "A Collocation Method for Predicting Subsonic Pressure Distribution on Interfering Parallel Wings," 12th ASME Structures, Structural Dynamics and Materials Conference, California, 1971.

Doyle, J. C., Glover, K., Khargonekar, P. P. and Francis, B. A., "State-Space Solutions to Standard $\mathcal{H}_2$ and $\mathcal{H}_\infty$ Control Problems," *IEEE Transactions on Automatic Control*, Vol. AC-34, No. 8, August, 1989, pp. 831-847.

Doyle, J. C., Wall, J. E. and Stein, G., "Performance and Robustness Analysis for Structured Uncertainty," Proceedings of the 21st IEEE Conference on Decision and Control, Orlando, FL, December, 1982, pp. 629-636.

Ducharme, E. H. and Crawley, E.F., "Velocity Scaled Aeroelastic Testing of an Unducted Fan," GTL Report No. 191, Massachusetts Institute of Technology, Cambridge, MA, 1989.

Ehlers, S. M. and Weisshaar, T. A., "Effect of Adaptive Material Properties on Static Aeroelastic Control," AIAA Paper No. 92-2526, Proceedings of the 33rd Structures, Structural Dynamics and Materials Conference, Dallas, TX, 1992, pp. 914-924.

Ehlers, S. M. and Weisshaar, T. A., "Static Aeroelastic Behavior of an Adaptive Laminated Piezoelectric Composite Wing," AIAA Paper No. 90-1078, Proceeding of the 31st SDM Conference, Long Beach, CA, May, 1990, pp. 1611-1623.

Emami-Naeini, A. and Rock, S. M., "On Asymptotic Behavior of Non-Square Linear Optimal Regulators," Proceedings of the 23rd Conference on Decision and Control, Las Vegas, NV, Dec., 1984, pp. 1762-1763.

Eversman, W. and Tewari, A., "Consistent Rational-Function Approximation for Unsteady Aerodynamics," *Journal of Aircraft*,, Vol. 28, No. 9, Sept., 1991, pp. 545-552.

Fanson, J. L., Lurie, B. J., O'Brien, J. F. and Chu, C.-C., "System Identification and Control of the JPL Active Structure," AIAA Paper No. 91-1231, Proceedings of the 32nd SDM Conference, Baltimore, MD, April, 1991, pp. 2247-2255.

Fleming, F. M. and Crawley, E. F., "The zeros of Controlled Structures: Sensor/Actuator Attributes and Structural Modelling," AIAA Paper No. 91-0984, Proceedings of the 32nd SDM Conference, Baltimore, MD, April, 1991, pp. 1806-1816.

Franklin, G. F. and Powell, J. D., *Digital Control of Dynamic Systems*, Addison-Wesley Publishing Company, Reading, MA, 1980.

Freudenberg and Looze, "Right Half Plane Poles and Zeros and Design Tradeoffs in Feedback Systems," IEEE Transactions on Automatic Control, Vol. AC-30, No. 6, June, 1985, pp. 555-565.

Gehling, R. N., "Active Vibration Suppression via LQG/LTR; Analytic and Experimental Results for the PACOSS Dynamic Test Article," Paper No. CAA, Proceedings of the Damping 1991 Conference, San Diego, CA, February, 1991.

Gilbert, M. G., Schmidt, D. K., and Weisshaar, T. A., "Quadratic Synthesis of Integrated Active Controls for an Aeroelastic Forward-Swept-Wing Aircraft," *Journal of Guidance, Control, and Dynamics*, Vol. 7, No. 2, March-April, 1984, pp. 190-196.

Hassig, H. J., "An Approximate True Damping Solution of the Flutter Equation by Iteration," Journal of Aircraft, Vol. 8 No. 11, Nov., 1971, pp. 885-889.

Heeg, J., "An Analytical and Experimental Study to Investigate Flutter Suppression Via Piezoelectric Actuation," M. S. Thesis, George Washington University, School of Engineering and Applied Science, Washington, DC, 1991.

Horikawa, H. and Dowell, E. H., "An Elementary Explanation of the Flutter Mechanism with Active Feedback Controls," *Journal of Aircraft*, Vol. 16, No. 4, April, 1979, pp. 225-232.

Hyland, D. C. and Bernstein, D. S., "The Optimal Projection Equations for Fixed-Order Dynamic Compensation," *IEEE Transactions on Automatic Control*, Vol. AC-29, 1984, pp. 1034-1037.

Karpel, M. and Hoadley, S. T., "Physically Weighted Approximations of Unsteady Aerodynamic Forces Using the Minimum-State Method," NASA TP-3025, March, 1991.

Karpel, M., "Design for Active Flutter Suppression and Gust Alleviation Using State-Space Aeroelastic Modeling," *Journal of Aircraft*, Vol. 19, No. 3, March, 1982, pp.221-227.

Kuethe, A. M. and Chow, C.-Y., "Foundations of Aerodynamics: Bases of Aerodynamic Design," 3rd Ed., John Wiley and Sons, New York, 1976.

Kwakernaak, H. and Sivan, R., *Linear Optimal Control Systems*, Wiley-Interscience, John Wiley and Sons, Inc., New York, 1972.

Lazarus, K. B., Crawley, E. F. and Bohlmann, J. D., "Static Aeroelastic Control Using Strain Actuated Adaptive Structures," *Journal of Intelligent Material Systems and Structures*, Vol. 2, No. 3/July, 1991, pp. 386-410.

Lazarus, K. B., Crawley, E. F. and Lin, C.Y., "Fundamental Mechanisms of Aeroelastic Control with Control Surface and Strain Actuation," AIAA Paper No. 91-0985, Proceedings of the 33rd AIAA/ASME/ASCE/AHS Structures, Structural Dynamics and Materials Conference, Baltimore, MD, April, 1991, pp. 1817-1831.

Lazarus, K.B. and Crawley, E.F., "Induced Strain Actuation of Composite Plates," GTL Report No. 197, Massachusetts Institute of Technology, Cambridge, MA, 1989.

Lee, C-K. and Moon, F.C., "Laminated Piezopolymer Plates for Torsion and Bending Sensors and Actuators," *J. Acoustical Society of America*, Vol. 85, No. 6, June, 1989.

Lehtomaki, N. A., Castanon, D. A., Levy, B. C., Stein, G., Sandell, N. R. Jr. and Athens, M., "Robustness and Modeling Error Characterization," *IEEE Transactions on Automatic Control*, Vol. AC-29, No. 3, March, 1984, pp. 212-220.

Liebst, B. S., Garrard, W. L., and Adams, W.M., "Design of an Active Flutter Suppression System," *Journal of Guidance, Control, and Dynamics*, Vol. 9, No. 1, Jan.-Feb., 1986, pp. 64-71.

Maciejowski, J. M., *Multivariable Feedback Design*, Electronic Systems Engineering Series, Addison-Wesley Publishing Company, New York, 1989.

Mahesh, J. K., Stone, C. R., Garrard, W. L. and Dunn, H. J., "Control Law Synthesis for Flutter Suppression Using Linear Quadratic Gaussian Theory," *Journal of Guidance and Control*, Vol. 4, No. 4, July-Aug., 1981, pp. 415-422.

Meirovitch, L. and Kwak, M. K., "Convergence of the Classical Rayleigh-Ritz Method and the Finite Element Method," *AIAA Journal*, Vol. 28, No. 8, Aug. 1990, pp. 1509-1516.

Meirovitch, L., *Analytical Methods in Vibrations*, MacMillan Pub. Co., New York, 1967.

Mercadal, M., "Homotopy Approach to Optimal, Linear Quadratic, Fixed architecture Compensation," *Journal of Guidance, Control and Dynamics*," Vol. 14, No. 6, Nov.-Dec., 1991, pp. 1224-1233.

Miller, D. W., Jacques, R. N. and de Luis, J., "Typical Section Problems for Structural Control Applications," AIAA Paper No. 90-1225, Proceeding of

the AIAA Dynamic Specialists Conference, Long Beach, CA, April 5-6, 1990, pp. 334-348.

Moore, B. C., "Principal Component Analysis in Linear System: Controllability, Observability, and Model Reduction," *IEEE Transactions. on Automatic Control*, AC-26, 1981, pp. 17-31.

Mukhopadhyay, V, "Flutter Suppression Digital Control Law Design and Testing for the AFW Wind-Tunnel Model," AIAA Paper No. 92-2095, Proceeding of the AIAA Dynamics Specialist Conference, Dallas, TX, April, 1992.

Mukhopadhyay, V., Newsom, J. R., and Abel, I., "Reduced-Order Optimal Feedback Control Law Synthesis for Flutter Suppression," *Journal of Guidance and Control*, Vol. 5, No. 4, July-Aug., 1982, pp. 389-395.

Newsom, J. R., "Control Law Synthesis for Active Flutter Suppression Using Optimal Control Theory," *Journal of Guidance and Control*, Vol.2, No., 5, Sept.-Oct., 1979, pp. 388-394.

Newsom, J. R., Pototzky, A. S., and Abel, I., "Design of a Flutter Suppression System for an Experimental Drone Aircraft," *Journal of Aircraft*, Vol. 22, No. 5, May, 1985, pp. 380-386.

Noll, T. E., "Aeroservoelasticity," AIAA Paper No. 90-1073, Proceedings of the 31st Structures, SDM Conference, Long Beach, CA, April, 1990, pp. 1560-1570.

Noll, T., Perry, B. III, Tiffany, S., and others, "Aeroservoelastic Wind-Tunnel Investigations Using the Active Flexible Wing Model - Status and Recent Accomplishments," presented at the 30th Structures, Structural Dynamics and Materials Conference, Mobile, AL, April, 1989, pp. 68-75.

Ohta, H., Fujimori, A., Nikiforuk, P. N. and Gupta, M. M., "Active Flutter Suppression for Two-Dimensional Airfoils," *Journal of Guidance, Control, and Dynamics*, Vol. 12, No. 2, March-April, 1989, pp. 188-194.

Pan, W., Zhang, Q., Bhalla, A., and Cross, L. E., "Field-Forced Antiferroelectric-to-Ferroelectric Switching in Modified Lead Zirconate

Titanate Stannate Ceramics," *J. American Ceramic Society*, Vol. 72, No. 4, 1989, pp. 571-578.

Perry, B. III, Mukhopadhyay, V., Hoadley, S. T., and others, "Digital-Flutter-Suppression-System Investigations for the Active Flexible Wing Wind-Tunnel Model," AIAA Paper No. 90-1074, Proceeding of the 31st SDM Conference, Long Beach, CA, May, 1990, pp. 1571-1581.

Peterson, L. D., "Optimal Projection Control of an Experimental Truss Structure," *Journal of Guidance, Control and Dynamics*, Vol. 14, No. 2, March-April, 1991, pp. 241-250.

Phillips, D. J., Hyland, D. C. and Collins, E. G. Jr., "Experimental Demonstration of Active Vibration Control for Flexible Structures," Proceedings of the 29th Conference on Decision and Control, Honolulu, HA, December, 1990, pp. 2024-2029.

Rubenstein, S. P., Saunders, W. R., Ellis, G. K., Robertshaw, H. H. and Baumann, T., "Demonstration of a LQG Vibration controller for a Simply-Supported Plate," Resent Advances in Active Control of Sound and Vibration, Blacksburg, VA, April, 1991, pp. 618-630.

Theodorsen, T. and Garrick, I. E., "Nonstationary Flow About a Wing-Aileron-Tab Combination Including Aerodynamic Balance," NACA, Report No. 736, 1942.

Theodorsen, T., "General Theory of Aerodynamic Instability and the Mechanism of Flutter, NACA Report 496, 1935.

Tiffany, S. H. and Adams, W. M. Jr., "Nonlinear Programming Extensions to Rational Function Approximation Methods for Unsteady Aerodynamic Forces," NASA TP-2776, July, 1988.

Tiffany, S. H. and Karpel, M., "Aeroservoelastic Modeling and Applications Using Minimum-State Approximations of the Unsteady Aerodynamics," presented at the 30th Structures, Structural Dynamics and Materials Conference, April, 1989, pp. 265-274.

Voth, C. T. and Stoughton, R. M., "$\mathcal{H}_\infty$ Control for the PACOSS DTA," Paper No. CAB, Proceedings of the Damping 1991 Conference, San Diego, CA, February, 1991.

Wada, B.K., Fanson, J.L., and Crawley, E.F., "Adaptive Structures," Proceedings of the ASME Winter Annual Meeting, San Francisco, CA, December, 1989.

Wang, B.-T. and Rogers, C. A., "Laminated Plate Theory for Spatially Distributed Induced Strain Actuators," *Journal of Composite Materials*, Vol. 25, No. 4/April, 1991, pp. 433-452.

Waszak, M. R. and Srinathkumar, S., "Active Flutter Suppression: Control System Design and Experimental Validation," AIAA Paper No. 91-2629, Proceeding of the 31st SDM Conference, Long Beach, CA, May, 1990, pp. 276-286.

Watkins, C. E., Woolston, D. S. and Cunningham, J. J., "A Systematic Kernel Funciton Proceedurefor Determining Aerodynamic Forces on Oscillating or Steady Finite Wings at Subsonic Speeds," NASA TR-48, 1959.

Weisshaar, T. A. and Ehlers, S. M., "Adaptive Static and Dynamic Aeroelastic Design," Presented at the 1991 International Forum on Aeroelasticity and Structural Dynamics: Workshop on Smart Material Systems and Structures, June, 1991.

Weisshaar, T.A. and Foist, B.L., "Vibration Tailoring of Advanced Composite Lifting Surfaces," *Journal of Aircraft*, Vol. 22, No. 2, February, 1985, pp. 141-147.

Zeiler, T. A. and Weisshaar, T. A., "Integrated Aeroservoelastic Tailoring of Lifting surfaces," *Journal of Aircraft*, Vol. 25, No. 1, Jan., 1988, pp. 76-83.

Zhou, N. and Cudney, H. H., "Active Control of Sound Transmission by Plates in the Reverberant Field," Proceeding of the Conference on Resent Advances in Active Control of Sound and Vibration, Blacksburg, VA, April, 1991, pp. S10-S21.